12-2018

Taming and Leveraging Directionality and Blockage in Millimeter Wave Communications

Jingchao Bao
University of Tennessee, jbao2@vols.utk.edu

To the Graduate Council:

I am submitting herewith a dissertation written by Jingchao Bao entitled "Taming and Leveraging Directionality and Blockage in Millimeter Wave Communications." I have examined the final electronic copy of this dissertation for form and content and recommend that it be accepted in partial fulfillment of the requirements for the degree of Doctor of Philosophy, with a major in Electrical Engineering.

Husheng Li, Major Professor

We have read this dissertation and recommend its acceptance:

Seddik Djouadi, Aly E. Fathy, Xiaopeng Zhao

Accepted for the Council:

Dixie L. Thompson

Vice Provost and Dean of the Graduate School

(Original signatures are on file with official student records.)

Taming and Leveraging Directionality and Blockage in Millimeter Wave Communications

A Dissertation Presented for the

Doctor of Philosophy

Degree

The University of Tennessee, Knoxville

Jingchao Bao

December 2018

Acknowledgments

First and for most, I would like to express my deepest appreciation to my academic advisor — Dr. Husheng Li for the continuous support and patience. My research would have been impossible without the aid, support and your immense knowledge. The enthusiasm he has for his research was contagious and motivational for me during my Ph.D. pursuit.

Besides my advisor, I would like to thank the rest of my thesis committee, Prof. Aly E. Fathy, Prof. Seddik Djouadi and Prof. Xiaopeng Zhao. They have provided me extensive professional guidance and a great deal of comments and encouragement which incented me for my thesis.

I am grateful to all of my colleagues who I have had the pleasure to work with in University of Tennessee. Yawen Fan, Liang Li, Yifan Wang, Zhiyang Zhang and Rukun Mao, for the meaningful discussions in our group meeting and for all the fun we have had. I am in debt with Dr. Xiandeng He and Dr Yunhun Yi for the invaluable input to the testbed development. Part of my work would be impossible without the optical system provided from the group of Dr. Jinong Tan and Xiaodong Yang in MABE department. My sincere thanks also go to Jiazhen Zhou, Chiyu Zhang and Prof. Dengfeng Sun for all the fun I had during my stay in Purdue University with UAV experiment.

I would like to thank my friends for accepting nothing less than excellence from me. I am grateful for time spent with friends, for all the memorable trips into the Great Smoky mountains with my backpacking buddies and authentic BBQ.

Last but not the least, I would like to thank my parents, Li Li and Xinyu Bao, for supporting me spiritually throughout my life in general. Thanks for let me pursue whatever I would like to do in my life. You are my ultimate role models.

Abstract

To cope with the challenge for high-rate data transmission, Millimeter Wave(mmWave) is one potential solution. The short wavelength unlatched the era of directional mobile communication. The semi-optical communication requires revolutionary thinking. To assist the research and evaluate various algorithms, we build a motion-sensitive mmWave testbed with two degrees of freedom for environmental sensing and general wireless communication.

The first part of this thesis contains two approaches to maintain the connection in mmWave mobile communication. The first one seeks to solve the beam tracking problem using motion sensor within the mobile device. A tracking algorithm is given and integrated into the tracking protocol. Detailed experiments and numerical simulations compared several compensation schemes with optical benchmark and demonstrated the efficiency of overhead reduction. The second strategy attempts to mitigate intermittent connections during roaming is multi-connectivity. Taking advantage of properties of rateless erasure code, a fountain code type multi-connectivity mechanism is proposed to increase the link reliability with simplified backhaul mechanism. The simulation demonstrates the efficiency and robustness of our system design with a multi-link channel record.

The second topic in this thesis explores various techniques in blockage mitigation. A fast hear-beat like channel with heavy blockage loss is identified in the mmWave Unmanned Aerial Vehicle (UAV) communication experiment due to the propeller blockage. These blockage patterns are detected through Holm's procedure as a problem of multi-time series edge detection. To reduce the blockage effect, an adaptive modulation and coding scheme is designed. The simulation results show that it could greatly improve the throughput given appropriately predicted patterns.

The last but not the least, the blockage of directional communication also appears as a blessing because the geometrical information and blockage event of ancillary signal paths can be utilized to predict the blockage timing for the current transmission path. A geometrical model and prediction algorithm are derived to resolve the blockage time and initiate active handovers. An experiment provides solid proof of multi-paths properties and the numeral simulation demonstrates the efficiency of the proposed algorithm.

Table of Contents

List of Tables

List of Figures

Chapter 1

Introduction

1.1 Millimeter Wave Communication

As the huge demand for mobile data increases with a 40%-70% growth rate[19], lack of adequate spectrum is a common challenge confronting the mobile network. The traffic of mobile device in the next decade could boom to 1000 times compared with current traffic[69], which render it impossible to accommodate with sub 6GHz microwave spectrum[18]. This acute conflict between the demand and supply of cellular spectrum inevitably urges the exploration of higher-frequency bands for more room for growth.

To meet the challenge of these requirements, one of the key enabling technologies is millimeter wave(mmWave) communication[38, 70, 73, 76]. It is widely been accepted that mmWave is most promising to achieve multi-Gbps throughput for mobile network as the available bandwidth in mmWave is considerably large compared with microwave counterpart [75, 100]. Based on Shannon equation, the channel capacity of additive white Gaussian noise channel is

$$C = B\log_2(1 + \frac{P}{N_0 B}), \tag{1.1}$$

where B, P and N_0 is the bandwidth, signal strength and noise power spectral density. If signal-to-noise ratio (SNR) $\frac{P}{N_0 B}$ is fixed, the channel capacity increases linear with the available bandwidth B. Unfortunately, with the strict regulation on the transmitting power, such freedom does not exist[15]. Nevertheless, the mmWave spectrum could provide a satisfactory link for small cell mobile network, especially within a ultra-dense system[12, 29, 106]. One more feature of mmWave mobile communication is that the enormous bandwidth could be flexible deployed for self back-haul with fast and dynamic deployment of base station [65, 74], where the wide spectrum can be simultaneously scheduled for both mobile wireless access and back-haul.

The research of mmWave dates back to one century ago. Recently, the interest on mmWave is focused on the mobile network, which is in sharp contrast with stationary scenario. In the next section, the history of millimeter wave communication is briefly reviewed and recent progress in this area.

1.2 A Brief History of mmWave

It is surprising that the history of mmWave research begins from a hundred years ago in company with the infant era of wireless communication.

In 1865, Maxwell successfully predicted the behavior of electromagnetic propagation and later many components which is currently well-known in microwaves are soon to be developed, which paves the road to mmWave research. Shortly after that, Sir. Bose build its own mmWave components such as spark transmitter, coherer, dielectric lens, polarizer, horn antenna and cylindrical diffraction grating at India in 1895 [26].

In Bose's experiment, he successfully demonstrated that the electromagnetic waves with wavelength from 5mm to 2.5cm could ring a bell remotely and explode the gunpowder located 23m away through two intervening walls, which is earlier than Marconi's demonstration of wireless communication. Then the research on mmWave went to hibernation until its re-emergence at the age of space and satellite communication. Since 1950s, the crowded spectrum on lower frequency and advancement in solid state materials brings back mmWave to the researcher. The first breakthrough is on the mmWave Radar astronomy for the moon surface [52].

From 1990 to 2000s, the research interest migrated to the wireless personal area network(WPAN) and wireless local area network(WLAN). The research starts with channel measurement[101], and then followed by attempt of standardization for high data throughput network ,e.g. ECMA-387, IEEE 802.15.3c, wirelessHD and IEEE 802.11ad[16, 25, 39, 40]. All of these standards emphasize the high throughput yet dynamic and mobile scenarios are mostly ignored.

Today, most efforts are devoted to the research of mobile mmWave network. FCC has issued a temporary license for field experiments[104], and all service providers such as Verizon, AT&T, T-Mobile and Docomo are actively developing their prototype systems. In addition to that, Google, Facebook, Nokia and NI also put substantial efforts into promotion of development of mobile mmWave applications.

In the next section, the challenge for mobile network is elaborated and potential solutions are given and addressed in the future chapters.

1.3 Challenge of mmWave Mobile Network

For wireless radio, link budget is a key parameter to understand power requirement for system design. Link budget accounts for all the gain or loss between the transmitter to the receiver. In the mmWave regime, the notorious disadvantage is the relatively large propagation loss which tightens the link budget. Both theoretical result and filed channel measurements confirm that more link budget compensation is needed when compared with sub 6GHz spectrum.

1.3.1 Propagation Loss of mmWave Communication

From theoretical side, the free space propagation of electromagnetic wave can be mathematically characterized by Friis transmission Equ. 1.2. The received power is calculated with distance between two antennas d, transmitted power P_t and transmitting and receiving antenna gain G_t and G_r respectively. As the wavelength of electromagnetic wave is inverse to the frequency with respect to the speed of light$\lambda = \frac{c}{f}$, the received power is proportional to square of wavelength λ and thus the free space loss is considerably large compared with traditional low frequency spectrum. For the same separation distance of 100m, the path loss of 60GHz is more than 28dB compared with 2.4GHz and 42.3dB for 460MHz. The heavy path loss appears as non-trivial problem when adopting mmWave as new wireless pipe.

$$P_r(d) = P_t G_t G_r (\frac{\lambda}{4\pi})^2 d^{-n} \tag{1.2}$$

When the path loss exponent $n = 2$ in the above Equ.1.2, the above model characterize the propagation loss in the perfect vacuum. In the modeling of non-free-space propagation, the value of n could range from 2-6 as a rough approximation for the link budge estimation. The coefficient issues of mmWave have been studied by multiple institutes and it is no different than the microwave counterpart, although it is more scenario specific.

1.3.2 Atmospheric Effect on mmWave Communication

As for the field channel measurements, the result reveals another negative factor in the link budget. Unlike the outer space, the atmosphere consists different gaseous molecules. Under the clear normal weather condition, most of the molecules will be oxygen or nitrogen while water molecules can dramatically increase in the adverse weather.

All electromagnetic wave can be absorbed by these molecules with a certain degree in the atmosphere, yet some frequencies suffer more. As for the traditional microwave communication except water, the impact of atmosphere can be ignored in most scenarios, which does not stand correctly with the mmWave spectrum. With channel measurements, it appears that some bands have more path loss compared with others. From the measurement in Figure.1.1, several peaks absorption besides the distance-dependent path loss can be observed around 60GHz, 180GHz and 320GHz due to different molecular absorption. The 60GHz electromagnetic signal is attenuated by the oxygen molecular while other two peaks are created by the water vapor in the atmosphere.

For dry or normal weather, water vapor is a minor player yet a major constituent during rain, snow, hail or fog. Therefore, the total attenuation is a weather-dependent result and deserves special attention because its presence dramatically affects the propagation of electromagnetic radiation. Great number of researches are denoted to characterize these effects, and these have been successfully applied for earth-space communication.

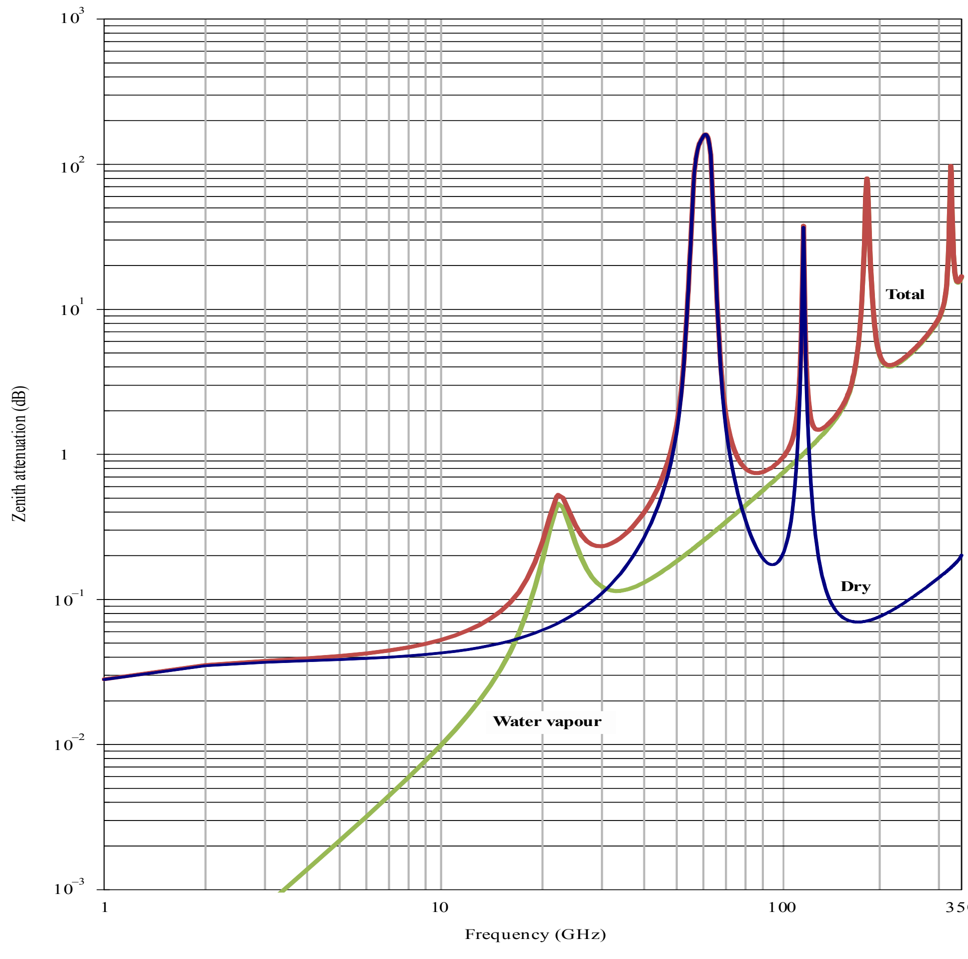

Figure 1.1: Total, dry air and water-vapour zenith attenuation from sea level from [86] (Pressure = 1 013.25 hPa; Temperature = 15°C; Water Vapour Density = 7.5 g/m^3)

This attenuation is a hinder as the satellite link can be several tens of kilometers, yet this can be a careless conclusion when it comes to the small cell outdoor mobile network as the distance will be far less than satellite channel. As showed in previous study[68], the rain attenuation at 28GHz is about 1.4dB over 200m, which is not a severe negative factor for small cell. The research on other spectrum [101, 102] has similar result but not on extreme weather. In general, the impact of rain exits on the outdoor mobile system but it is a manageable factor in the short range small cell.

1.3.3 Fight with Pathloss — Multiple-Input and Multiple-Output (MIMO) and Beamforming

To fight all these challenges, we need a close look at equation.1.2 for potential solutions. Two types of compensations are available. The transmitting power P_t is one choice, yet it has limited freedom due to regulations. In additional to that, large P_t could also drain out the limited battery for the mobile device. From the radio station sides, increasing the transmitting power would increase both inter-cell interference and intra-cell interference as the signal to interference and noise radio (SINR) is the key for system design.

Fortunately, a high gain antenna is a feasible solution with the techniques of massive MIMO and beamforming. The answer originates from the very small wavelength of mmWave, which makes it practical to pack numerous miniaturized antennas into small form factors, and thus massive MIMO and beamforming can be used to provide highly directive pseudo optical-type communication[8, 35, 38, 76, 109].

The classical antenna theory [17] show that the maximum gain G of identical antenna array is proportional to

$$G \propto \frac{(NL)^d}{\lambda^2} \tag{1.3}$$

where d is the dimension of antenna array (linear or square array) and λ is defined as before. N is the number of antenna along one dimension and L is the effective length of antenna elements. By adopting these large antenna arrays at both sides, the excess path loss can be completely compensated by the enormous antenna gains with up-to-date semi-conductor technique. As showed in the field experiment in [76], for same aperture size, path loss on 30GHz between TX and RX is reduced with both antenna array installed on both sides compared with single patch antenna of 3GHz.

Despite these benefits of large antenna arrays, the complexity of both hardware and software design increases with the number of elements. Although a full digital beamforming design provides the most flexible tunning capability, the cost and power consumption is prohibitive huge for mobile commercial devices and simplifications on architecture have to be made to reduce the workload for real-time digital process[44]. The basic principle is that low power and simplified analog components will replace part of the RF chain components in hardware. One feasible solution [89] is to adopt analog phase shifters or delay vector network to offer limited steering ability in the near term of mmWave. Other designs also intend to replace power-hungry high resolution ADCs with low resolution ones to reduce the whole cost[38, 64]. With new mixed beamforming structure, the signal processing algorithms must accommodate the hardware constraints for the optimal performance. Hybrid beamforming architectures [2, 10], beamspace-based signal processing techniques [84], lens-based analog beamforming antennas[10], and low-rate ADC methods [58] have been proposed in recent literature. In conclusion, the directional antenna is a prerequisite for path loss compensation in the mmWave era, yet no optimal result on the antenna array structure can be given by now.

1.3.4 Blockage — The Barrier in Mobile mmWave Communication

With the link budget satisfied, how to fully capitalize this huge capacity of mmWave is still an unsolved issue for mmWave networking. With directional communication, the quality of wireless link, which could translate into a user-perceivable throughput and good quality of service (QoS), relies heavily on the condition of light of sight (LOS) channel.

Although following the same physical law, the order of magnitude of frequency of mmWave render it more difficult to penetrate common objects due to weak diffraction[108], more absorption[6] and strong reflection[71]. In particular, some common materials of brick could cause 40-80 dB[4, 108] attenuation and human body can result a loss of 20-35dB[50]. Foliage and vegetation also count for the loss[85] with heavy water contents.

The challenge in this case stems from the fact that the LOS path between a user and a base station may easily be blocked by obstacles, such as treetops, pedestrians, and buildings when the user moves. Therefore, the large variation of signal strength poses severely threat to the quality of wireless link, where the resultant intermittent connection at the physical layer has a huge negative impact on the performance of higher layers. Depending on the density of obstacles and the user's mobility pattern, channel modeling shows that outage on a mmWave link may occur with a significant 20% - 60% probability [73, 81] and it may lead to over 10-fold degradation of the TCP throughput [67, 107, 110]. Therefore, unless being addressed properly, the blockage appears as the bottleneck from fully utilizing the capacity of the mmWave channel.

1.3.5 Mobility Management — Mobility-Induced Beam Management and Robust Connection

Another serious issue for mmWave mobile communication is that directional communication significantly increases the probability of deafness during mobile roaming. The directional antenna can only provide a limited angular coverage which implicates a more complicated control layer to provide full-cell coverage. In the mobile communication systems, The initial association (IA) problem, which refers to the procedures before the user transits from other states to connected mode, requires both base station and mobile device to agree on the appropriate beam directions with a large search space. This introduces significant delay and system overhead to achieve sufficient link budget. Besides that, other problems like the discovery range mismatch, multi-connectivity and dynamics-aware access urges for a suitable new approach in mmWave network[9].

For IA process, all algorithms can be categorized into exhaustive search[42], iterative method[23] and randomized pairing[45, 63]. Brutal force explicit exams all possible pairing while iterative methods will adopt a multi-stage procedure which gradually search space with finer granularity. The random directional beamforming procedure attacks this problem to minimize the missing rate with multi-user case if randomly located in the cell[45]. In addition to that, the auxiliary information from GPS, off-band specturm like LTE or WiFi can offer geographic information to locate the relative distance and direction to reduce the training process as mentioned above[37, 61].

The second hurdle induced by mobility is the routinely beam tracking. The optimal beam direction founded by initial association rarely need adjustment with static scenarios, whereas the mobility could quickly increase the angle misalignment and thus require periodic beam refinement to correct the beam direction. There are a few necessary reasons for that. In mmWave bands, the user mobility leads very limited channel coherence time and the periodic re-aligned beam direction could maintain the coherence. The second problem is that a minimal beam tracking could reduce the system overhead for a consistent link budget. On the contrary, a beam training from the scratch in initial access procedure can provide similar result yet overhead would be prohibitive.

In [20], some candidates beam pairs is selected and tracked in the previous phase for further examination over time. Another alternative approach in [22] intend to track the channel condition based on the geometry information from the environment. Authors in [28] estimates the angle of arrival (AoA) by using variations in the radiation pattern of the beam as a function of this angle. The beam tracking in general is to extend the validity period of best beam-direction pair but not to totally avoid or replace the re-initial access procedure, especially under the circumstance of long-time blockage.

1.4 Organization of Study

Next chapter.2 will focus on the current progress of mmWave tested. The detailed scheme and infrastructure of the 60GHz testbed with 2 degree of freedom(DoF) is given and a few experiment results followed. In Chapter 3, the beam tracking problem is explained in details. A sensor-based beam tracking algorithm is proposed to minimize the beam misalignment and compared with optical benchmark. Another option to remain connection is multi-connecitivity in Chapter 4. Moreover, the feedback scheme is discussed to provide better packet transmission rate and throughput. Then in chapter.5, we study the blockage in the mmWave communication on a more dynamic scenario, naming the unmanned aerial vehicle. The blockage pattern and loss are measured, and we further propose an algorithm to mitigate the problem. In chapter.6, the blockage information is utilized to predict the blockage timing for the LOS path. A geometric solution proved to be feasible. The future of this proposal is given in chapter.7.

Chapter 2

60GHz mmWave Testbed

2.1 Introduction

Before the mass deployment of mmWave products, it is necessary to have thorough testing for channel modeling and prototyping. A severe barrier in the mmWave research is the lack of accessible experimental platform. Traditional radio design methodology operating in the lower spectrum is no longer valid in the mmWave spectrum. For that reason, various organizations from both academic and industry put tremendous efforts to develop new hardware platforms. However, the cost of a mmWave system made by discrete components could be prohibitive expensive and the bulky system is too cumbersome to fit as a mobile system. An integrated signal processing and hardware design is badly needed to avoid high cost and energy consumption.

In this chapter, we first go through the literature for all the testbeds developed by now and then propose our mmWave testbed. This testbed has two degrees of freedom for movement detection and integrated with motion sensor for movement compensation. It could be applied for both PHY/MAC prototyping and environmental sensing.

2.2 Literature Review

Here we gathered the available information of all kind of platforms. In general, all these platforms can fit into these fields of interest.

1. Channel Modeling

2. Throughput Performance

3. Software Defined Radio

4. Wireless Sensing

In the initial phase of mmWave communication, most of the platforms are focused on the channel observation, measurement and modeling. Therefore, these hardware platforms consist of dedicated hardware with fixed horn antenna.[5, 53, 90, 101] In [53], the channel measurement is done by a 400 Mcps broadband sliding correlator channel sounder with horn antennas of different half-power beamwidth (10.9° and 7°). The sounder is mounted on a LabVIEW-controlled Gimbal to control the direction. It is suitable to measure and model channel propagation characteristics.

Besides channel measurements, some platform is also capable for radio-wave imaging. In [82], the authors compared different available imaging sensors in mmWave spectrum and also describes a 94GHz customized sensor for mmWave imaging. The paper [87] provides an indoor radio experiment about 60GHz wireless sensor network for virtual imaging.

As the birth of 802.11ad compatible products, researchers intend to explore the possibility to build testbeds using commercial WiGig devices. These products do not allow modification of the PHY/MAC layer design and frame structure. In addition to that, beamforming algorithms are all in-built, which means they have limited maneuverability on the PHY/MAC layers. Nevertheless, with an affordable price tag, it could offer a glimpse for the interaction between upper layers and directional PHY layer. In [60], a 60GHz WiGig dock is used to understand the beamforming, interference and frame level protocol performance with compromised directional antenna array. Authors in [79] attempt to build multi-Gigabit indoor enterprise WLAN network with multiple docks and laptops. With small wavelength of mmWave spectrum, the imaging precision is greatly improved. In paper [111], authors uses Wilocity 60GHz networking chipsets for high precision RF imaging. Based on the experiment result, it is safe to conclude that the limited maneuverability of commercial chipsets presets more challenges for the researcher to modify the hardware. Moreover, it is extremely difficult to locate the real cause given the observed results. Nevertheless, these are only low-cost solutions for preliminary experimental results by now.

A reconfigurable platform is of vital importance for validating prototype design before the deployment of protocols and applications. In the micowave spectrum, software defined radio(SDR)[98] has reformed the radio communication research that can be implemented only by dedicated hardware in the old days. To validate the design of mmWave network and sensing, a SDR in mmWave spectrum that can customize the waveform and capture raw signal would boost the research. In [1], authors propose the Agile-Link system for beam searching without scanning the whole space explicitly. In their paper, a customized 24 GHz ISM band mmWave platform is assembled with a phased array that has 8 antennas. However, the phase shifter used is discontinued and none replacement can be found on the market. Aside from that, most academic researchers tend combine off-the-shelf SDR platform with new mmWave radio head. As in [30, 36, 37], a testbed consists of VubIQ V band evaluation kit and WARP V1 are assembled to study beam searching algorithm in 802.11ad. With same platform, they propose several beam management approaches to reduce the overhead in both IA and beam tracking phase. Similarly, the first generation of WiMi from University of Wisconsin, Madison also accepts the similar architecture with a baseband unit combined with WARP V3 and external ADC/DAC module to study the link-level behavior and passive tracking system[91, 97]. All of these researches are done with horn antenna as no available electronically steerable phased-array antenna is available at that time.

These works above implement narrow-baseband transmission on mmWave, offer great design insight to capture and characterize the mmWave propagation. However, to truly release the power of mmWave spectrum, it is important to develop a testbed with an ultra-wide baseband to study the unique challenges in wideband signal processing. Recently, National instrument provides the first Gbps-level SDR modular hardware solutions with different mmWave spectrum radio heads[41]. The multi-FPGA baseband architecture supports the real-time digital signal processing capability.

Built upon that, in order to study the impact of imperfect of commercial-level practical phased array, a testbed with on-chip 12 elements phased array provided by Sibeam [78] is made to re-exam the impact of the artifact of real hardware on mmWave link characteristics, interference and spatial-reuse. Besides this, the OpenMili appears as the only available open source SDR testbed of 60GHz with an independent 4—element analog phased array. It is convenient with modularized antenna design, yet the cost for cables and connectors on mmWave spectrum is ridiculously expensive and the PCB layout is elusive to design. The baseband utilizes off-the-shelf FPGA and the firmware is developed with system on chip architecture. Another interesting testbed described in [83] contains an antenna array with lens and a group of 28GHz horn antennas to support simultaneous multi-beams. For such case, a mechanical rotation stage is still in need to provide full azimuth coverage.

There are two disadvantages on the above testbeds —cost and lack of mobility. Among all the platforms above, OpenMili is cheapest which costs 15K. However, the technique support is poor and learning curve is steep. On the other hand, NI mmWave and X60 will cost more than 170K for one unidirectional communication link. The second point is that all these systems, except the phased array antenna, have limited real-time antenna steering capability, thus beam searching and tracking cannot be implemented when the platform is moving. Therefore, they cannot cope with research of mmWave when real time motion is involved.

Attempting to mitigate these problems, we designed our own 60GHz mmWave testbed with two degree of freedom. One salient advantage of this platform is that it is motion sensitive. With motion sensor integrated, the testbed could monitor and compensate the beam tracking misalignment caused by mobility. Details are given below.

2.3 Motion Aware Testbed Scheme

Our testbed intents to build a half-duplex unidirectional communication link with one transmitter and one receiver on WiGig spectrum. The testbed contains three key-components — baseband processing unit, action module and RF converter. The receiver is mounted on a motorized platform, aka the action module while the transmitter is mounted on a fixed platform. The difference is owing to the fact that most of the experiment scenarios we considered are the downlink between base station and mobile terminal. A fixed base station does not require any movement in this scenario. Nevertheless, it can be easily extended to a double motorized platform with same setup. The basic scheme is showed in Fig.2.1. It contains two motorized components and several embedded systems for motion sensing and control. The signal processing of communication is accomplished by GNURadio in the laptop. As for the action module, the routine mechanical operation is controlled by the laptop and monitored by the embedded system while the real time motion sensing is directly realized on the low-level embedded system. The real time sensing does not require the coordination from high level command. Such direct scheme could reduce the latency involved by the coordination and details is given in the action module. The detailed component selections is listed in table.2.1 and explained below.

2.3.1 RF Module

The EK1HMC6350 evaluation kit is chosen. This kit includes two identical motherboards and two daughter boards for a half-duplex, 60 GHz millimeter wave link. This kit equips standard differential input/output baseband connectors and a MMPX connector to interface with a V-band antenna. Due to availability issue, we still utilize a pyramid antenna from Quinstar. The antenna is designed to have a half power beam width of 15° and antenna gain is 20dB. However, given the standard interface, an analog phased antenna array is still an available option in the future.

HMC 6300 and 6301 boards are compatible with 802.11ad standard and operate between 57GHZ to 64Ghz unlicensed spectrum with a bandwidth at most 1.8GHz. It is proved that there is no essential difference between low and high mmWave frequency [31] and thus the study result based on WiGig spectrum could characterize the properties of most mmWave spectrum. The combined gain adjustment of RX and TX is over $100dB$. Given the large blockage loss, a flexible real-time gain control interface should be developed.

The original evaluation kit includes a Windows graphical user interface (GUI) software allowing users to manage registers contents. However, the operation speed is too slow (100ms) and renders it useless in the real time adjustment. As the consequence of real-time control, the default solution is ignored and I developed a SPI interface with Arduino UNO for easy and fast access to the register with maximum refreshing rate of 1MHz. This speed can be further increased with more powerful embedded system with high clock speed.

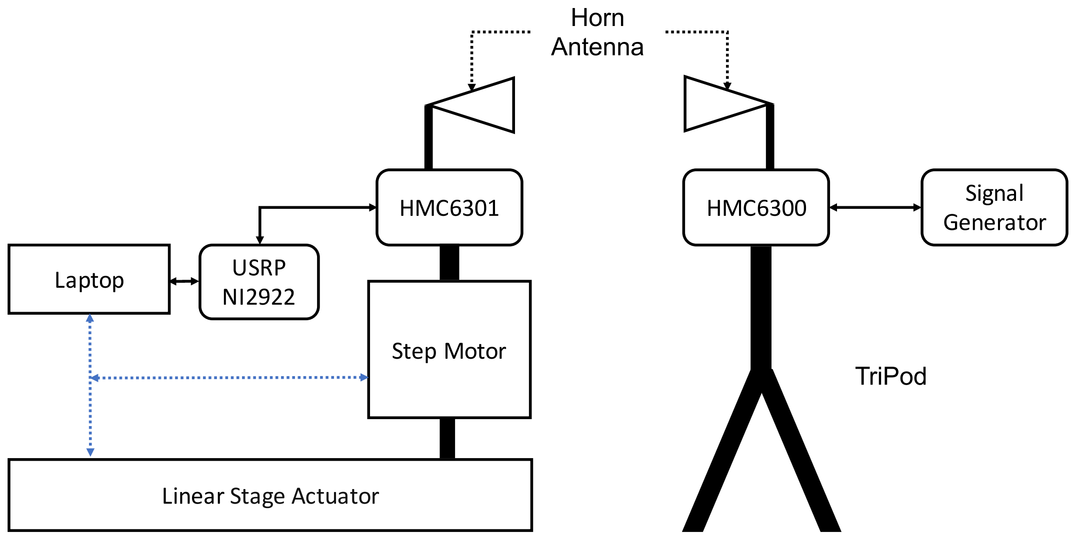

Figure 2.1: The Scheme of Two Degree of Freedom Motorized mmWave Communication Testbed.

Table 2.1: Testbed Component(* means optional components)

Testbed Components			
Hardware	RF Module	Transmitter	ADI HMC6300
		Receiver	ADI HMC6301
		External Clock *	
	Baseband Module	SDR	NI USRP 2922
		Daughter board	Basic TX/RX
		Input Resource*	Tektronix AFG3102C
	Action Module	Rotation Module	Mechaduino
		Linear Acturator	Mysweety 400mm Acturator
		Motion Module	SparkFun 9DoF Razor IMU
		Central Controller	Arduino UNO
		Acturator Driver	SMAKN Stepper Moter Drive
	Central Controller	Laptop	Dell
Software	Signal Processing		GNU Radio
	Embeded System		Arduino

Due to the high carrier frequency of mmWave, the carrier frequency offset and phase offset problems between transceivers are magnified with non-identical clock source. For environmental sensing problem with signal strength acquired only, a local crystal oscillator could satisfy the requirement. However, for experiments requires high order data transmissions (64, 128 QAM), the accurate phase coherence necessitates one single external clock resource, which is supported by this kit. This provides the flexibility for the experiments can be done by this testbed.

2.3.2 Action Module

A unique advantage of this testbed relies on the motion sensitive module. To compensate for the movement and rotation, it incorporates an inertia measurement unit (IMU) sensor to monitor the changing orientation. One unique challenge for the real-time compensation operation is that the system design need to response all movement with high speed and accuracy. A direct interaction between the mechanical components and sensor could offer the less latency and faster response. Therefore, the Razor 9 DoF with Invense MPU9250 is in charge of received the routine position command from laptop and further compensate the movement by incrementally adding either the direct measured or calculated displacement compensations.

Mechanical Components

The motorized platform consists of one linear movement stage and one 360° rotation stage. 400mm linear stage is driven by a 200 step/rev stepper motor with 5mm per round. The theoretical resolution for the movement is 0.025mm, which overly satisfies the demand of high precision.

On the linear stage, a closed-loop controlled rotation stage is built upon the open source Mechaduino. It utilizes a diametrical magnet mounted to the back of the motor shaft for position measurement and assure precision control. A 14 bit encoder AS5047D could achieve very high resolution with ±5% of step size, which translates to 0.09°. The experiment shows that one step movement (1.8°) takes 1ms to settle down.

By opening and maintaining a serial port between laptop and Arduino UNO, both linear and rotation stages are closely monitored by the central controller (Laptop). The information can be recorded for the future off-line analysis.

Motion Sensor

A IMU provides a low-cost solution of gyroscope/accelerometer/magnetometer within one chip for motion measurement. Moreover, the combination of these three components open the door of sensor fusion — tracking absolute orientation with respect to a fixed Earth frame. However, the accuracy is notoriously sensitive to the volatile environment and it is of vital importance to consider various factors below when the sensor is integrated.

- Initial Calibration: The MEMS sensors typically need calibration before use to ensure a stable performance. The raw measurements from three sensors are usually biased and asymmetric between 3-axis due to both internal and external causes. The initial calibration can take up to several tens of seconds for the sensors to initialize and for basic bias calibration to complete.

- Distorted Environment: Among all the sensors, the magnetometer delivers the reference for absolute orientation. However, the magnetic field around working place could be easily polluted by the motor, magnet components and even operational current. Unqualified PCB layout also introduces massive noise in measurements that void the algorithm.

- Refreshing Rate: The refreshing rate of sensor fusion filter rate is one of the important performance factors. For dynamic scenarios, a high refreshing rate could quickly stabilize the calculated quaternion and thus make a quick compensation. This factor is determined by both clock rate of micro controller and sensor sampling rate.

Considering all the factor above, we choose to using one independent micro controller and integrated IMU to offer clean measurements and higher refreshing rate, although the sensor can be integrated into the Mechaduino platform. If the IMU is too close to the motor or motor driver, the additional magnetic field could totally ruin the sensor fusion filter result.

2.3.3 Baseband Unit

To rapidly prototype various sampling and wireless communications systems, a National Instrument USRP NI2922 combined with basicTX/RX daughter board performs real-time data acquisition and process. This baseband unit equips with a dual, 14-bit, 100 MS/S ADC and dual 16-bit, 400 MS/s DAC to stream 50 MS/s of complex baseband samples to/from the host. Combined with GNURadio on the laptop, the software framework is unified with Python to prototyping mmWave directional communication system.

2.4 Performance and Channel Measurement

Here we will provide a preliminary analysis of channel measurement results of small scale movement. The landscape of the lab is shown in Fig. 2.2a and 2.3a, where the distance unit is feet. A transmitter and a receiver are placed at certain spots in the lab. Obviously, the wall and desk could behave as reflector. The location and direction of the transmitter (playing the role of the base station) are both fixed in the two tests. The receiver (playing the role of the mobile user), as shown in Fig.2.2a, moves along the linear stage actuator with the step of 1cm. At each step, the receiver rotates and measures the signal strength for every $1.8°$ degrees. The heat maps obtained from the experiments are given here. The two axes are the Azimuth angle of rotation and the distance of linear translation, respectively. In the LOS setting, the transmitter owns a LOS path toward the receiver and the result is shown in Fig. 2.2b. On the other hand, the antenna points to the wall in the NLOS scenario and only reflection paths are available as shown in Fig. 2.3b. Based on these two measurements, we could conclude following results.

- Within limited enclosed space, the signal almost fills the room. This result may first contradict with intuition of directional communication and high path loss. However, both experiments show that most azimuth angles have SNR above 0dB. This is due to the fact that the receiver has a high dynamic gain range to amplify the received signal, of which may not hold solid for mobile devices. In that case, only a few directions are qualified to maintain a communication link.

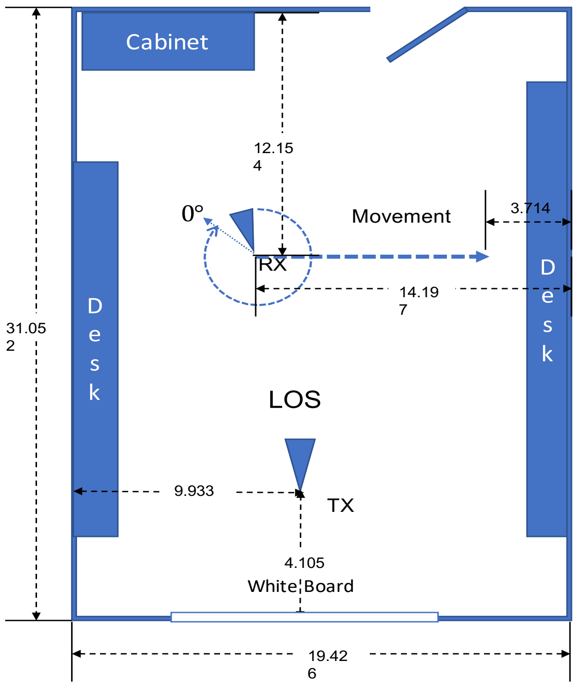

(a) Scheme

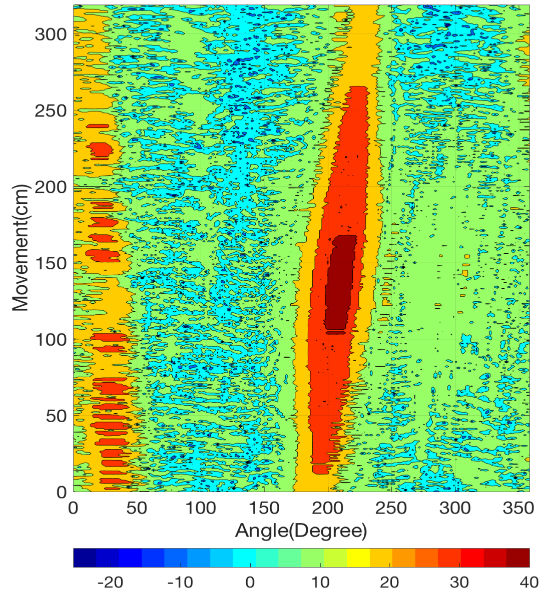

(b) Heatmap

Figure 2.2: Heatmap of LOS measurement in the Indoor Environment

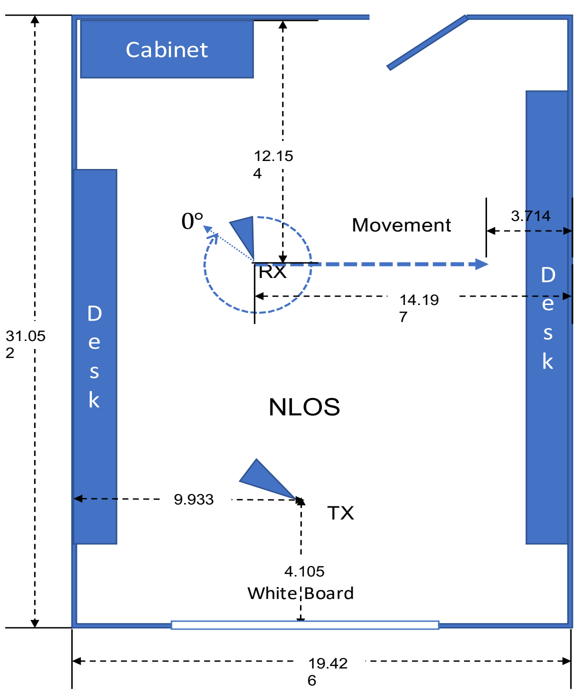

(a) Scheme

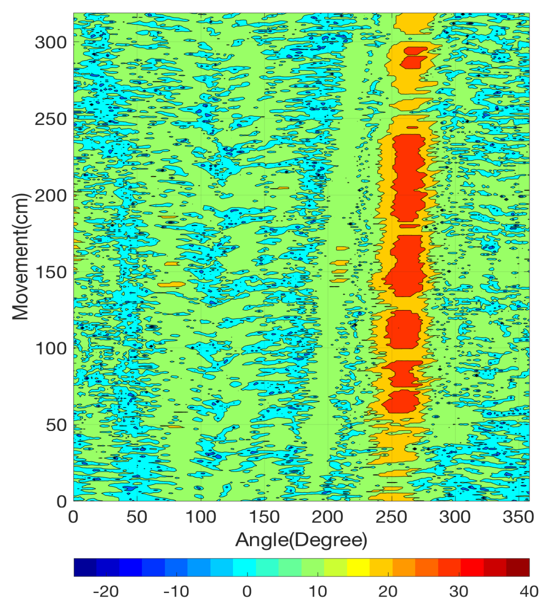

(b) Heatmap

Figure 2.3: Heatmap of NLOS measurement in the Indoor Environment

- It is easy to observe the 'ridge' in both maps, which indicates a strong incoming signal from certain angle. The ridge is approximately linear in the map and shift slowly along the movement. This means that the best beam alignment direction should be properly adjusted in dynamic case. Comparing the ridge areas between these two figures, the LOS is about 20dB stronger than NLOS one, which also agrees with the literature.

- The heatmap of LOS displays some unique properties. The most noticeable fact is two strong ridges exits— one LOS path and one first reflective NLOS path. Besides these, the signal of other azimuth angles is relative weak compared with NLOS.

- NLOS has only one 'ridge'. However, the heatmap demonstrates that other angles have incoming signal such as $25°$, $75°$ and $200°$. If the LOS path is not available due to blockage or other reasons, a NLOS could provide an alternative way to maintain the link and it displays rich multi-path properties.

Besides that, the motion sensing is also done with the experiment. The receiver is rotated by 90 degree and the rotation is compensated by simple gyroscope measurements. With adequate initial calibration, the accumulated error with time is less than $1°$/min. Given the fast-dynamic nature of wireless communication, this is well enough for angle compensation. For sensor fusion algorithms, the details will be given in the later chapter.

2.5 Conclusion

In this chapter, a cost-efficient mmWave testbed with motion sensing is provided and compared with previous testbed in the literature.

The limitation relies on the mechanical horn antenna. The inertia of mechanical action module is much larger than the electronic steerable phased array and the beam searching capability is too limited for the real time application. As a result, the development of a compatible phased array antenna would be a great add-on component to the system.

Part I

Mobility management

Chapter 3

Motion Sensor Aided Beam Tracking for Mobile Device in mmWave Communications

3.1 Introduction

Directional communication is an indispensable component in the mmWave communication. With directional communications, data transmission is plausible only when the transmitter and receiver discover the mutual existence and identify the relative direction, as illustrated in Fig. 3.1.

However, a perfect beam alignment between the transmitter and receiver needs fine-tuning and is vulnerable to different factors such as mobile device movement. Theoretically speaking, a narrower beam could concentrate more energy to one direction and thus achieve better throughput, whereas the searching time is much longer. A narrower beam needs accurate alignment; thus, a slight misalignment could significantly degrade the antenna gain. This severely complicates the communication protocol design in the medium access (MAC) layer. The link establishment and maintenance under static scenarios have been well studied in existing researches, yet the static model is hardly realistic in real mobile networks.

Therefore, the beam tracking process is necessary to proactively correct the beam direction, which inevitably creates ineligible overhead.

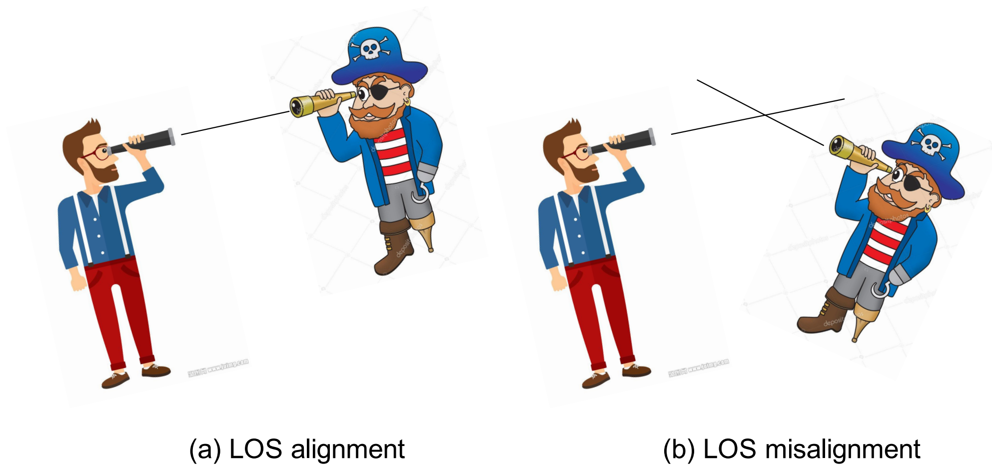

Figure 3.1: Partner searching with beams: alignment and misalignment

The angle deviation is hardly avoidable, given the semi-optical characteristics of mmWave. The design for beam tracking can be divided into two categories. One is explicit refinement in the protocol, where the transceiver pair constantly realigns the beam, thus creating system overhead, such as IEEE 802.11ad beam refinement phase. Another strategy seeks additional information, such as history direction, out-of-band spectrum. In paper [62], the authors use out-of-band spectrum for blind beam tracking and reduce 81% overhead, compared with the IEEE 802.11ad system. However, these system designs are mathematically complicated and may be inadequate for low power devices. Moreover, it utilizes the low frequency spectrum that is already overly occupied.

In this chapter, the beam tracking problem is examined from a different viewpoint. Currently, most smart devices are integrated with various sensors for sensing, monitoring and interacting with environment. Among all these sensors, inertial measurement unit (IMU) and GPS are mostly considered as a low-cost motion tracking solution and have been widely used in navigation, positioning and mobile gaming. It is obvious that this ancillary information could improve the performance of beam alignment with implicit feedback and thus reduce the tracking overhead.

The combination of multiple streams of sensor data for a more accurate result is called sensor fusion. As shown in the literature, the accuracy suffers from the drifting and measurement noise in the long run. However, the problem is eased in the beamforming scenario, where the integration time is of relatively short period. The reason is that the mobile network in general requires routinely scheduling for media access and handover and the realignment is necessary process over time. The goal for the beam tracking is to extend the term of validity instead of eliminating the initial access process.

Within the short period, the drift accumulation is negligible. Hence, we only need attitude deviations instead of the information of absolute attitude and position in the global space. The detailed analysis will be given in the next section.

The remainder of this chapter is organized as follows. Section 3.2 will briefly analyze the primary cause of beam misalignment and sensor fusion. The following Section 3.3 elaborates the procedure of beam compensation. Then Section 3.4 will propose a protocol of beam tracking based on the motion sensor compensation. Then experiment and simulation in Section 3.5 will validate the proposed scheme. Conclusions will be drawn in Section 3.6.

3.2 Beam Tracking and Motion Sensing

In this section, the background of beam tracking, misalignment and orientation/heading sensing are covered and explained.

3.2.1 Beam Tracking and Misalignment Analysis

In mmWave communications, the narrow beam is expected to improve the transmission range and spatial reuse, while it may bring severe blindness between the transmitter and receiver. mmWave devices need to discover and then align their beam directions for a reliable communication link. As for mobile networks, the support of mobility is a vital feature. How to initialize and maintain the link in a rapid and robust manner is more challenging in the mmWave spectrum.

In the literature, the beam association starts with the transmitter sending a predefined training sequence. There are numerous approaches to determine the direction for beam alignment in the traditional digital MIMO research, such as Beamscan, MUSIC, beamspace, ESPRIT, subspace methods etc. For analog beamforming, one brutal way is to exhaustively search for the beam space, which introduces extraordinary delay and overhead. In current WPAN and WLAN standards, the beam training period adopts a hierarchy search protocol, which consists of multiple phases. It is initiated by a coarse alignment and then followed by refinement. The overhead scales up with the number of mobile devices, as well as transmit and receive beam patterns. All these methods can identify the optimal weight for the radio frequency (RF) frontend in digital beamforming and the switching pattern in analog beamforming. As the cost for beam association is prohibitive, the tracking process becomes a vital ingredient in the whole recipe.

In this chapter, it is assumed that, after the initialization of beam alignment, both ends can identify the optimal beam directions. After the beams aligned, a rapid tracking mechanism needs to be built. The beam misalignment could be caused by position movement or attitude rotation in the LOS condition as showed in Fig.3.2. For instance, in IEEE 802.11ad, the narrowest beam width could be less than 3 degrees, given the division of 128 sections. As for human movement, the average human walking speed is 5km/h (1.388 m/s). For the time frame of 100ms and 10m distance between base station (BS) and user equipment (UE), the relative angle misalignment is only 0.75°, which is well covered by the beam width. However, the angle rotation severely deteriorates the link budget. The experiment in [80] also proved that the small-scale fading is relatively negligible for mmWave. However, a slipped phone could easily lose the beam alignment within such a short time. Based on the study in [62], a 70° rotation could cause 5 mismatches in a second. To maintain a robust connection, substantial training overhead is expected for mmWave communications.

Another scenario is high-speed mobility; e.g., a UE is inside a high-speed vehicle. In a typical outdoor circumstance, we assume that the distance between BS and UE is 100m. Then given the 3° constraint, the coverage length is about 5.23m. Given the time frame of 100ms, it is equivalent to 188km/h, which could cover most of the current vehicle speed. Once again, this estimation demonstrates that the relative position is a secondary effect, while the angle deviation is the most critical factor for beam tracking. Experiments in Section 3.5 will validate our analysis.

In summary, the primary factor of the beam misalignment in mmWave is self-rotation. This deviation can be mitigated given the awareness of self-motion.

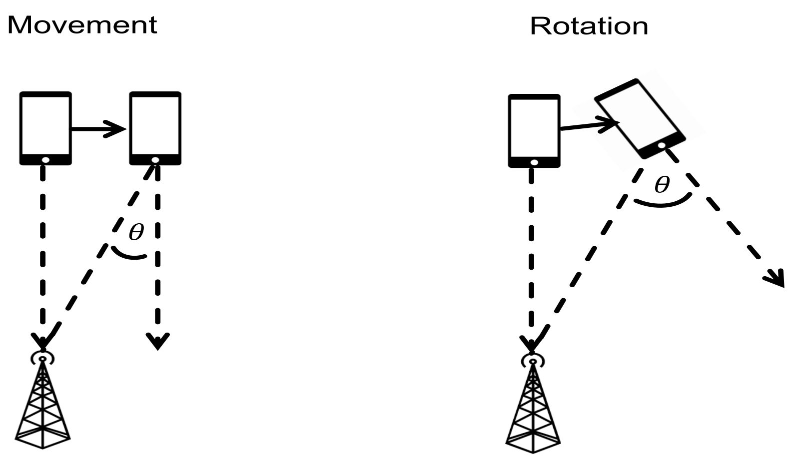

Figure 3.2: Motion misalignment in beamforming

3.2.2 Motion Sensing and Sensor Fusion

Thanks to the rapid development of low-cost micro-electro-mechanical-system (MEMS), most mobile smart devices provides an inexpensive kinematic solution, which contains three key components — accelerometer, gyroscope and magnetometer for various applications. These sensors can be the cornerstone to extract the absolute attitude in the space with Sensor fusion algorithm in mmWave communication.

- Accelerometer: Accelerometer measures the force including gravity exerted on the object. It is a sensitive sensor which could capture the movement such as tapping or small vibration. Yet it could be extremely noisy in a short term, rendering it useless unless a proper low pass filter is applied to extract the information.

- Gyroscope: Gyroscope measures the angular velocity in the sensor frame. The attitude is acquired by the integration of measurement over time. Gyroscope is reasonably accurate over a short time, while the drifting issue makes it inaccurate due to the integration over time. This problem could be mitigated by the technique of sensor fusion.

- Magnetometer: Magnetometer detects and measures magnetic field. The magnetometer offers a great option to measure the absolute orientation in the earth frame, since it could tell the orientation of north. However, the disadvantage is also obvious that the magnetic north pole does not match the geographic one. Moreover, the direction varies based on the nearby materials which could substantially affect the magnetic field.

Combing the sensory measurements from different source, the result could contain less uncertainty and provide more reliable results and such process is called sensor fusion. Integrating three motion sensors could provide sufficient information for the absolute orientation in the space for the beam angle compensation, while their disadvantages can be mitigated by the input of others.

In the existing studies, numbers of methods have been proposed for sensor fusion. The most direct rotation compensation strategy is to apply the gyro measurement only for the rotation cancellation. To fix the drifting issue, Mahony filter [56] is widely applied as a benchmark algorithm by correcting the rotation. Another interesting algorithm in [55] is designed by Madgwick, who formulated the fusion as a minimization problem. These methods are all compared in the latter section.

3.3 Frame Transformation and Beam Misalignment Compensation

As the beam misalignment is closely related to the orientation of mobile device, the tracking algorithm based on IMU need a proper mathematical framework to represent the orientations of different frames (coordinate systems).

3.3.1 Quaternion Representation of Orientation

In the 2-dimensional spaces, the rotation matrix dominates the representations of rotation as a optimal choice. However, the rotation in 3-dimensional spaces has many possible representations, each of them own their unique advantages in different scenarios. For the altitude and spatial rotation of mobile device in our case, a convenient choice is the quaternion. The advantage of quaternion involve combining subsequent rotations (and equivalently orientations), easy interpolating between rotations and robust to rounding error (easy renormalization compared with rotation matrix).

A quaternion is mathematically defined as $\mathbf{q} = a+bi+cj+dk$ where a, b, c, and d are real numbers and i, j and k are imaginary units. By constraining the magnitude of quaternion such that $\|\mathbf{q}\| = 1$, it can be used to represent an orientation (rotation relative to a reference coordinate system). In additional to that, a pure quaternion $\bar{\mathbf{d}} = 0 + d_x i + d_y j + d_z k$, which further null the real part as $a = 0$, could represent a directional vector $\mathbf{d} = (d_x, d_y, d_z)$ with unit norm. The multiple rule for two quaternions $q_1 = a_1 + b_1 i + c_1 j + d_1 k$ and $q_2 = a_2 + b_2 i + c_2 j + d_2 k$ is defined as:

$$
\begin{aligned}
q_1 q_2 = & a_1 a_2 - b_1 b_2 - c_1 c_2 - d_1 d_2 \\
& + (a_1 b_2 + b_1 a_2 + c_1 d_2 - d_1 c_2) i \\
& + (a_1 c_2 - b_1 d_2 + c_1 a_2 + d_1 b_2) j \\
& + (a_1 d_2 + b_1 c_2 - c_1 b_2 + d_1 a_2) k.
\end{aligned}
\tag{3.1}
$$

The product of two quaternions represents combining subsequent rotations, which can be considered as the integration of cumulative rotation over time.

Given the above definition, a rotation operation by $\mathbf{q}$ on a direction vector $\mathbf{d}$ is given by

$$
\bar{\mathbf{d}}' = \mathbf{q}\bar{\mathbf{d}}\mathbf{q}^{-1}, \tag{3.2}
$$

where $\mathbf{q}^{-1} = a - bi - cj - dk$ represents the conjugate of $\mathbf{q}$. More details of quaternion operation can be refereed to [99].

3.3.2 Global and Local Frames

With directional communication, both transceivers need to maintain the beam alignment. In fact, transmitter and receiver only recognize the optimal direction in their own frame, where the coordinate transformation $\mathbf{q}$ to the global coordinate is unclear unless detailed geological position and accurately environment model are given. Considering the fact that analysis is easier under the global frame, but compensation is achieved by the mobile device itself, it is necessary to study the transformation between two frames.

In the following part, global coordinate g is fixed at the location of BS and the origin point is arbitrary located at the BS. The definition of global frame could save one more definition of local coordinate of BS as BS is usually static during the communication. The optimal beam direction D is given as mutual directions within the global frame provided the positions of the UE and BS. Besides the global frame, another frame called local coordinate system l is attached to the mobile device rigidly and rotates with the device itself. All the sensors in the mobile devices are working in this frame, while the antenna array is also placed in a certain plane in the local frame. The relationship is showed in Fig. 3.3. The global and local frames are distinguished by the subscripts g and l.

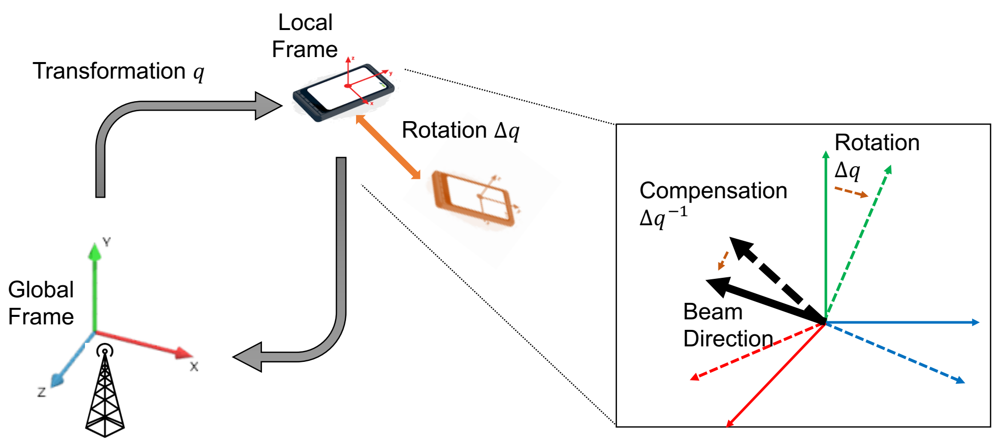

Figure 3.3: Beamforming Misalignment Compensation

In the subsequent discussion, compensation for the misalignment is achieved without knowing the condition of global frame. The benefits are multifold. Although the measurements in the local frame could be used to estimate the attitude and position for the mobile device in the global frame, given more information from GPS and detailed real time environmental model, this process is computationally heavy to maintain in real time and is prone to all drifts and noises. Moreover, if the distance between the UE and BS is inaccurate, especially in the non-LOS (NLOS) case, the compensation of pure movement is impossible. Another persuasive argument is that an accurate long-time tracking is unnecessary at the presence of fast switching LOS/NLOS environment. A computationally inexpensive yet fast responsive compensation mechanism is much preferable in such dynamical scenarios.

3.3.3 Beam Misalignment Compensation

With above definition, the beam misalignment compensation follows the procedure below:

1. For an antenna array, the beam direction will be translated from the azimuth angle $\alpha \in [0, 2\pi)$ and elevation angle $\beta \in (-\frac{\pi}{2}, \frac{\pi}{2})$ in the spherical coordinate to a unit direction $D_l(0)$:

$$D_l = \begin{bmatrix} X \\ Y \\ Z \end{bmatrix} = \begin{bmatrix} \cos(\beta) * \cos(\alpha) \\ \cos(\beta) * \sin(\alpha) \\ \sin(\beta) \end{bmatrix} \tag{3.3}$$

   The above equation is for the uniform square planar array in 3D space. For uniform linear antenna arrays, only the azimuth angel is used and $\beta = 0$.

2. Periodically, the UE updates the acceleration $\mathbf{a}_l(t) = (a_x, a_y, a_z)$, angular velocity $\omega_l(t) = (\omega_x, \omega_y, \omega_z)$ and magnetic field $\mathbf{m}_l(t) = (m_x, m_y, m_z)$ at time t. During a period δt, the local frame has reached a new state, as illustrated by the dotted frame in Fig. 3.3. To estimate the rotation $\Delta\mathbf{q}_l$ of the local frame, it is necessary to calculate $\Delta\mathbf{q}_l(t) = S(\mathbf{a}_l(t), \omega_l(t), \mathbf{m}_l(t))$, where S maps the sensor measurements to the rotation estimation. For the simplified misalignment compensation, only the gyro measurement is applied. The angular velocity to the frame rotation in this period δt is converted as:

$$\begin{aligned} \Delta\mathbf{q}_l(t) &= \cos\left(\frac{\delta tn}{2}\right) + i\frac{\omega_x}{l}\sin\left(\frac{\delta tn}{2}\right) \\ &+ j\frac{\omega_y}{l}\sin\left(\frac{\delta tn}{2}\right) + k\frac{\omega_z}{l}\sin\left(\frac{\delta tn}{2}\right), \end{aligned} \tag{3.4}$$

   where $n = \|\omega\|$ in radians. The gyro measurement can be further corrected using all sensor measurements and sensor fusion algorithm, based on which $\Delta\mathbf{q}_l$ is refined.

3. To compensate the beam deviation, the beam direction in the local frame $D_l(t-1)$ shoule be tuned back to the previous angle. Since the conjugate of a unit quaternion

is the opposite rotation, this operation can be written as

$$\bar{\mathbf{D}}_l'(t-1) = \mathbf{\Delta q}^{-1}\bar{\mathbf{D}}_l(t-1)\mathbf{\Delta q}. \tag{3.5}$$

4. Finally, the optimal direction could uniquely determine the optimal tuning parameters for different antenna arrays, while this unit direction vector D_l on the sphere can be converted to

$$\begin{bmatrix}\alpha \\ \beta\end{bmatrix} = \begin{bmatrix}\arctan(y_l/x_l) \\ \arctan(z_l/\sqrt{x_l^2+y_l^2})\end{bmatrix}, \tag{3.6}$$

where the angles α and β can be used to steer the beam direction.

3.4 Misalignment Compensation Protocol

Above compensation algorithm can only cover the mobile user without any occurrence of blockage. However, blockage is an inevitable negative factor to be considered in the mmWave MAC layer design. Therefore, a modified MAC protocol is given in this section to cover both contents.

3.4.1 Review on mmWave Protocol

Considering the case that BS is stationary, two main causes for the beam direction variation are the UE movement and environment variation. Since the BS will coordinate all links within the cell and the beam alignment is a resource intensive task, the primary goal of the protocol is to reduce the overhead and partly transfer the workload to the UE to alleviate the burden on the BS. In the analysis, it is assumed that the overhead of re-initialization is much more expensive than incremental beam refinement.

The IEEE 802.11ad is analyzed here, whose timing structure is given in Fig. 3.4, for instance. This scheme can be adopted to cellular networks as well. To reduce the system overhead, IEEE 802.11ad adopts an in-packet training procedure in the beam refinement phase, instead of a packet by packet approach. After the association, one party, either BS

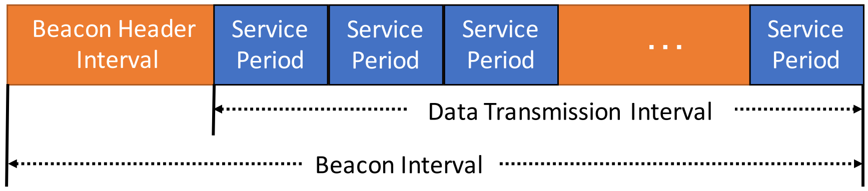

Figure 3.4: A Simplified Beacon Interval Frame of IEEE 802.11ad.

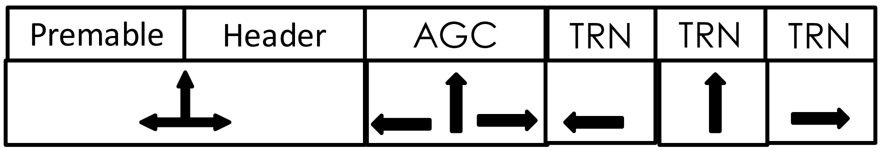

Figure 3.5: In-packet Training in the Beam Refinement of IEEE 802.11ad. (The arrows means the directions.)

or UE, will propose a training request in the header and then receive a training sequence, as illustrated in Fig. 3.5, where a set of directions are evaluated. Then the optimal beam is fed back to the initiator. This is called the Tx beam refinement; Rx training follows the same procedure. It is obvious that the refinement overhead scales linearly with the cardinality of the direction set, thus creating heavy overhead for narrow beam systems prone to misalignment. Therefore, a novel scheme, which could fit into the current protocol with a minimum explicit training request, is proposed here.

3.4.2 Motion and Blockage Aware Mac Protocol

In the proposed scheme illustrated in Fig. 3.6, the new protocol adapts two new modules, namely the sensor-aided compensation module and the blockage detection module. At the beginning of one beacon interval, each link initializes by following the default setup, where the antenna array will lock the azimuth and elevation angle (α, β) and convert to the direction vector D_l. At the beginning of each service period, the UE will first apply the compensation strategy to update the antenna beam direction, using the above misalignment compensation method. During this period, it receives or transmits the data to this new direction. In this process, the SNR will be monitored for further analysis. This procedure may continue, given a stable SNR, until the end of the beacon. If the SNR drops significantly, it proceeds to a new beam searching.

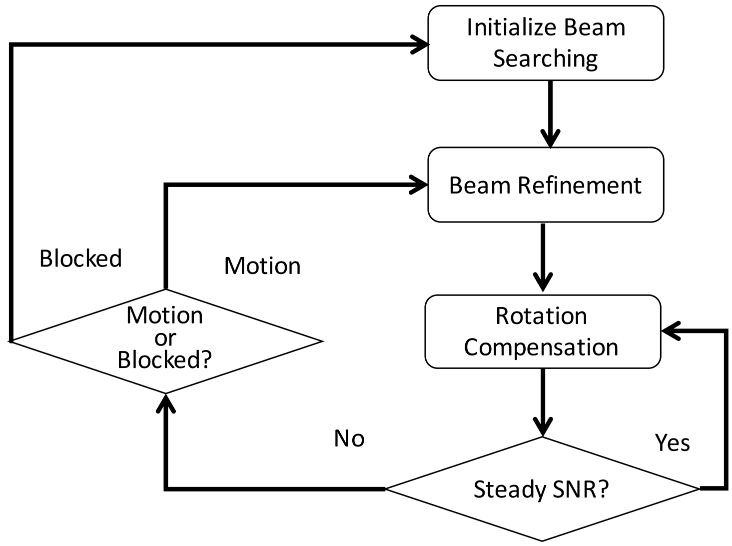

Figure 3.6: Proposed scheme of beam tracking

Do We Need Long Time Tracking?

In [13], authors provided the experiment result of attenuation loss with human blockage effects. From the prospect of communication systems, the shadowing effect is strong in amplitude (20dB), short in the rising time (in the order of tens of ms) and long in fading duration (100-300 ms). With an uncontrollable environment, the attenuation loss of mmWave channel may encounter multiple changes within one second. Tracking one direction for long term seems to be an unwise strategy.

3.5 Experiments and Simulations Result

In this section, the setup and several experiment results are explained with IMU and optical benchmark. Then several simulation results are discussed.

3.5.1 IMU Measurement

The UE is considered as a free rigid body in the 3D space. Therefore, motion tracking measurements are captured by an iPhone 6 and the result is compared with an optical tracking system called Optitrack [59]. The configuration of Optitrack is shown in Fig. 3.7a, where six infrared cameras are evenly located on the roof of a room to guarantee that there are three available cameras at any time. On the cell phone, three infrared reflective markers are fixed at the shell for tracking as shown in Fig. 3.7b, providing the real-time position and attitude information. This optical tracking system offers a benchmark with error less than $\pm 0.1mm$ for the true attitude and tracks the position in the global frame with an update rate of 100Hz.

IMU sensors in iPhone are set in the push mode with the update rate of 100Hz for the acceleration, angular velocity and magnetic field. One thing to be notice is while the maximum rate of iOS system is upper bounded by 100Hz. For pure chip-level sampling, the maximum speed could reach several thousand per second.

In the initial phase of record, the phone is raised slowly in the vertical direction for three times and then laid flat on the desk for several seconds, which is used to synchronize the record between the UE and the optical tracking system. These data can be used to construct two typical scenarios in the following simulation.

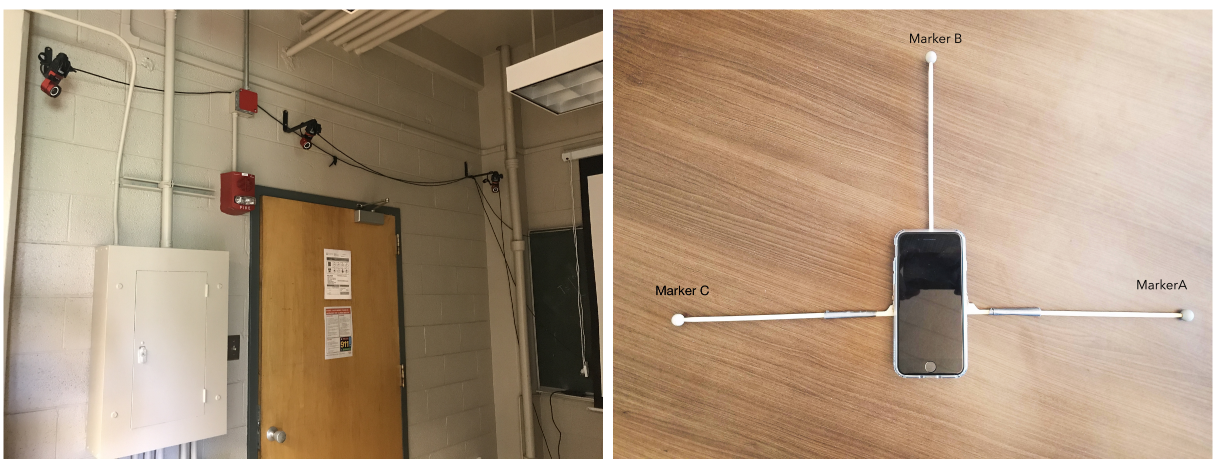

(a) Optical Tracking System **(b)** Marker Arrangement

Figure 3.7: Benchmark Test

- Sitting Mode: The tester sits on a rotating chair and watches videos on the mobile device. The tester can randomly change his direction. Later, he browses Internet with an app where multiple clicks are recorded.

- Walking Mode: The tester holds the phone near his ear and then listens to the phone, while walking within the room. Due to the limited space, the straight-line walking period is short, whereas the walking speed is about $1.5m/s$.

3.5.2 Calibration Optical Benchmark

The three markers are fixed on a case and arranged as an isosceles right triangle where A_g, B_g and C_g denote the corresponding positions of markers in the global frame. To track the trajectory and orientation of the local frame, we assign the direction vector of X-axis of local frame $\vec{X}_l$ as $\vec{X}_l = \frac{A_g - C_g}{\|A_g - C_g\|}$. During the recording procedure, the relative position could vary due to measurement error. To overcome the deformation and maintain the orthogonality between axis, we define a central point denoted by M, which lies between A_g and C_g and satisfies $\vec{Y}_l = \frac{B_g - M}{\|B_g - M\|} \perp \vec{X}_l$. The third axis $\vec{Z}_l$ is given by the cross product $\vec{Z}_l = \vec{X}_l \times \vec{Y}_l$. These constructs a right-handed frame for the local coordinate system. This definition coincides with the iPhone sensor coordinate and thus simplifies the analysis further. The center point M is considered as the central point of the antenna array. Its trajectory is the movement of UE in the global frame.

In order to compare the angle deviation in the experiment, the normalized beam direction is well-defined in the global frame. The transformation quaternions between two frames are given by $\mathbf{q}_{g\to l}$ and $\mathbf{q}_{g\leftarrow l}$. The real time optimal beam direction defined as the direction from the central point on UE to the BS, namely

$$\mathbf{D}_g = \frac{M - BS}{\|M - BS\|}, \tag{3.7}$$

where BS is the center of the BS antenna array.

The beam direction in the local frame can be converted to the global frame as $\hat{\bar{\mathbf{D}}}_g = \mathbf{q}_{g\to l}\bar{\mathbf{D}}_l\mathbf{q}_{g\to l}^{-1}$. Finally, the compensation error need, which is beam deviation between $\mathbf{D}_g$ and $\hat{\mathbf{D}}_g$, is given by

$$\delta D = \arctan\left(\frac{\mathbf{D}_g \times \hat{\mathbf{D}}_g}{\mathbf{D}_g \cdot \hat{\mathbf{D}}_g}\right). \tag{3.8}$$

3.5.3 Beam Misalignment

Considering the beam direction is the result of relative position between two ends, two scenarios are further constructed based on the distance to the BS.

- Outdoor Environment: As the era of mmWave mobile network, the cell range shrinks to 100-200m. Therefore, the setup for the outdoor simulation is assumed that the BS is located 100m away from the UE at the height of 5m.

- Indoor Environment or NLOS mmWave communication: The second case is that the BS is extremely close to the UE, which is around dimension of indoor space. Another possible scenario is that for the NLOS communication, the signal will be reflected by nearby obstacle such as concrete wall or glass.

In the following analysis, the beam tracking algorithm assumes a uniform antenna gain among the main beam. Nevertheless, the gain varies among beams in the practical systems, this simplified assumption still could earn insight for future design.

During the simulation, one beacon interval of the IEEE 802.11ad timing frame consists of 10 service periods, each lasting 10 ms to match the previous experiment. For every 10 service periods, the angle deviation are calculated between $\mathbf{D}_g$ and $\hat{\mathbf{D}}_g$.

In Fig. 3.8 and 3.9, the maximum angle deviations with and without the sensor compensation are recorded and compared for all scenarios. In general, the largest angle misalignment without the compensation after 10 service periods is around $10 - 15°$. Given such a high deviation rate, the connection could easily be lost for several times in one second. On the contrary, the pure gyro-based compensation strategy will keep the angle error under $3°$. This translates to a considerable reduction of the beam refinement training time. The second observation from these results is that the angle deviation caused by movement is a minor factor in the short term. This result could ease some concerns that we need complicated tracking mechanism for the motion caused misalignment. The last but not the least, Fig. 3.10 illustrates 15,000 realizations of the angle deviation with respect to the service periods. In most cases the angle deviation is increasing with time, while one can also find some situations in which the angle deviation actually decreases with time.

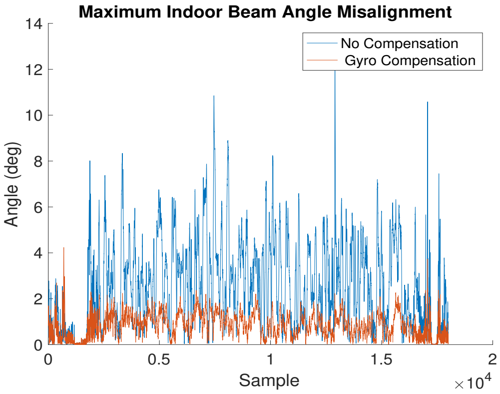

(a) Indoor in Walking Condition

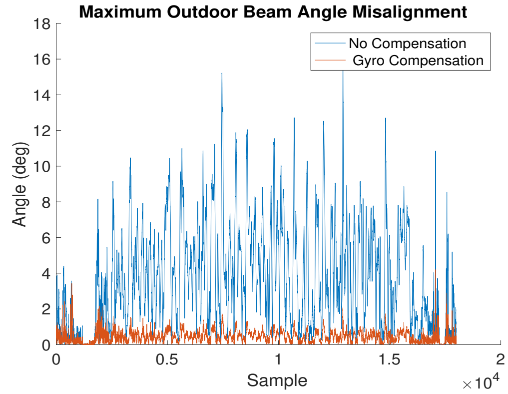

(b) Outdoor in Walking Condition

Figure 3.8: Angle deviation in the walking condition

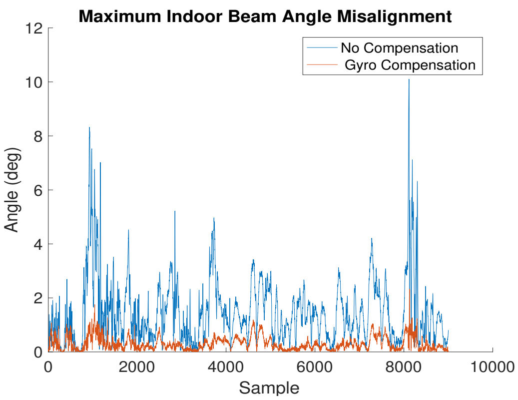

(a) Indoor in Sitting Condition

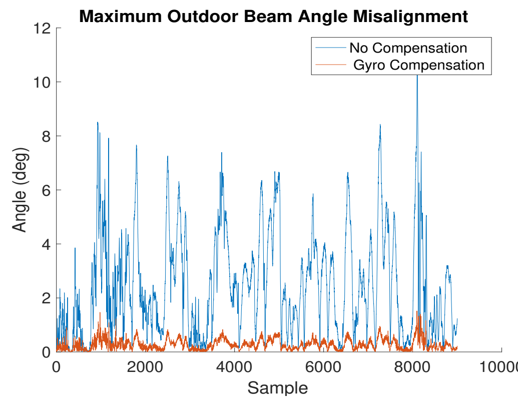

(b) Outdoor in Sitting Condition

Figure 3.9: Angle deviation in the sitting condition

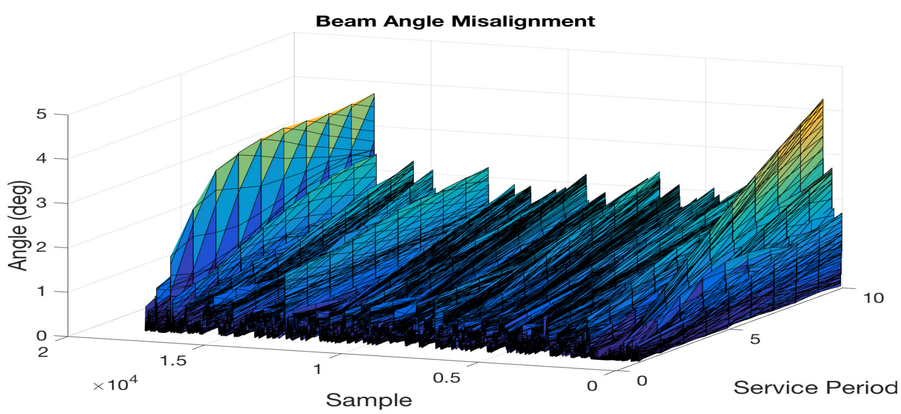

Figure 3.10: Trend of angle deviation over service periods and starting point.

A detailed statistics of angle deviation is shown in Table 3.1. Beginning at each sampling point, the beam is assumed to be aligned perfectly. Then the angle deviation of next 100 service periods are calculated given the sensors measurements. Δ is the threshold of angle deviation to loss the signal. When the angle deviation is larger than Δ, it can claim that the beam tracking is failed. The mean and standard deviation of the first hitting time of the threshold (i.e., the time of the loss of tracking) are recorded. It is clear that the less dynamical cases (sitting) has a longer expectation of the hitting time (which can be considered as the reliable tracking period). The probability of different hitting times with respect to Δ is showed in Fig. 3.11. It is clear that the probability is very low unless Δ is very small.

Table 3.1: Experiment Statistics

Scenarios	Walking				Sitting			
	Outdoor		Indoor		Outdoor		Indoor	
Δ	Mean	σ	Mean	σ	Mean	σ	Mean	σ
1.00	38.28	34.24	27.34	33.62	62.95	35.58	44.75	32.65
2.00	67.93	32.70	38.83	33.04	89.50	23.29	69.93	29.91
3.00	84.63	25.35	49.01	31.37	95.91	15.38	84.53	22.99
4.00	92.46	17.89	58.49	29.52	98.56	9.11	92.74	16.46
5.00	96.40	12.25	66.53	27.27	99.50	5.30	96.87	10.57
6.00	98.43	8.03	73.68	24.54	99.85	2.66	98.70	6.48
7.00	99.54	4.42	80.03	21.38	99.96	1.41	99.59	3.86
8.00	99.88	2.12	85.76	17.98	100.00	0.00	99.81	2.32
9.00	99.98	0.64	90.48	14.25	100.00	0.00	99.94	1.02
10.00	100.00	0.00	94.18	10.76	100.00	0.00	99.98	0.56

3.5.4 Comparison of Different Filters

In Fig. 3.12, three sensor fusion strategies, namely gyro only, Mahony [56] and Madgwick [55] filters, are compared in the walking condition. From the compensation result, two sensor fusion filters indeed achieve a better tracking accuracy in general. However, no free lunch is available, since more computation resource is consumed for these two strategies. Another negative factor in the filter design is that the hyper-parameters in the filter need fine-tuning. Performance degradation does exist due to inappropriate parameters. The last point is that the history attitude is involved in the angle correction. The directions of gravity

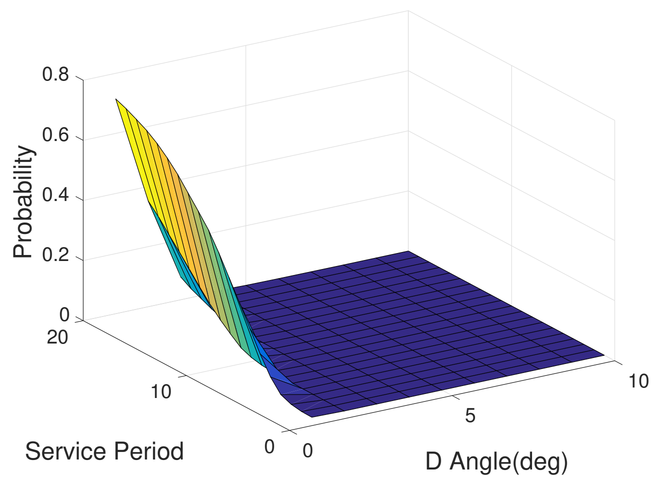

Figure 3.11: The probability of different hitting time of the angle deviation threshold (the loss of tracking) at different service periods in the outdoor walking condition.

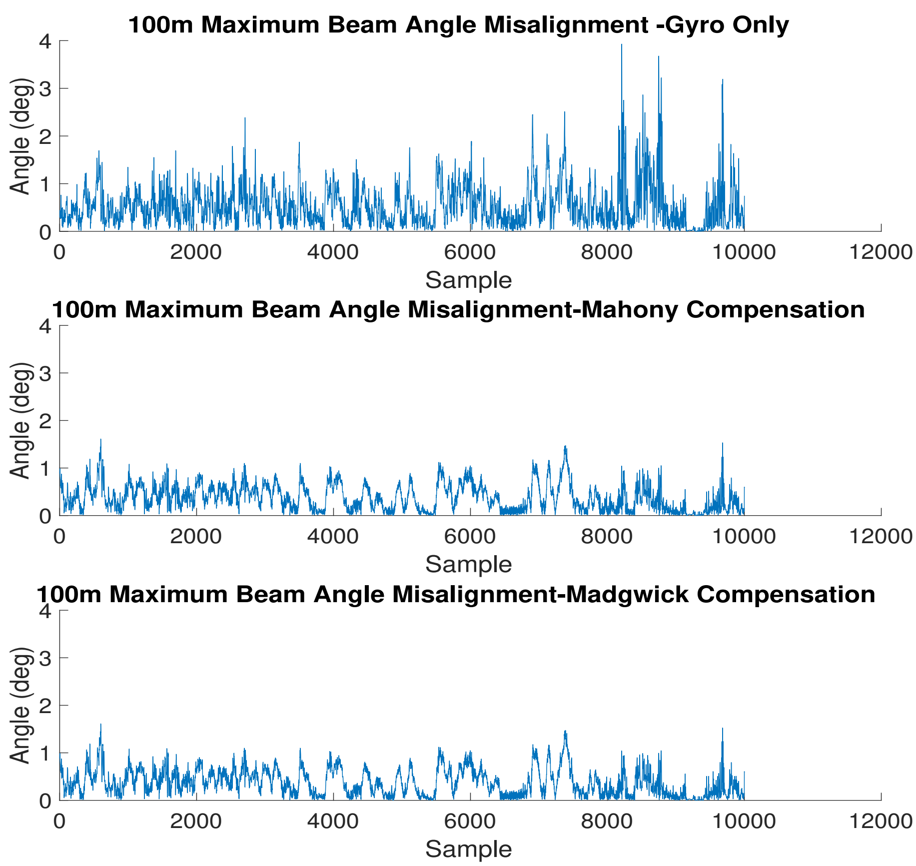

Figure 3.12: Comparison of Compensation using Different Filters

and north are calibrated throughout the process. When the measurements are interfered by the environment, the angle calibration will be inevitably distorted for extended period. Therefore, the compensation strategy should be determined by the system requirement such as the beam width and system cost.

3.5.5 Overhead Reduction

As what is mentioned above, all the active beam searching, and beam refinement induce overhead to the system. Again, the IEEE 802.11ad are applied the overhead assessment. Based on IEEE 802.11ad, a 5% system overhead is expected for a single UE due to the beam alignment refinement. For multiple users, the overhead will add up to a tremendous fraction of all resource as the user number increases.

In this simulation, each beacon interval contains n service periods. The beam direction is compensated by the sensor measurements. We also set up different thresholds for the maximum angle deviation. When the beam is beyond the angle threshold, a new beam refinement procedure is required. Fig. 3.13 shows the overhead reduction ratio between the compensation and non-compensation schemes.

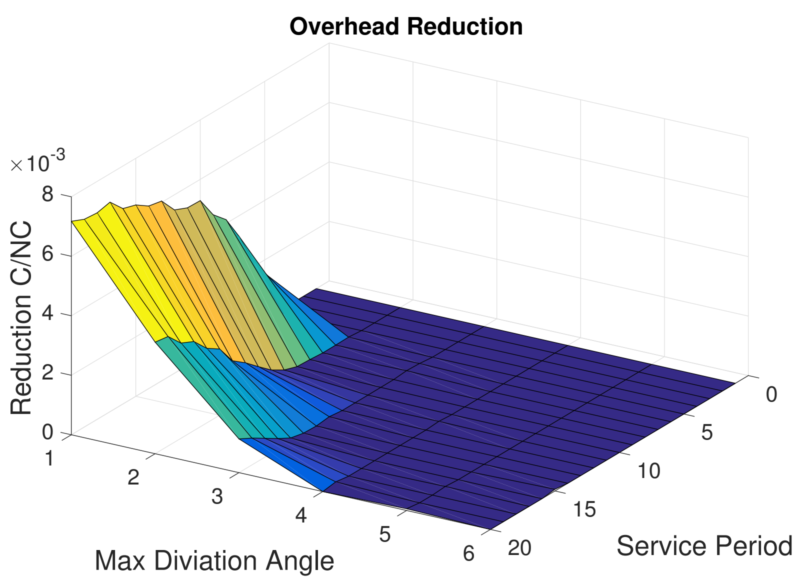

Figure 3.13: Overhead reduction for different thresholds

It is obvious that the compensated scheme almost eliminates all the beam refinements in most cases. Even under the most stringent requirement (1° for 20 service periods), the sensor compensated scheme only consumes 0.7% overhead compared with the non-compensation strategy. This simulation implies that the sensor-aided tracking scheme be a strong competitor in the beam-tracking protocol.

3.6 Conclusions

The directional communication requires a tighter wireless bond between nodes. While the mobility renders the mmWave communication prone to angle misalignment with beamforming. In this chapter, the primary factors of misalignment are analyzed and identified during the beam tracking procedure. Then, the necessity and benefit of introducing the information of motion sensor in the beam tracking is further testified. To reduce the heavy overhead, sensor-based correction method for the beam direction is proposed and merged into a modified MAC Layer protocol. In the experiment phase, the sensor compensation is compared with an optical benchmark and the results prove the effectiveness of sensor-based beam tracking. Moreover, the discussion about different sensor fusion algorithms is followed. Finally, the comparison of the overhead reduction in IEEE 802.11ad can demonstrate the efficiency of our proposed scheme.

Chapter 4

Multi-connectivity Using Erasure Code for Reliable Transmission

4.1 Introduction

In mmWave communication, either blockage and mobility could create an intermittent connection over relatively short time. In addition to that, the dense deployment of mmWave pico cell network requires more frequent handoffs, if any blockage is detected or the device is in high speed roaming. Another notorious problem with mmWave is the costly initial association during the cell searching and initiation procedure[3]. One blockage event could create a large latency if a passive handoff is inevitable.

One potential solution to improve the robustness and quality of service (QoS) is multi-connectivity[32]. Simultaneously maintaining connections with multi-cell base stations has been showed to considerably reduce handoff failure and improve QoS[66].

Multi-connectivity, naming Dual Connectivity (DC), has been introduced since LTE ver.12 [7]. The integration of macro cell and small cell allows one user to be served by both base stations, with the operations of different carriers[77]. In the era of 5G new radio (NR), the high spatial multiplexing of semi-optical mmWave allows high frequency multiplexing between cells, which can eliminate the constraint of orthogonal carriers. Therefore, the multi-connectivity can be a powerful weapon to combat the volatile environment of mmWave[47].

One drawback of DC in LTE is the complicated control and data plane in the backbone during the handoff or dropout [21]. Upon handoff, undelivered downlink data needs to be forwarded to the new eNodeB for sequential data transmission. In the LTE paradigm, the probability of sudden dropout due to blockage is relative rare; yet it is not necessarily true for the mmWave case. The intermittent link condition dramatically intensifies the workload within the backhaul, and creates a large latency during buffering operations.

To leverage the power of new spectrum, a simplified backhaul scheme for multi-connectivity is an interesting topic. As shown in previous researches[14], the link condition in mmWave can be characterized by a two-state random process switching between the line of sight (LOS) and blockage. This link model resembles the classical erasure channel, where one single bit (packet) may be either received or erased. Therefore, a solution based on the erasure code is proposed in this paper to simplify the backhaul design and minimize the need for the feedback of ACK. Here we adopt a rateless code, namely the Raptor code[88], for the efficiency of transmission over multiple links with simplified packet offloading mechanism in Fig. 4.1. As the first successful fountain code, the original data, encoded by the Raptor code, could be successfully recovered with a subset of unordered symbols (packets), and thus the erased symbols can be safely ignored if a blockage occurs, which is the key for the backhaul simplification. To the best knowledge of authors, this is the first research on the multi-connectivity based on the coding design.

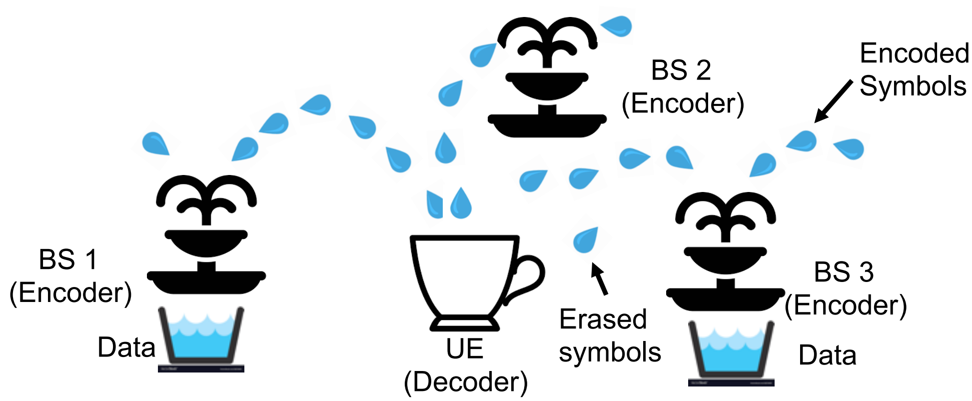

Figure 4.1: Multi-connectivity with fountain code.

The remainder of the chapter is organized as follows. Section 4.2 provides the basic principle of multi-connectivity and raptor code. Section 4.3 outlines the backbone design assumed in this study, as well as the benefits of adopting an implicit feedback mechanism. Section 4.4 presents all the channel measurements with the analysis of blockage statistics. Then the simulation results on the system performance will be presented in Section 4.5. Finally, conclusions are drawn in Section 4.6.

4.2 Multi-Connectivity and Fountain Code

The next generation mobile network will be supported by both the evolution of previous microwave network and novel techniques such as mmWave. The combination of both incurs unique challenges. In this section, we briefly revisit these concepts and identify new problems.

4.2.1 Data Transfer in Multi-Connectivity and Handoff

The proposal of multi-connectivity stems from the consideration of robustness and throughput. In 4G LTE networks, DC is defined such that a user equipment (UE) can be configured to utilize radio resources from different eNodeBs with possible distinct schedulers. The eNodeBs are connected through X2 interfaces to exchange handoff command or undelivered data, where any of them can act as a master (MeNode) or a secondary (SeNode) node. The benefits can be discussed in three scenarios:

- user-plane aggregation.
- control plane/user plane separation.
- uplink/downlink separation.

This paper will focus on the first topic. The DC architecture in LTE is described in Fig. 4.2 in two schemes. The downlink data in the first scheme will be routed directly to two eNodeBs with less pressure on the X2 backhaul in a static environment. When mobility is considered, the frequency of switching between multiple secondary eNodeB is tremendously high, in heterogeneous networks where a macro eNodeB has tight integration with micro cells or pico-cells. In such a scenario, the second scheme is a better choice, where all the data stream is first routed to the master node and transferred to the secondary node. The pressure on the backhaul over the X2 interface is intense in such a case. Another drawback with one more hop will introduce an extra latency due to the X2 interface latency and limited buffer space. As a result, an efficient flow management mechanism of data among cells will play a key role.

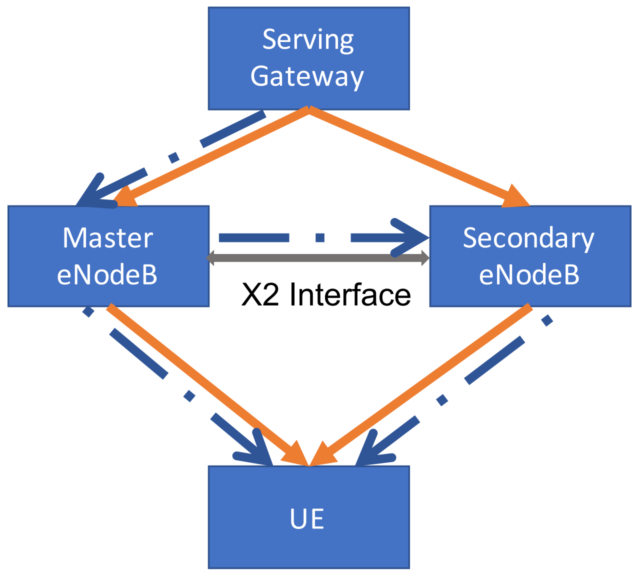

Figure 4.2: Two DC architectures, where the orange solid and blue dotted arrows correspond to architecture types 1 and 2, respectively.

Another problem involving the buffer redistribution is the handoff procedure. A detailed handoff is explained in Fig. 4.3 with the X2 interface. Depending on the two handoff modes, seamless or lossless, the buffered data in the source eNodeB needs to be forwarded or abandoned. When the target eNodeB acknowledges the handoff request from the source eNodeB, the data packet from core network will start to arrive at the target eNodeB, and the packets processed are abandoned in the source eNodeB in the seamless mode. When the time sensitivity is the primary concern, this mode offers the best performance of latency when the packet loss is tolerable. On the contrary, when the lossless handoff is activated, all the packets processed in the MAC layer are forwarded to the target node. Thus, the UE will wait until the buffered data is forwarded to the target node if the events of blockage happened on one link. This introduces a larger latency, while the in-sequence data transmission is guaranteed.

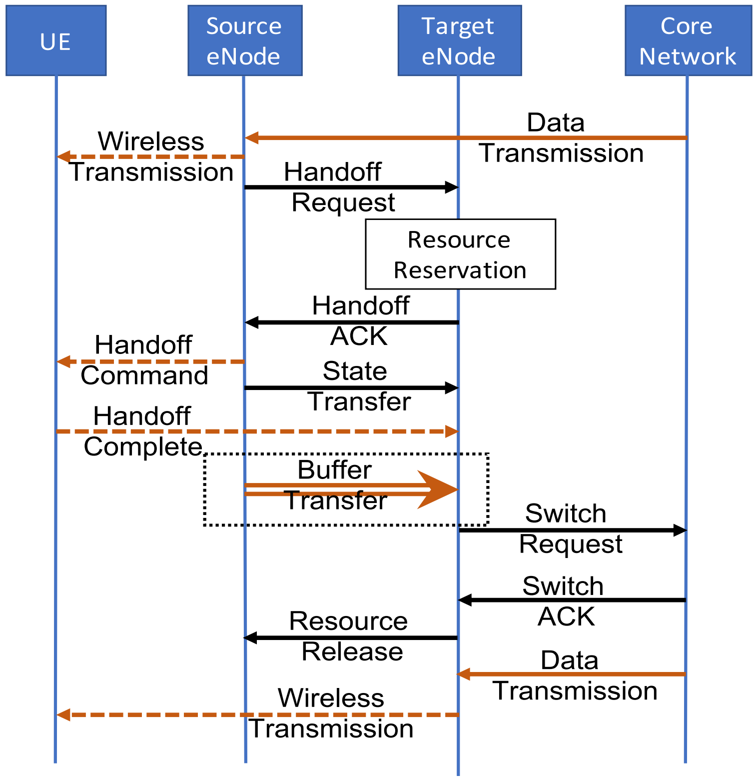

Figure 4.3: The time scheme of handoff procedure. The doted block is optional.

The link reliability in mmWave becomes worse than the microwave counterpart. As a result, the chance of handoff increases dramatically, because of the significant probability of blockage. The large latency or packet loss nullifies the performance gain of multi-connectivity. As the following contents show, the fountain code could mitigate the intense data transfer problem.

In the remainder of this paper, we assume that an mmWave UE can maintain simultaneous transmissions with multiple eNodeBs; and a heterogeneous network exists with a microwave macro cell and mmWave pico cells. When the environment becomes complicated and difficult to provide stable coverage, the control channel will still adopt the traditional microwave for a reliable cell search and resource management, since it is less prone to blockage and has less path loss.

4.2.2 Fountain Code and Applications

Fountain code is a metaphorical fountain that produces infinite symbols (water drops). A given data piece can be encoded into endless stream of packets. Formally speaking, the fountain code for a set of k input symbols (packets) $(x_1, \ldots, x_k)$ can generate an unlimited steam of output symbols (packets) $z_1, z_2, \ldots$. These output symbols (packets) have unique ID numbers and are produced independently and randomly, according to a distribution on $\mathcal{F}_2^k$. For the receiver, a decoding algorithm can recover the original k symbols from any set of n output symbols with a high confidence.

The first practical fountain code is the LT code[54], where the key for its success is the robust soliton distribution used for generating the random distribution. Then the next generation of fountain code, called raptor code, further reduced the decoding cost with a two-layer coding and decoding structures[88]. Considering the rateless and adaptive nature with arbitrary binary erasure rate, the raptor code has been integrated in 3GPP MBMS standard for broadcast file delivery, and different streaming services such as one way satellite broadcast [96].

In general, there is no ACK mechanism in broadcasting service due to efficiency concerns[51]. However, given a time constraint, the multi-connectivity system design will benefit from the knowledge of link states to reduce the packet loss over blocked link and in-time transmission for the next data block. The saved system resource could serve other UE within one network. In the next section, we propose our own control channel scheme for efficient ACKs with raptor code.

4.3 Blockage Aware Multi Connectivity

For reliable communications, the positive ACK or negative NACK provides the necessary integrity for the sequential data segment, and initiates a re-transmission with lost packets. In general, Raptor code in mutli-link transmission does not require sequential data transmission and thus eliminates the necessity of ACK. In this section, we attempt to use limited feedback to boost the system performance.

4.3.1 Reliable Communications with Implicit ACK

The request for feedback is discussed in several prospects. Firstly, the advantage of fountain code is the elimination of re-transmission request for lost packets and capability of generating infinite symbols. However, the UE can attempt to decode original data block once the number of received symbols is more than sufficient. If decoding is completed, the UE should ask for the initialization of the next data block to avoid the waste of radio resources. The second argument for the feedback originates from the blockage occurring to one link. In spite of the fact that the UE can safely ignore the erased packets sent from the blocked channel, it is necessary to inform the corresponding eNodeB to backoff a certain time to wait for the recovery of link, and meanwhile the BS can serve other UE with available frequency-time slot. This backoff time is an implicit NACK mechanism. In details (the notation is defined in Fig. 4.4), the UE holds a backoff state W_b. When a symbol received from one link is erased, the UE should update the backoff state W_b with backoff increasing function $W_b = f_{inc}(W_b)$, refresh the self backup timer T_b and notify the macrowave coordinator about the T_b through a reliable control channel. The corresponding mmWave eNodeB and UE will wait until the backoff timer is cleared for a link restoration. Upon recovery, W_b is updated with backoff decreasing function $W_b = f_{dec}(W_b)$. Unlike the ACK in TCP, there is no need to re-transmit the erased packet, thanks to the nice properties of fountain code. This significantly simplifies the backhaul design and workload during the handoff.

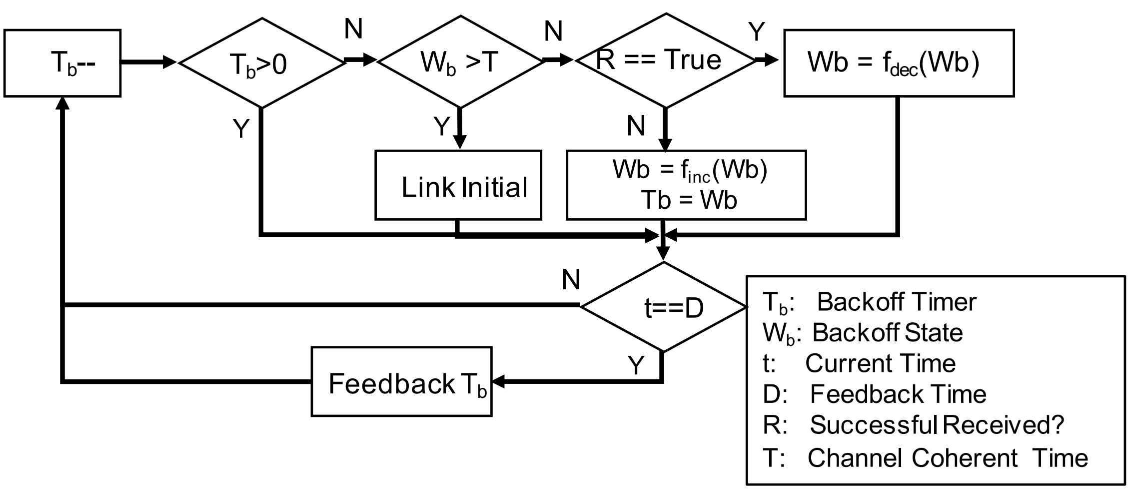

Figure 4.4: Dynamic data offloading: distributed encoding

In addition to that, the backoff scheme should be further discussed depending on the backoff states. If the backoff time surpasses the channel coherent time T, the link condition is unknown to the UE, and thus the link initialization is a must. On the contrary, a simple transmission attempt may still be valid under the same channel condition. The field experiment in the next section will demonstrate the efficiency in an mmWave channel.

4.3.2 Instant Feedback vs Routine Feedback

The channel quality is the baseline for the success of wireless communications. In general, an instant feedback offers the best system performance with a minimum packet loss. However, the radio resource in the mobile network is scheduled by the base station, and feedbacks are scheduled in advance. Therefore, it is better to consider the impact of latency in the feedback design.

In this paper, we consider a routine feedback with a period of D. For the event of erased symbols detected at time t, the local backoff timer T_b will be refreshed. If $t + T_b < D$, the local backoff timer still counts down, whereas the receiver is in the idle state temporarily. No backoff report is fed back if the link is recovered before D. Otherwise, the UE will report its current backoff time T_b at time D to the macro eNodeBs. Combing all the factors, we propose a blockage-aware ACK mechanism as shown in Fig. 4.4 for the mmWave multi-connectivity.

4.3.3 Dynamic Data Offloading in the Backbone

With user plane multi-connectivity, the segmented data is distributed into the buffers of different eNodeBs, and no duplicated packets exist between each other. Therefore, the unsent contents in the buffer need to be transferred in the adversary conditions. However, each symbol (or packet) with fountain code is generated independently from the original data block in a distributed manner, as long as the random seeds are the same. This would allow two possible data offloading schemes.

For the first scheme in Fig. 4.5a, the data block will be duplicated into mmWave eNodeBs. Then each eNodeB can work independently to encode different symbols with distinct symbol

ID numbers with UE. For instance, if one data block requires n symbols, then eNodeBs $i = 1, 2, 3...$ can generate symbols with ID $n(i-1), n(i-1)+1, n(i-1)+2....$

The second scheme requires that the macro cell directly distribute different encoded symbols into the mmWave eNodeB buffers as in Fig. 4.5b. This simplifies the workload in the pico cell but requires a tighter integration between the macro and pico cells. The second scheme also works with the setting of a single eNodeB with multiple remote radio heads.

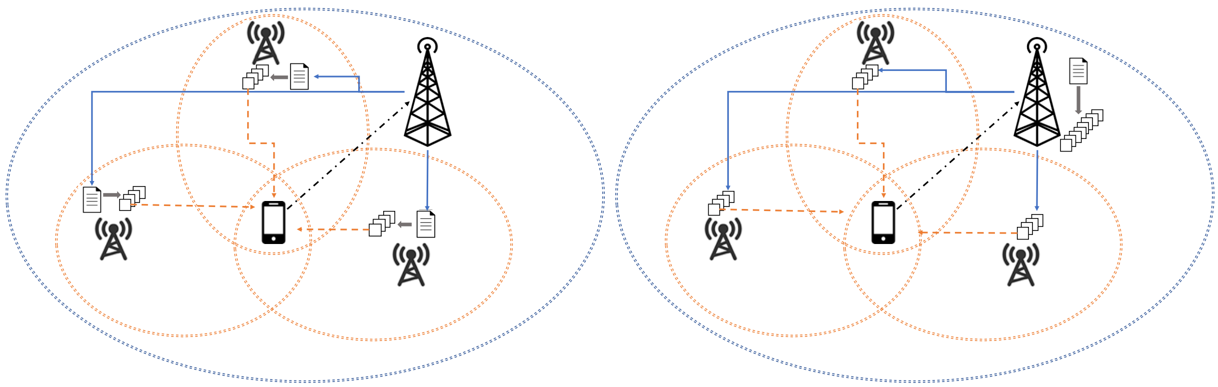

(a) Distributed Encoding **(b)** Centralized Encoding

Figure 4.5: Dynamic data offloading

In conclusion, mmWave is vulnerable to blockages. The simple real-time feedback with channel condition is time-consuming. With fountain code, the overhead of feedback is minimized in the multi-connectivity because there is no requirement for the re-transmission for the erased packets. The UE and pico eNodeB will reach an agreement with a UE-defined backoff time. In such a manner, the radio resource can be allocated for other urgent need and improve the efficiency with the best effort on the throughput.

4.4 Multi-Connectivity Experiment

To verify the efficiency of the proposed protocol design in a multi-connectivity setting, the mmWave channel condition with multiple links is captured with a customized mmWave testbed in the 60 GHz band in Fig. 4.6. It consists of an HMC6300 board at the transmitter and an HMC6301 board at the receiver. Two Quinstar pyramidal horn antennas are mounted

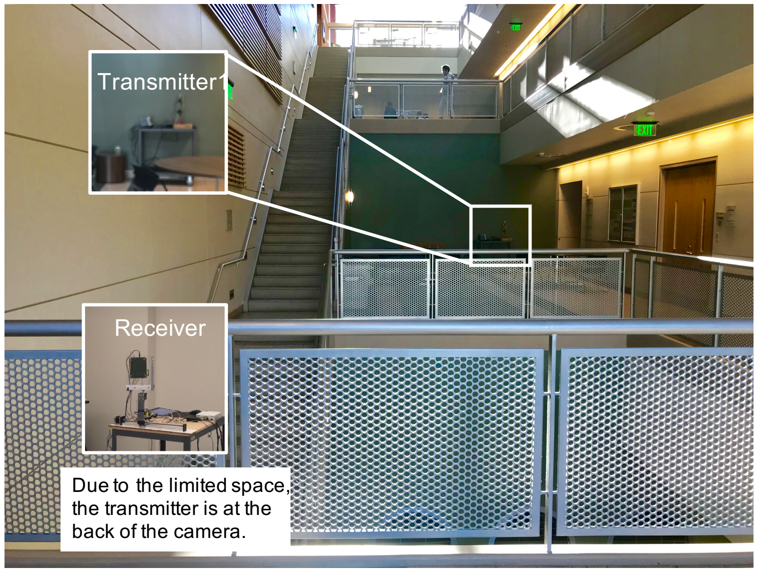

Figure 4.6: The Experiment in the Hall Way of Min Kao Building, University of Tennessee.

to the transmitter and receiver. More details of testbed can be found in our previous chapter. 2.

The experiment is conducted in the hall way in the EECS department of the University of Tennessee, where the transmitters are located in three different positions, and the receiver is fixed at one spot. The floor plan is given in Fig.4.7. Based on the floor plan, it is obvious that the LOS paths exist in three links. With limited multi-connectivity capability, the received signal strength (RSS) is measured in three days at the same time period to synthesize a multi-connectivity channel condition. The time granularity of RSS is 0.5ms per sample. The gain of both ends is fixed in the experiment and may exaggerate the link blockage loss. Nevertheless, the channel condition will only be better with more dynamic gain settings.

4.4.1 Channel Measurement and Statistics

The salient advantage of multi-connectivity is the robustness, compared with single link outage caused by blockage. The recorded RSS is shown in Fig. 4.8, and the total numbers of available links in Fig. 4.9 strongly support this assumption. From Fig. 4.8, it is obvious that link 2 suffers denser but weaker blockages than the other two links, because one person walking along the corridor can block the bouncing signal for multiple times. However, during the experiment, an interesting observation is that the optimal direction of link 2 is not strictly

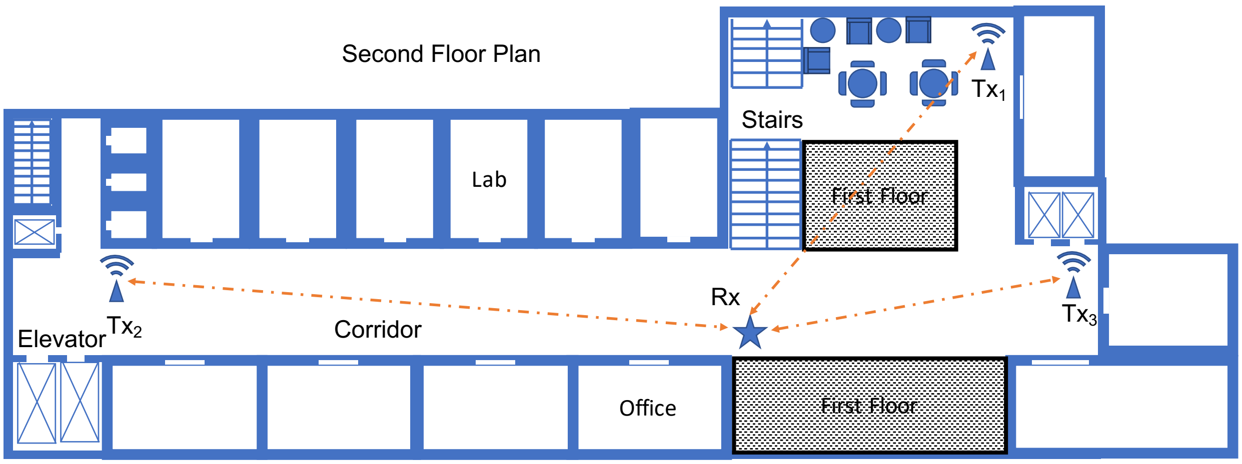

Figure 4.7: Floor plan in the experiment and the positions of TX/RX nodes.

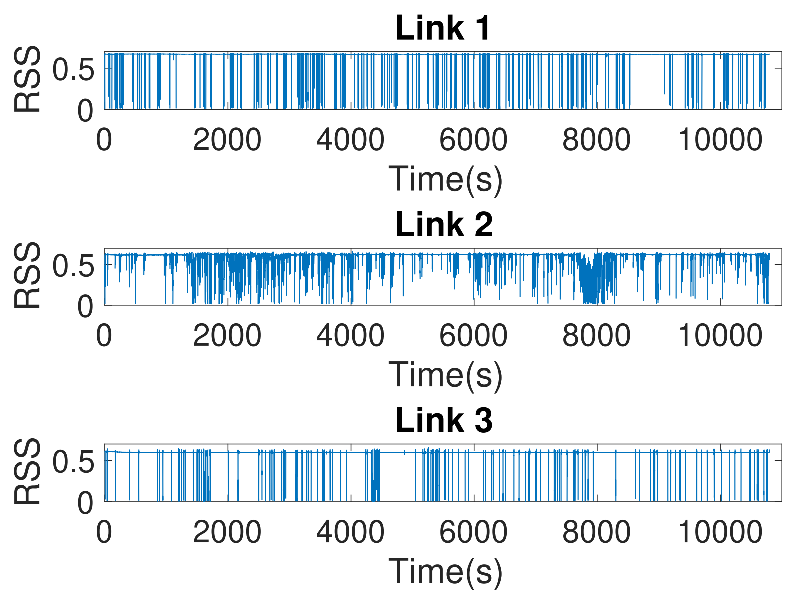

Figure 4.8: Received signal strength over 3 hours over three links.

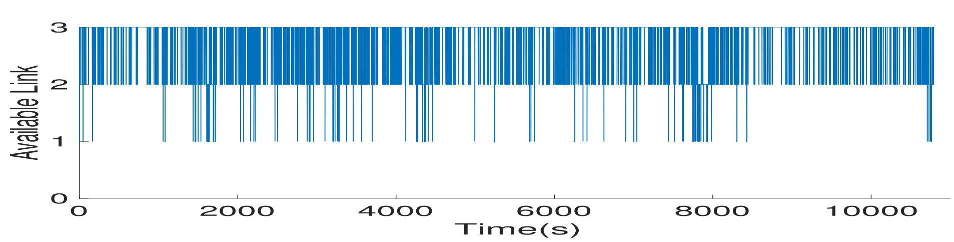

Figure 4.9: The number of available links over 3 hours.

LOS. The reason could be that the corridor is too long and narrow for the beam width of 10°, such that the corridor is gradually filled with signal with increasing distance to the transmitter. Finally, part of the energy will be bounced back by the wall, which causes multiple path interference at the LOS direction.

The statistics in Figure .4.10 shows that the outage rates are 2.1%, 11.0% and 3.7% of links 1, 2 and 3 respectively. On the contrary, the failure rate of two-link connectivity is 1.1%,0.63% and 0.47%. If we further extend to the multi-connectivity scenarios with three links connection, the failure rate is 0% during this three-hour measurements. This convincing result means that, given sufficient geographic separation of transmitters, it could guarantee good mutual independence on channel condition and provide consistent communication links.

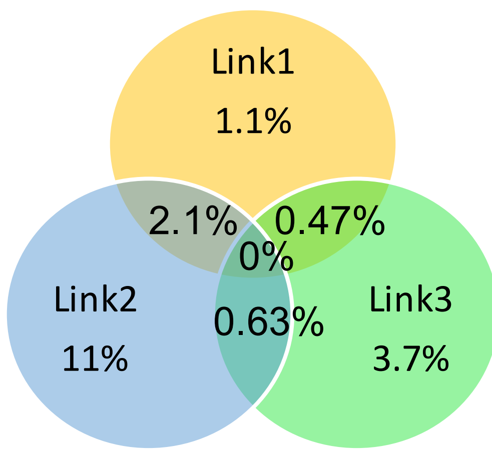

Figure 4.10: Outage Probability over three links.

The details of channel characteristics are listed in Table 4.1, about the expectation of blockage time and arrival time. Here we define the arrival time as the time between the end of the previous blockage event, and the consecutive blockage event excluding the blockage time. It is obvious that some statistics, e.g. variance of arrival time of link 2, could change rapidly over time. This may contradict with some common assumptions about the modeling of arrival rate such as Poisson process. In Fig. 4.11, the histogram of three links clearly demonstrates that they do not fit any well-known mathematical models. The Kolmogorov-Smirnov test confirms that the arrival and blockage times do not follow typical distributions such as Gaussian, exponential, Weibull, Poisson, et al.

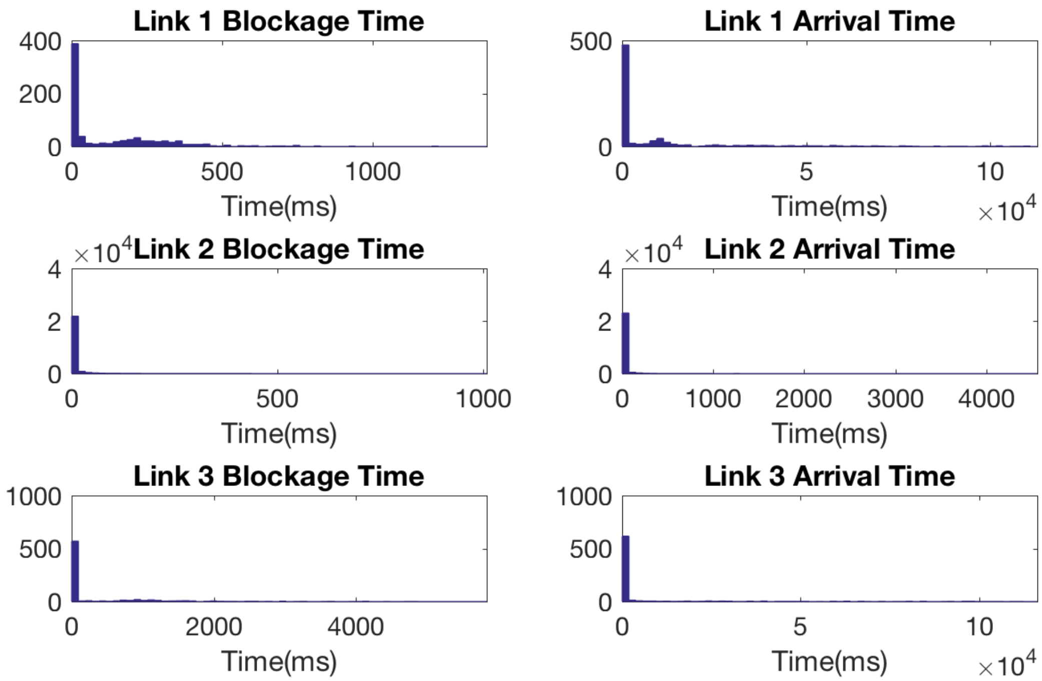

Figure 4.11: Histograms of blockage time and arrival time.

Table 4.1: Statistics of blockage time and arrival time (ms), where a is the arrival time, b is the blockage time, E is the expectation, and σ is the variance.

Hour		Link1	Link2	Link3
1	$\mathbf{E}(b)$	1.580E+02	4.300E+01	5.370E+02
	$\sigma(b)$	1.071E+05	6.653E+05	1.158E+06
	$\mathbf{E}(a)$	1.599E+04	2.740E+02	1.196E+04
	$\sigma(a)$	5.460E+09	3.120E+09	7.455E+09
2	$\mathbf{E}(b)$	1.560E+02	3.400E+01	6.970E+02
	$\sigma(b)$	4.928E+05	2.604E+05	5.232E+06
	$\mathbf{E}(a)$	1.391E+04	4.580E+02	1.343E+04
	$\sigma(a)$	7.884E+07	1.247E+08	1.400E+08
3	$\mathbf{E}(b)$	1.540E+02	7.400E+01	3.090E+02
	$\sigma(b)$	2.056E+07	1.933E+07	1.954E+06
	$\mathbf{E}(a)$	1.266E+04	5.150E+02	1.541E+04
	$\sigma(a)$	6.921E+09	1.002E+10	7.968E+09

4.5 Simulation Result

In this section, a mixed mmWave multi-connectivity simulation is given. We consider a simplified communication system with three mmWave eNodeBs located at the positions shown in Fig. 4.7. The RSS record in the previous section represents three erasure channels, where the erasure time is defined as the time duration of the RSS lower than a threshold. The systematic raptor code symbols with 1024 bytes are generated according to RFC6330 [96]. The three eNodeBs are transmitting raptor code symbols of same data block in a synchronous approach. The feedback latency is fixed at 5ms except in the latency simulation sections.

The system performance is compared with a benchmark where only successful decoding is fed back with no latency. No backoff mechanism is provided and three eNodeBs will transmit symbols until a successful decoding flag is received. We focus on two performance criteria, naming packet loss rate and throughput. The packet loss rate is defined as the total packet loss sent from the three mmWave nodes over the received packets in UE. Moreover, the throughput is the total number of decoded bytes, normalized by the benchmark system throughput.

4.5.1 Backoff Adjustment Scheme

In the simulation, the functions f_{inc} and f_{dec} are defined as

$$f_{inc}(W_b) = \begin{cases} I_e * W_b, & \text{for exponential increase} \\ I_l + W_b, & \text{if increase is linear} \end{cases} \tag{4.1}$$

and

$$f_{dec}(W_b) = \begin{cases} W_b/D_e \text{ if } W_b/D_e \geq 1, \text{and exponential decrease} \\ W_b - D_l \text{ if } W_b - D_i > 0, \text{if decrease is linear} \\ 0 \text{ all other cases.} \end{cases} \tag{4.2}$$

The combination of the above functions result in four backoff schemes. All of them are simulated with captured channel records. The packet loss rate of benchmark is the maximum limit of y-axis in Fig. 4.12. From all the figures, it is clear that any limited implicit feedback scheme will dramatically improve the packet loss rate. Therefore, the compromise on the throughput is emphasized in the comparisons. As is shown in Fig. 4.12, the optimal tradeoff is achieved under the combination of linear increasing/linear decreasing backoff scheme, unlike the linear increasing/exponential decreasing windows congestion control in TCP or expoential backoff mechanism in carrier-sense multiple access with collision detection (CSMA/CD).

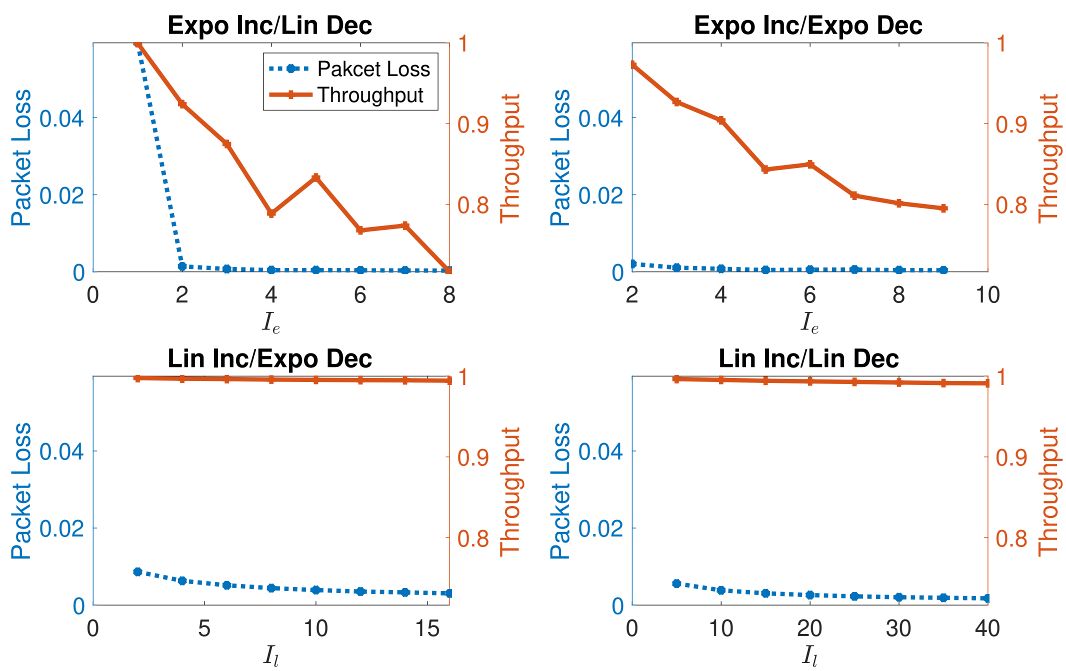

Figure 4.12: Performance comparison of four backoff schemes over different increasing functions f_{inc}. The f_{dec} is fixed in each figure.

Another interesting observation from the simulation is that the choice of D_l orD_e in f_{dec} has little impact on the system performance in Fig. 4.13. We believe that this phenomenon is caused by the distribution of blockage time, which is long-tailed and is almost mutually independent over times.

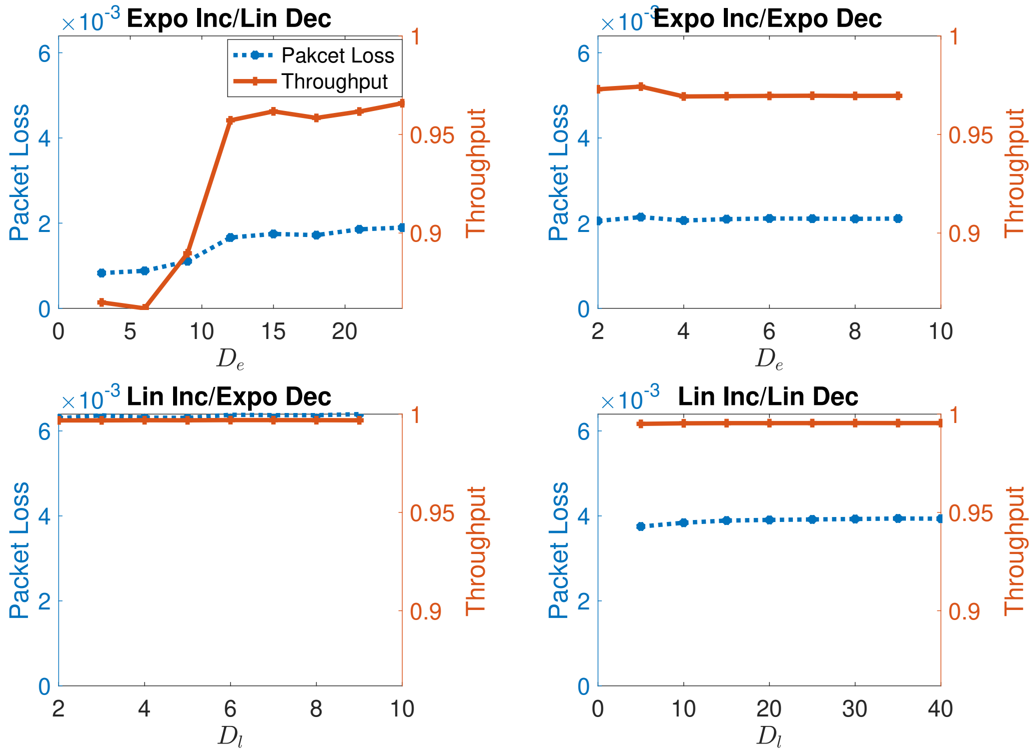

Figure 4.13: Performance comparison of four backoff schemes over different decreasing functions f_{dec}. The f_{inc} is fixed in each figure.

4.5.2 Feedback Delay

The impact of feedback delay is thoroughly examined in Figures 4.14 and 4.15. Fig. 4.14 shows that the latency does have an impact on both packet loss and throughput, while the loss is marginal under the same backoff schemes. If various feedback latencies are compared, both throughput and packet loss rate deteriorate with growing latency. Combining the above simulations, we can safely conclude that the implicit backoff scheme is robust over reasonable feedback latency.

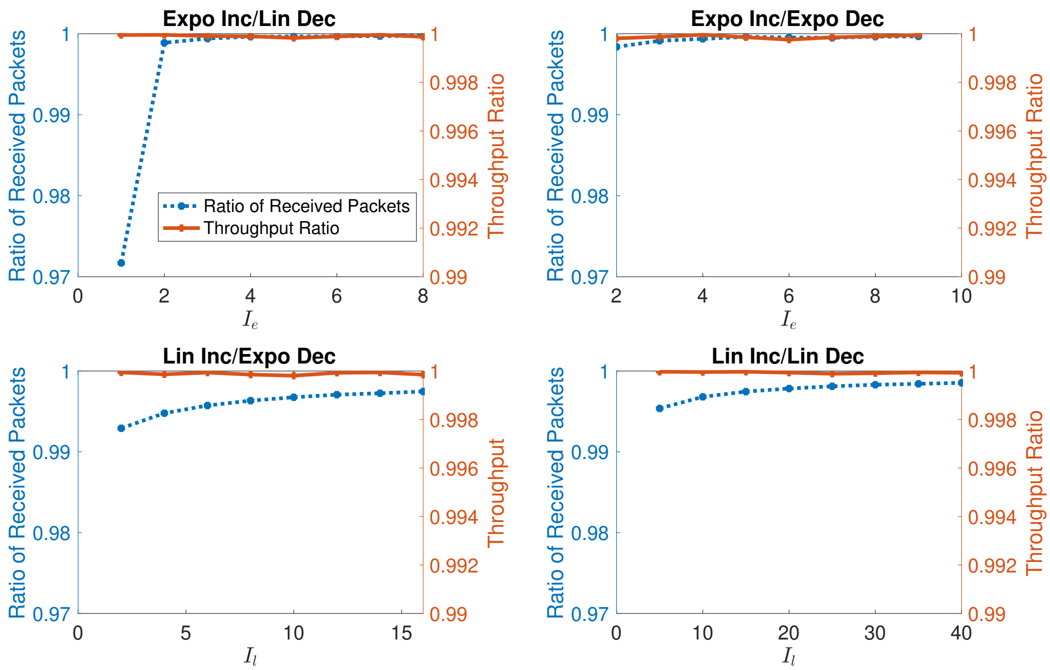

Figure 4.14: System performance comparison between instant feedback and feedback with 5ms latency with same paramters as Fig.4.12. All the ratios in figures are defined as 5ms Latency feedback over instant feedback.

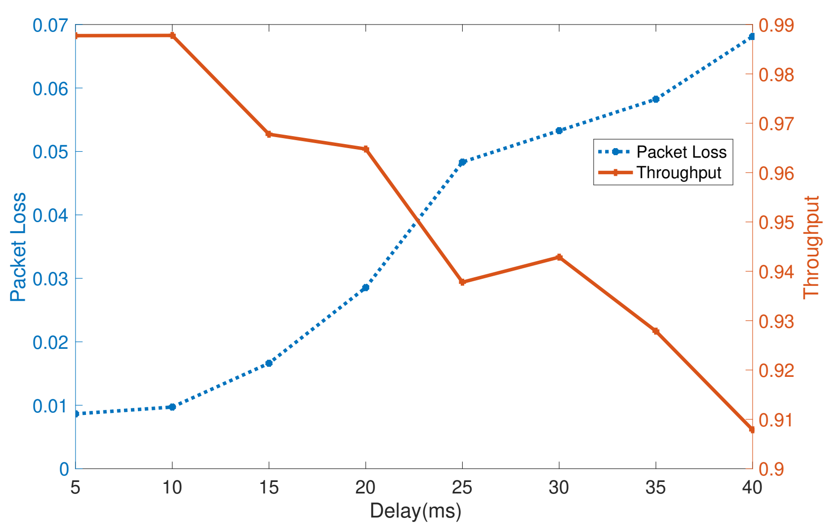

Figure 4.15: System performance comparison over different latencies.

4.5.3 Dynamic Offloading

As shown in Fig. 4.16, the distributed offloading mode requires more symbols for successful decoding. The reason for this is that the first k symbols in the systematic raptor code are the original data. Under good link conditions, the UE can decode with centralized offloading system, while it may require a few more symbols with distributed generation.

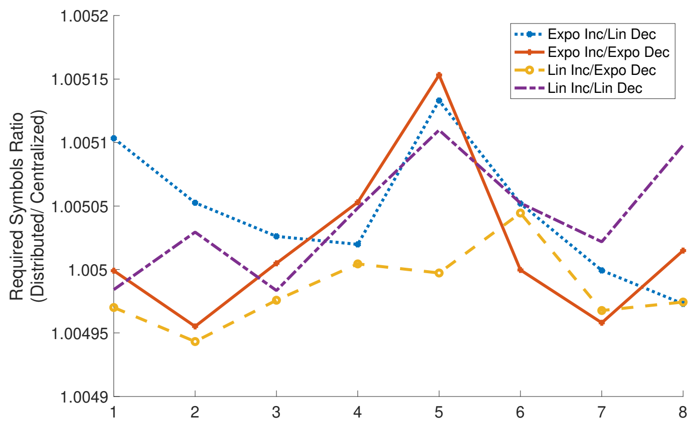

Figure 4.16: The ratio of averaged symbol numbers for successful decoding between distributed and centralized off-loading mechanisms.

4.6 Conclusion

Given the high spatial multiplexing with directional communications, the multi-connectivity is a potential solution to combat intermittent connection and provides robust performance. However, the complexity of backbone network and caching mechanism hinders the implementation in the mmWave band. To simplify the design and enhance the robustness, the fountain code could provide a self-adaptive coding rate to address the randomness of blockage events. In addition to that, a field experiment has been carried out to capture the channel blockage condition in the real environment. The statistics of the mmWave channel have been derived from experiment and have been used in the simulation. The raptor code, which is the most mature fountain code implemented in various protocols, has been utilized for the performance analysis. The analysis of reduced packet loss and associated throughput has been provided to demonstrate the efficiency.

Part II

Blockage Mitigation

Chapter 5

Blockage of Millimeter Wave Communications on Rotor UAVs: Demonstration and Mitigation

5.1 Introduction

Unmanned aerial vehicle (a.k.a. drone) is an airbone system offers a great taste for various new applications, such as geographical measurement, surveillance, civil utility inspection, cargo delivery and environmental monitoring. Moreover, it has been proposed to carry a base station with drone after the extreme weather or severe disasters to aid search and rescue and maintain a reliable communication for disaster recovery services [48].

All above application and potential relies on the wireless communication. On one hand, based on the forecast in 2013 [11], number of UAV service demand will boom in the next 10 years. The crowded low altitude airspace with UAV cause severe interference within both UAV and territorial wireless communication given current technology and spectrum. For applications with high data-throughput or real-time requirements, the conflict between demand and supply urge for the new solution.

To cope with such requirement, mmWave spectrum is an excellent candidate given the fact that a wide unoccupied spectrum is available in a such high frequency band in order to achieve a high data rate. In fact, the new generation of cellular and WLAN already consider extending the territories with new spectrum. In addition to that, the short wavelength of mmWave also enables the integration of larges numbers of antennas on the surface of a single chip, which further enables the implementation of massive MIMO and beamforming that offer a highly directional semi-optical communication link. Combined with these advantages, mmWave could provide high spatial multiplexing capability, translating to extreme high throughput with little interference within limited space, especially suitable for UAV swarm or urban area applications. Therefore, it is only natural to consider mmWave as a potential solution for the UAV communication in the future.

Although mmWave comes with all these benefits, it is challenging to fully utilize these new physical layer advantages in the mobile network, to which UAV Ad-Hoc network is surely belongs. The well-known reason is that mmWave is prone to blockage effect due to the short wavelength, which leaves only LOS for maintain a reliable communication channel between transceivers. This creates a severe and unsolved problem for the UAV communication system. For small and compact rotary UAVs, the arrangement and integration of different modules needs to be delicately designed. Since future UAVs could communicate with both ground or aerial targets, the link direction of mmWave module needs to cover all spherical directions and thus it is inevitably blocked by the certain components of UAV itself in a certain period. This self-blockage may severely deteriorate the performance within a highly dynamic environment. Moreover, the propeller of rotary UAV could also create a highly intermittent link, which result a huge negative factor on the performance. Currently, most researches have been carried out for static indoor environment, while little is known about the outdoor circumstances [14, 72, 105], not to mention the dynamic environment such as air-ground or air-air channels. To the best knowledge of authors, no previous work has been done on the self-blockage in the mmWave band for UAV, despite the experiment in the traditional frequency band [103].

Nevertheless, previous channel measurements still provide insight for the channel modeling. For the loss pattern and incurred by various obstacles, it is more scenario specific. As showed in [14], blockage incurred by human movement is difficult to model in a unified framework. In this paper, to evaluate this blockage effect in the context of UAVs, a series of measurements on the blockage loss due to the fast rotating propeller of UAV are done, which could provide insight for UAV designs as shown in Fig. 5.1. The result clearly demonstrates that the blockage does exit and the loss is significant in certain circumstances, which could severely deteriorate the performance for compact UAVs. In addition to that, the blockage pattern measured in the controlled environment shows the propeller forms a fast varying but periodic channel, just like heartbeat (but much faster). In comparison, the traditional shadowing model in microwave spectrum is only suitable for slow changing while the blockage effect of mmWave communications is much faster, thus forming a unique challenge to mmWave communications in UAVs. Besides these, the incidence angle also has impact on the blockage pattern in the following experiment and the reflective signal also raise concern in the interference control with the existence of UAV propeller.

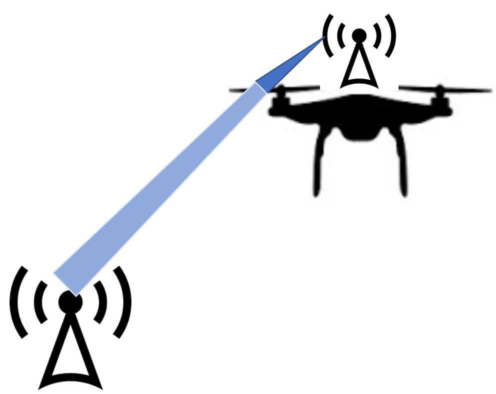

Figure 5.1: UAV Blockage for mmWave Communication. The signal is weakened by UAV propeller

As blockage identified due to a UAV propeller, prediction of the blockage period could mitigate this negative factor given the fact that mechanical system has much more inertia than the digital communication system and thus the blockage pattern can be considered as semi-static. In order to identify the pattern, a multi-channel (each channel corresponds to a subcarrier) quickest detection algorithm is proposed, with the assumption of a multi-subcarrier mmWave communication system, which is a reasonable assumption in modern digital communication system. Each channel computes its p-value using an approximated version as a summary metric regard to the knowledge of blockage. At each time step, the computed p-values are integrated, where the Holm's procedure is applied to determine whether a significant change on the signal strength over different subcarriers has occurred simultaneously. As noted in [93], the Holm's procedure provides a strong control on the family-wise error rate I (FWER I) for a coherent detection given all the SNR conditions of all channels (subcarriers). As will be demonstrated by numerical results, the quickest detection approach will help to detect the edge of blockage and thus identify the blockage pattern. Finally, given the prediction, it is showed that this prediction method could dramatically reduce the overhead for the channel estimation and monitoring for mmWave communication for UAV.

The remainder of this paper is organized as follows. Section 5.2 will explain the propeller blockage measurement and the corresponding experiment results. Then Section 5.3 will propose two approaches for the summary statistic for each subcarriers. Then the next section will discuss how to adopt the Holes procedures for multi-channel blockage detection. Then an adaptive modulation scheme is constructed based on a multi-channel quickest detection for the blockage pattern. Simulations in Section 5.5 demonstrate the efficiency and effectiveness using the prediction algorithm. In the final, conclusions will be drawn in Section 5.6.

5.2 Experiments on Blockage Due to Propeller

Different channel measurement experiments have been done for the static and low speed blockage effects on the mmWave communication. However, no result is available for the UAV except for fixed wing UAV and purpose of high throughput relay. These results are more focused on the high-power transmission over long distance with relatively static link. In this section, several experiment will thoroughly exam the blockage loss, reflection signal and blockage pattern with a rotary UAV.

5.2.1 Equipment and Facilities

In the experiment phase, all the experiments are done with two testbeds. Both of them consist two sub-modules, a mmWave measurement subsystem and a fixed UAV propeller subsystem.

Although it might be more practical to mount the communication system on a hovering UAV on duty, most current UAV platforms do not meet the requirement for maintaining a stable distance for long time. Since the blockage effect of propeller is the main topic here, a propeller fastened securely in position is enough for channel measurement. In this paper, a DJI E1200 propulsion system is mounted firmly on the top of a heavy-duty frame. The carbon fiber two-blade propeller has a thickness about 3mm and the widest part of the blade is around 5cm. The specification can be found in [24]. This subsystem is remotely controlled with five programmed throttle levels. The detailed list of devices is given in Table.5.1.

The mmWave Testbed functions as a channel sounder to monitor the signal strength variation in different situation. To capture the received baseband signal, a Tektronix DPO70404C oscilloscope acquires and stores the waveform measurements for offline analysis. In part of the experiment, the EK1HMC6350 platform is replaced by Tensorcom TC60G transceiver, which is a complete chip set for the 802.11ad compatible transmission solution.

Table 5.1: Hardware Testbed Components

Component	Model
Signal Input	Tektronix AFG3102C
Transmitter	AD HMC6300 / Tensorcom TC60G
Receiver	AD HMC6301 / Tensorcom TC60G
Baseband Sink	Tektronix DPO 70404C
Antenna	WR15 10 Horn Antenna
Propulsion	DJI E1200
Remote Control	MSP 430

5.2.2 Experiment Procedure

The experiment is implemented as shown in Fig. 5.2. A signal source generates a 1MHz sinusoidal baseband signal. This signal is transmitted and converted to the carrier frequency in the 60GHz band. Then a receiver is located 5 meter away from transmitter.

Between these transceivers, the propeller is located between the light of sight (LOS) path. The effective width of the propeller at the LOS is 3cm. It spans an angle of 17°. The mmWave signal is captured by the HMC6301 board and down converted into I&Q-channel signals. Finally, this base-band data is stored in the oscilloscope for signal strength analysis off-line.

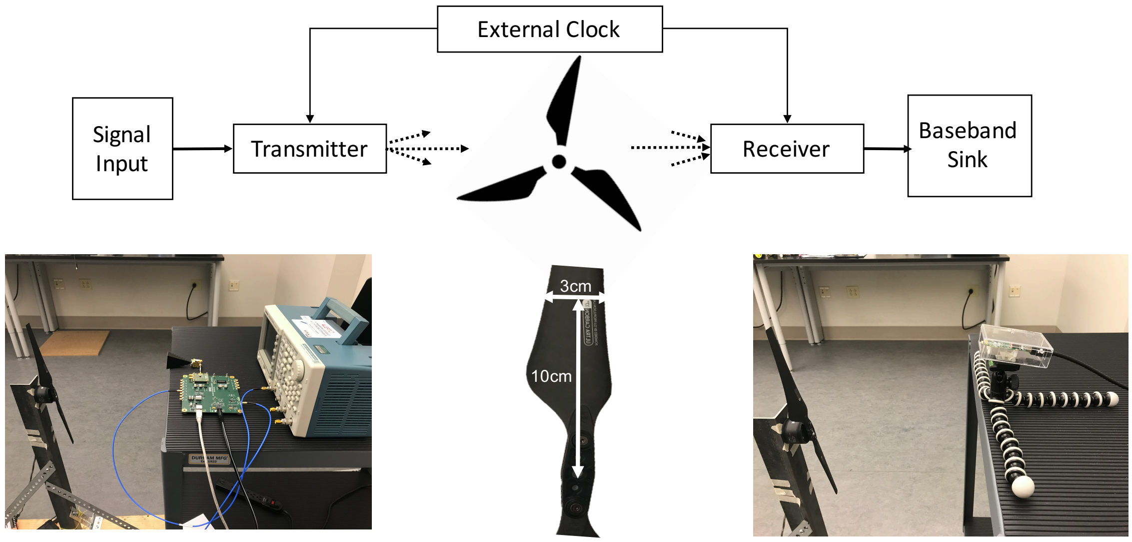

Figure 5.2: Experiment setup: the lower left figure shows the AD HMC 6300 transmitter and the UAV propeller. The lower right figure shows the Tensorcom Platform Test. In the middle is the dimension of the propeller.

The experiments are divided into several stages, namely the blockage loss measurement, the relationship between incident angle and signal strength, reflection angle versus signal strength and the blockage pattern identification.

- Blockage loss: First, a benchmark measurement without blockage is sampled. The ambient noise power, when the transmitter is shut down and no obstacle is present, is recorded with same configuration. Then, a propeller is placed at different distances to the transmitter on the LOS, and the received signal strength is recorded. All these measurements are converted to the signal-to-noise ratio (SNR). Finally, the blockage loss is calculated and compared with the benchmark SNR.

- Blockage pattern: The propulsion system is located at different distances to the transmitter on the LOS. The motor speed varies according to different driving throttle levels. In this experiment, we test 5 throttle levels and try to identify the blockage pattern parameters, namely the blockage duration t_d and the rising time t_r. Again, the received signal is recorded at the oscilloscope and a maximum envelope detection is applied to the magnitude of received signal. Then a low pass filter would reduce the noise. The minimum threshold $a_{min} = 0.9A_{min} + 0.1A_{max}$ is defined as a combination of the maximum in the sample (A_{max}) and the minimum in the sample (A_{min}). The maximum threshold follows the same style, being set as $a_{max} = 0.1A_{min} + 0.9A_{max}$. This ratio will be adaptively adjusted given the noise on the final envelop. The rising time t_r is the duration between a_{max} and a_{min}. The blockage duration t_d is defined as the time duration between successive local minimums. Finally, the period t_p is defined as the time periodic of the blockage pattern. The definitions are illustrated in Fig. 5.4.

- Incident angle: Similar to previous experiment, the propeller is placed at the LOS path. However, the difference is that the frame is rotated gradually with predefined angles, then the incidence angles between mmWave propagation path and propeller blade is changed respectively. During this process, the propeller is given the second throttle level and placed with a distance of 1m from transmitter. The receiver is located 5m away from transmitter.

- Reflection: In this test, the intention is to exam if propeller could cause unwanted interference in a reflective path. During this test, the receiver is located on the same side with transmitter and propeller is in the working condition of distance 1.5m. Moreover, the signal strengths and the pattern are measured.

5.2.3 Experiment Result

All the blockage effects are showed, analyzed and summarized in this section.

Blockage Loss

As shown in Fig. 5.3, it is clear that the semi-optical mmWave communication is prone to the blockage incurred by the UAV propeller. The blockage effect of propeller could be a detrimental factor in the future mmWave communication.

In general, the blockage loss is less as the distance increases. Ranging from 10cm to 1m between the transmitter and obstacle, the blockage loss is about 4-10dB. For compact rotary UAV, it is a reasonable scale, which means that the existence of propeller could cause severe loss for the mmWave wireless module.

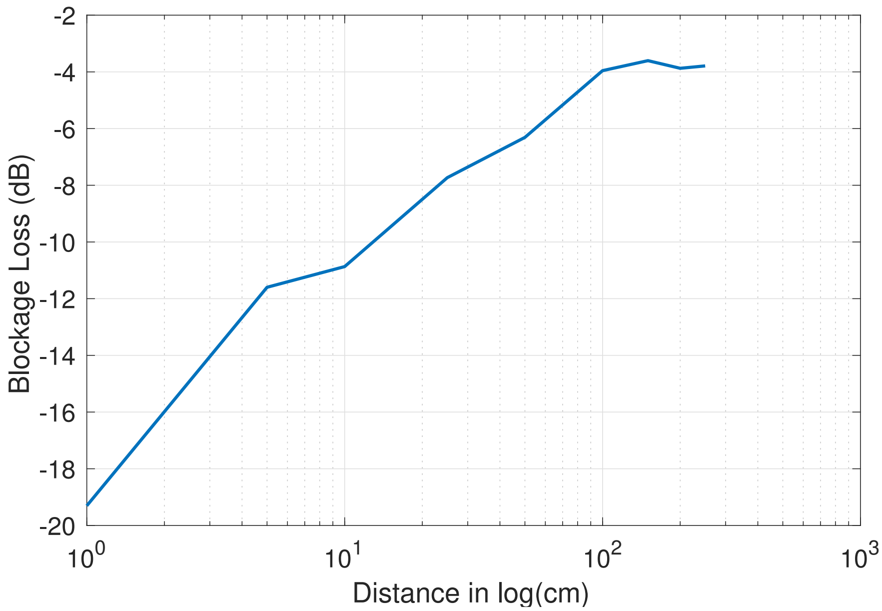

Figure 5.3: Blockage Loss due to the Rotating Propeller given Different Distances, where the x-axis is in the Logarithm Scale.

Blockage Pattern

Due to the high speed of the rotary motor in UAV, the blockage due to propeller creates a fast fading channel, in a sharp contrast to traditional slow shadow fading. It is obvious that the period of blockage is proportional to the motor speed as showed in Figure. 5.4. Especially with a lower speed, the ratio $\frac{t_d}{t_p}$ exactly matches the circular sector $\frac{17°}{180°}$. However, for settings with higher throttle, this equality no longer holds, mainly because the boundary is vague in the measurements with noise within such short time frame.

This blockage pattern proposes challenging problem for standard wireless structure. These fast and deep rising times may disable the automatic gain controller (AGC) in the RF chain; thus the transmitted data cannot be properly recovered through such a channel. As can be seen in Table 5.2 with high throttle levels (levels 3 and 4), the rising time is in the order sub-millisecond. Therefore, to accurately track the channel conditions with pure measurements, the pilots should be heavily interleaved within the time-space frame in such scenarios and wastes a large portion of bandwidth.

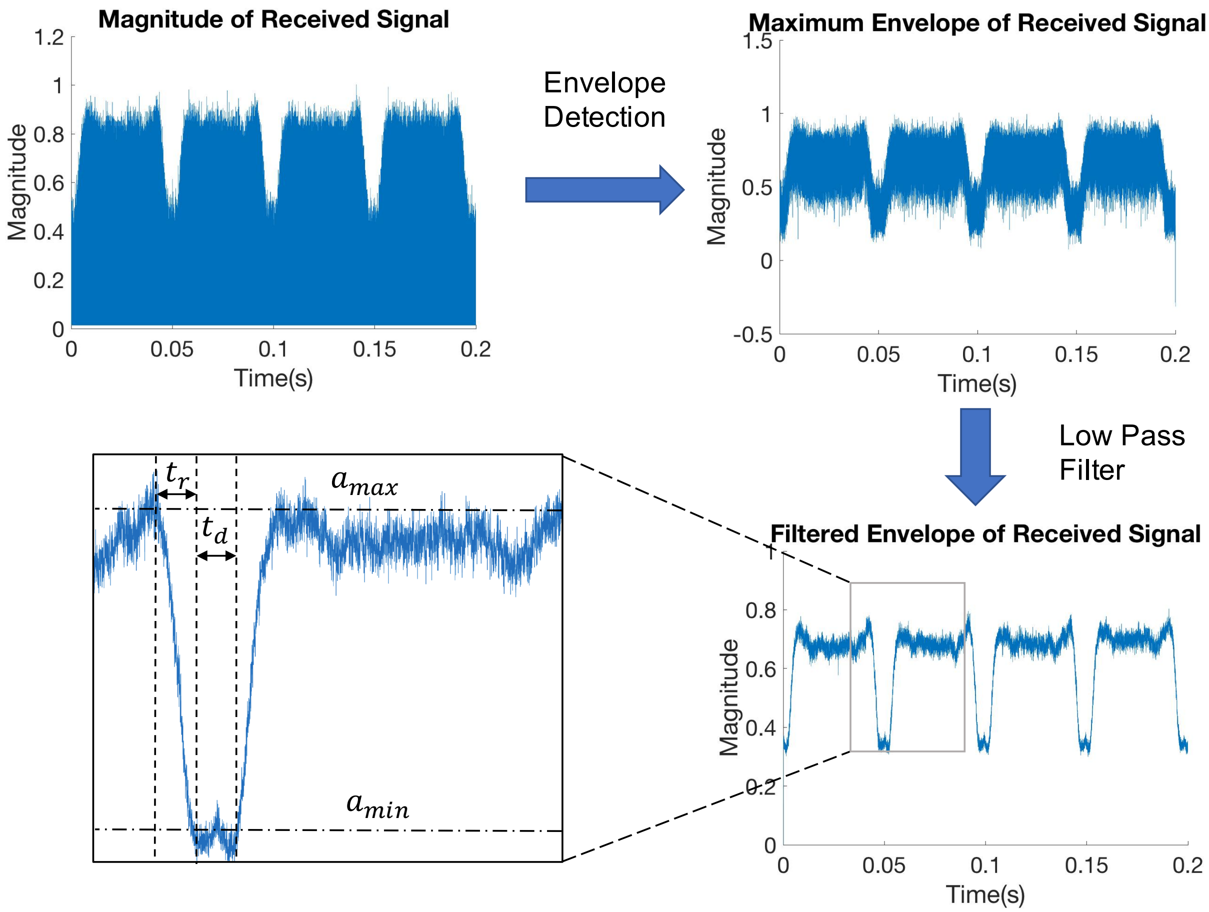

Figure 5.4: The Illustration of Blockage Pattern.

Table 5.2: Statistics of Blockage Pattern.

		Distance (cm)				
PWM	Time(ms)	50	100	150	200	250
1	t_d	5.2	7.5	11.6	14.1	14.7
	t_r	3.5	5.8	4.7	3.5	2.6
	t_p	49.7	49.6	50.0	49.9	49.4
2	t_d	2.9	3.2	3.3	4.2	4.7
	t_r	1.6	1.4	1.3	0.995	0.844
	t_p	14	14.1	14.1	14.1	14.1
3	t_d	1.6	1.9	1.7	2.3	2.9
	t_r	0.852	0.755	0.754	0.709	0.471
	t_p	8.2	8.2	8.2	8.2	8.2
4	t_d	1.1	1.0	1.2	1.8	1.9
	t_r	0.48	0.517	0.6341	0.493	0.405
	t_p	5.8	5.8	5.8	5.8	5.8

Incidence Angle

In this experiment, there are several interesting yet reasonable discoveries.

As the frame is rotating as in Fig.5.5 and 5.6, the square-like signal strength pattern gradually transform into a saw-like pattern. This transformation appears naturally given the comparison of two extreme cases — angle 0° and 90°. Angle 0 is the normal case as previous experiment. For angle 90°, the LOS path is along the surface of propeller, the variation of blockage area is the length of propeller blade flank. This could explain this phenomenon.

For angles with square-like SNR, the difference between the unblocked and blocked signal strength becomes less as showed in Fig.5.7. This results combines the decreasing LOS signal strength and increasing blockage signal. The first effect comes from the limitation of the experiment setup where the rotation of the propeller frame create more effective blockage area while the second effect results from the reduced effective blockage area from the propeller blade. One more observation from Fig.5.6 is that the average blockage time based on our experiment seems to be slightly increases over the incidence angle.

Reflection

From the Fig. 5.8, the receiver could indeed capture the reflected signal from several positions. However, during the experiment, the reflected signal is at least 19.2dB weak compared with LOS signal. This significant loss can be ignored in most of the cases, although, it still presents a potential threat for the unexpected interference for other directions.

Summary

In summary, this intermittent channel hinders the applications of mmWave in the UAV. For different modulations and coding schemes, it requires various minimum SNRs. If the channel is estimated under a good channel condition while the signal is transmitted later during a blockage, the real time SNR could fall below the minimum requirement. The bit error rate will change significant subsequently . This will be demonstrated in the following experiment.

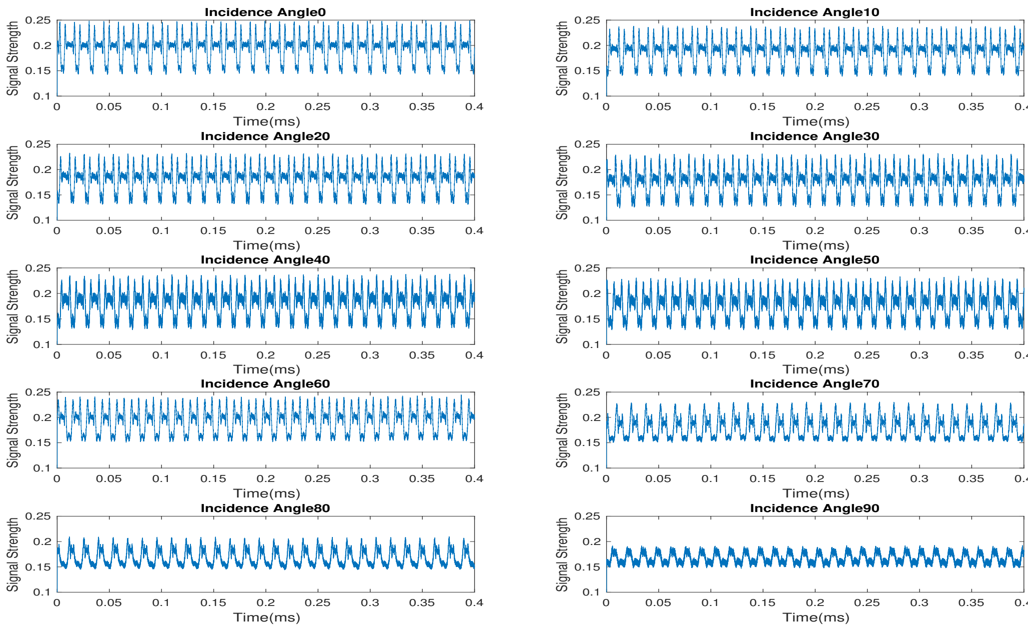

Figure 5.5: Blockage Pattern vs Incidence Angle. The Distance between Propeller and Transmitter is 1.0m.

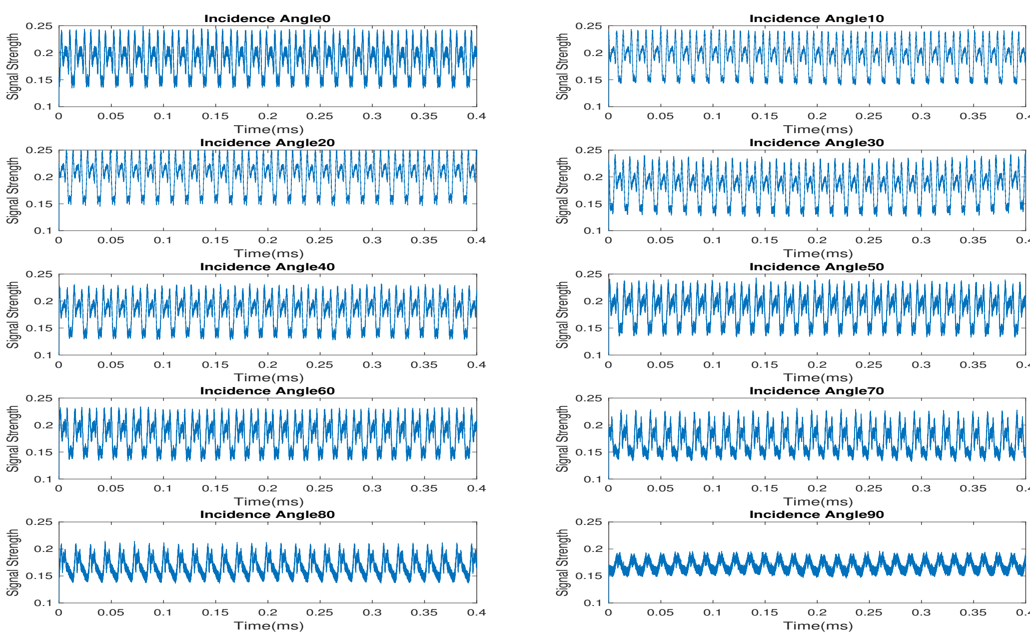

Figure 5.6: Blockage Pattern vs Incidence Angle. The Distance between Propeller and Transmitter is 1.5m.

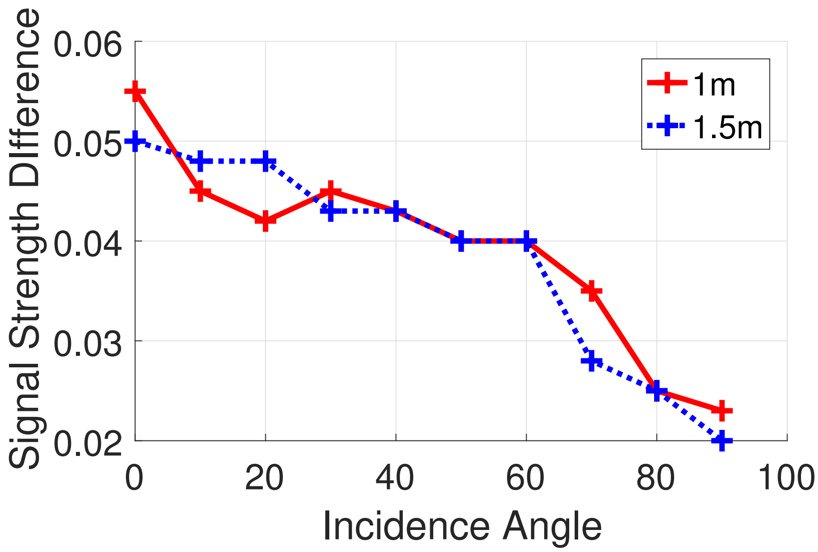

Figure 5.7: Signal Strength Difference between Blockage and LOS. (The legend shows the distance between propeller and transmitter.)

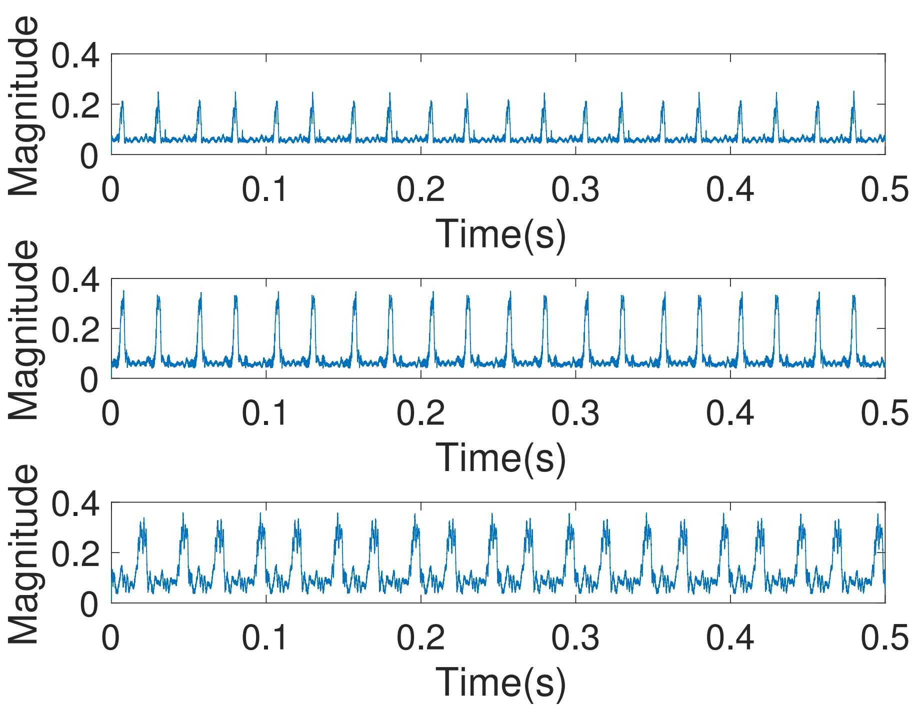

Figure 5.8: Reflected Signal Strength with Different Angles 60°, 45° and 30°.

5.2.4 Rapid Blockage with off-the-shelf Products

In order to demonstrate above detrimental factor, the second phase of experiment is with a commercial IEEE 802.11ad chip. A pair of Tensorcom TC60G-USB3.0 transceivers replaces the HMC evaluation board in the previous experiment. This transceiver is fully functional with basic PHY and MAC layer of IEEE 802.11ad standard. This standard is designed to replace wired cable for high throughput in a relatively static environment. Therefore, the frequency of channel estimation may not track the real time condition accurately.

The real time throughput is recorded using its own software with a log rate of 10 microseconds and two modulation and coding schemes (MCSs) are compared under different blockage distances and throttle levels. The throughput record is showed in Fig.5.9, where level 0 means that there is no blockage and can be considered as a benchmark result. Apparently, the throughput in MCS-4 is severely damaged by the working propeller. In spite

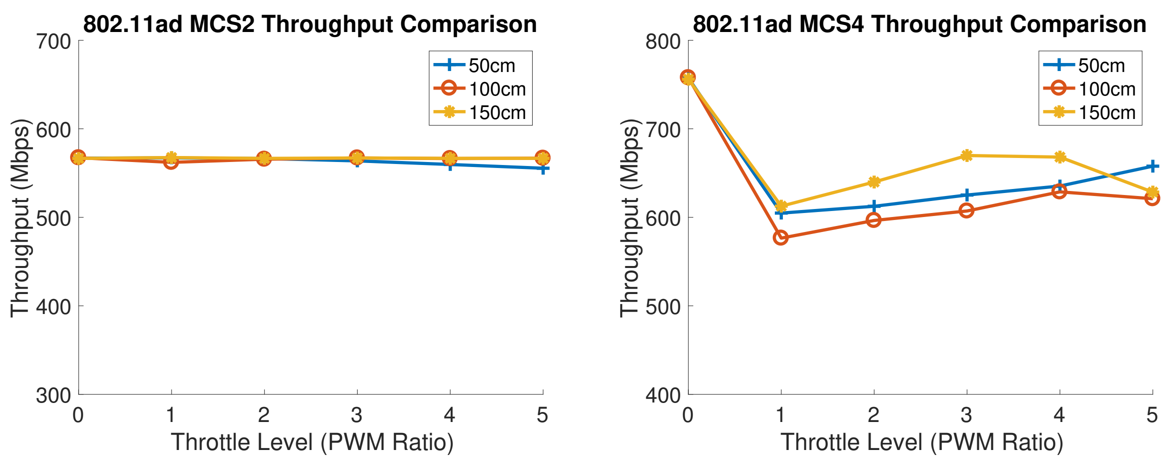

(a) Modulation and Coding Scheme: $\pi/2$-BPSK and 1/2 LDPC

(b) Modulation and Coding Scheme: $\pi/2$-BPSK and 3/4 LDPC

Figure 5.9: IEEE 802.11ad throughput test

of that, different throttle speeds of motor have relative even impact for on the throughput. Indeed, the average blockage time is almost a constant ratio, since the effective blocking area remains the same, regardless of the rotating speed. A higher throttle results in narrower dents with a higher frequency in the time domain while blocked/unblocked ratio remains the same. In contrast, MCS-2 almost holds the same performance compared with the benchmark. The comparison between above two figures reveals that MCS-2 still hold a safe SNR margin above the minimum SNR requirement while MCS-4 is right on the edge.

In a nutshell, given the off-the-shelf product in the mmWave spectrum, it cannot cope with such a hostile environment due to the blockage of UAV propeller, thus requiring a faster channel tracking.

The last thing but not the least, the material of propeller may not be restricted to carbon fiber. All proper materials can be used for propeller and the blockage loss could be different respectively. It's highly likely that the metal propeller could cause more blockage loss in such cases.

5.3 Blockage Pattern Detection—System Model and Quickest Detection

As the existence of blockage effect is confirmed, a robust communication for UAV mmWave system need to mitigate this negative effect. In general, there are two types of system design which could solve the problem — a highly integrated system design and modularized design. As for the integrated design, the mechanical system should inform the position of propeller to the communication system to boost the transmitting power. The second design strategy requires a robust communication module to survive the blockage. This chapter will focus on the second design scheme. Strategies based on sequential quickest change detection are proposed to detect the sharp edge of blockage and identify the pattern, and thus improve mmWave communication performance subject to UAV propeller blockage.

More specifically, the following three different approaches could help to ease the problem:

- Conservative MCS: The MCS is always conservatively determined given the real time SNR minus the blockage loss (in dB scale).
- Multiple Links: The UAV will explore the capability of multiple links with directional communication to multiple receivers.
- Blockage Timing Tracking: By monitoring and predicting the period of SNR ditches, we apply the adaptive modulation and coding to even the link quality of SNR.

Among these three, the third approach could achieve the best balance between throughput and reliability and the first strategy is considered as the benchmark for comparison.

5.3.1 Blockage Pattern Modeling

To accurately monitor the blockage pattern, the parameters of blockage ditches shall be distracted from the channel measurements since it is highly periodic in a relatively short time. For simplicity of system model, the assumption is that the blockage is perfectly periodic, which forms a periodic on-off process. Then the blockage pattern is characterized by the following parameters:

- Beginning time of blockage
- Time duration of blockage; i.e., t_d or $t_d + 2t_r$ in Fig. 5.4.
- The SNR drop; i.e., $\frac{a_{\max}}{a_{\min}}$ in in Fig. 5.4.

To estimate the above parameters for the blockage pattern, we need to detect the beginning and ending edges of each blockage period. This task can be accomplished by detecting the significant changes in the random process of received signal magnitude.

5.3.2 Heart-Beat Channel Model

Before the details of edge detection, the channel model combined with blockage pattern above is defined. In this model, the frequency band is evenly divided into N subcarriers (e.g., as in orthogonal frequency-division multiplexing, OFDM). Then, the received signal, as an N-vector, is given by

$$\mathbf{y}(t) = \mathbf{H}(t)\mathbf{x}(t) + \mathbf{w}(t), \tag{5.1}$$

where $\mathbf{y}(t) \in \mathbb{C}^n$ and $\mathbf{x}(t) \in \mathbb{C}^n$ are received and transmitted complex signals. The noise $\mathbf{w}(t)$ is assumed as white Gaussian noise with possible correlated distribution: $\mathbf{w}(t) \sim \mathcal{CN}(0, \Sigma)$, where Σ is the covariance matrix. Because LOS propagation is usually considered as the dominant path in mmWave, there is no multi-path effect and thus time dispersion in this model. Furthermore, all subcarriers are perfect isolated in the assumption with each other and no cross-interference exits, which is reasonable due to the large available bandwidth and sufficient guard bands. Hence, the channel matrix $\mathbf{H}$ is reduced as a diagonal matrix; namely $\mathbf{H}(t) = diag(H_t^1, ..., H_t^N)$. $\mathbf{H}(t)$ is time variant due to possible blockages and other time variant factors.

As previous experiment shows, the blockage effect is universal among mmWave spectrum. In other words, the diagonal elements of the channel matrix $\mathbf{H}$ will decrease simultaneously when the blockage happens despite other random factors. To accommodate the case in which different elements in $\mathbf{y}$ experience different blockages (e.g., if each element in $\mathbf{y}$ corresponds to a subcarrier), the simplified generic model for each diagonal element is given as $\mathbf{H}$ (in dB scale):

$$\mathbf{H}_t^n = L_B \mathbb{1}_{B^n}(t) + H^n(dB), \qquad n = 1, ..., N, \tag{5.2}$$

where L_B represents the blockage loss in certain scenario and $\mathbb{1}_{B^n}(t)$ is the indicator function of blockage existence, which could be different for different n's, and H^n is the channel gain when there is no blockage. As the blockage happens at time T_c, a subset of subcarriers experiences deep blockages, while some subcarriers may not. These properties are utilized for the blockage pattern recognition in the following contents.

5.3.3 Multi-channel Detection

Given the blockage channel model, the naive idea would be monitoring a subset of the subcarriers such that at least one of the subcarriers will experience the blockage with high probability, and then clarify a blockage.

However, this simple idea would not work well. First of all, one subcarrier could still experience the frequency selective fading over time, an edge detector of one subcarrier could be fooled by such noisy channel condition. The second concern is that the multi-subcarriers detection is equivalent to a multi-hypothesis detection problem where more subcarriers are monitored, it becomes increasingly likely that one test will raise false alarm with random process. In formally word, the FWER need to be firmly controlled, otherwise the probability of at least one incorrect rejection will boom with the increasing number of tests [46].

It is beneficial to find a method to cooperatively monitor the blockage event. This blockage detection now is considered as a multi time-series quickest detection for detecting the change of distribution in random process using multiple series of observations. The scheme for such multi-subcarriers quickest detection is illustrated in Fig. 5.10.

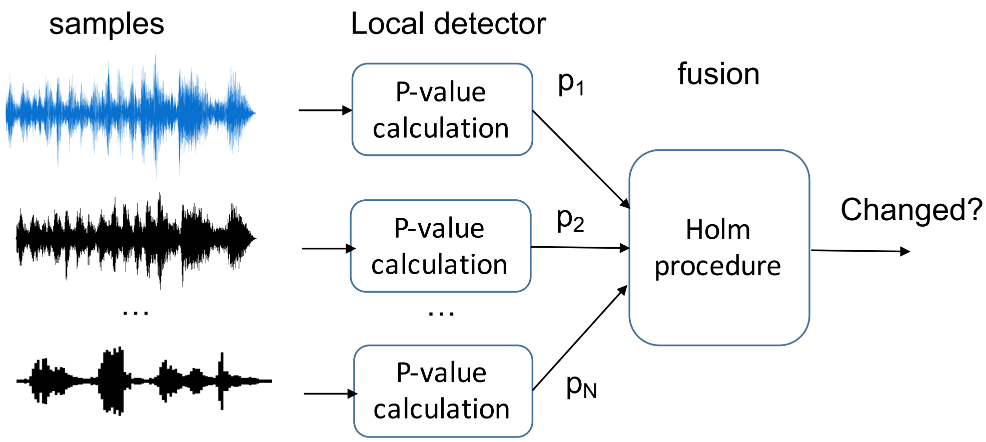

Figure 5.10: An illustration of multichannel quickest detection

Let the channel state H_t^n of subcarriers n be independent and identically distributed (i.i.d.) with probability density function $P(\cdot|\theta_0^n)$ up to the change time T_c and distribution $P(\cdot|\theta_1^n)$ after that. We further define F_0 and F_1 as the probability distribution respectively. Here θ_k^n, $k = 0, 1$, is the distribution parameter for H_t^n that could be used for the change detection if known(e.g., mean or variance). The change time T_c is not known in advance. When a change occurs, it will affect M out of the N subcarriers. That is, at time T_c, M channels will experience a distribution change, while the others remain unchanged. However, the subset of subcarriers experiencing blockage is an unknown parameter to the receiver. Furthermore, the value of M is not prior knowledge. Let T_k denote the time at which a change is declared (not to be confused with T_c, the time that a change actually occurs). Then to measure the detection performance, the metrics of detection delay is defined as the minimum worst case detection delay D_W with a constraint on the false alarm probability $P_{FA} \leq \alpha$.

$$\begin{aligned} &\min D_W(\tau) \\ &\text{subject to} \qquad P_{FA} \leq \alpha, \end{aligned} \tag{5.3}$$

where α is the constraint on the false alarm rate and

$$D_W(\tau) = \sup_{T_C \geq 1} essE[(\tau - T_C + 1^+)|\mathcal{F}_{T_C - 1}], \tag{5.4}$$

where $\mathcal{F}_t$ is the σ-field generated by $H_1, H_2, \cdots, H_t$.

In the next part, the detection problems on single subcarrier are firstly discussed and the multi-subcarriers edge detection algorithms are developed on those.

5.4 Multi-Carrier Change Detection and Adaptive Communications — A Holmes Approach

In this section, under different assumptions on the distribution, the problem of edge detection are treated respectively. Finally, the algorithm is deployed for an adaptive communication protocol without huge cost on channel estimation.

5.4.1 Problem of Edge Detection

The detection of a step change in the time series samples is a classical problem in the stochastic process. In general, the detection is related to the change in the all stochastic properties of certain stochastic process. As for the blockage detection, the simultaneous strength change among all subcarriers, which translates as the step change on the mean of the process, is the key for success detection. Based on the knowledge of distribution, we discuss this problem in two parts.

Detection with Distribution Known — CUSUM

If both F_0 and F_1 are known distributions with known parameters, the CUSUM test is proved to be the optimal solution to the minimax detection problem (5.4) Under the Lorden criterion [49], the stopping time of which minimizes the D_W given an upper bound of P_{FA}. It is easy to detect the change point with the log likelihood (LR) approach. The time to claim the change in the CUSUM test is given by

$$\tau^* = \inf \left\{ t \geq 1 : \max_{1 \leq k \leq t} \sum_{i=k}^{t} l(X_i) \geq \gamma \right\} \tag{5.5}$$

where γ is selected such that $E_0(\tau^*) = 1/\alpha$.

As for the detail of implementation, the CUSUM algorithm in [34] is applied at each subcarrier for each time slot. We define the instantaneous log-likelihood ratio for subcarrier n at time t as

$$s_t^n = \log \left(\frac{P(H_t^n|\theta_1^n)}{P(H_t^n|\theta_0^n)} \right). \tag{5.6}$$

θ_0 and θ_1 represent the null hypothesis and hypothesis that a change occurs respectively. In a recursive manner, the CUSUM metric of subcarrier n is computed as

$$S_t^n = \max(0, S_{t-1}^n + s_t^n). \tag{5.7}$$

If S_t^n surpass the threshold, it claims a detection of edge for a single subcarrier. Within such framework, the simultaneous change point is detected for the impacted subcarriers.

5.4.2 Multi-Subcarriers Detection

Previous section discussed the edge detection for single subcarrier and the CUSUM value can be computed or estimated in different scenarios. In this part, these detection algorithms are the cornerstone for a multi-subcarriers blockage detection algorithm.

The p-values of the detection for subcarrier n is desired to be a summary statistic that describes the important characteristics of the observed data. The CUSUM value is an excellent choice since its provides a compact representation of all data observed from time 0 to time t. Another desirable characteristic for this summary statistic is that its sample distribution under the null hypothesis can be analytically derived. Unfortunately, the CUSUM value derived from general distribution has no analytical form, even when the observations are standard normal. However, this distribution can be empirically estimated as follows.

Define $\mathcal{R}_\alpha^n$ as the rejection region containing channel n's CUSUM values, for which the null hypothesis θ_0 will be rejected when a significance level α is assumed, namely

$$\mathcal{R}_\alpha^n = \{S_t^n : \mathbb{P}(S > S_t^n|\theta_0) < \alpha\}, \tag{5.8}$$

where S is a random variable characterized by the distribution of the CUSUM statistic under the null hypothesis. Restrict the Type I family-wise error rate (FWER) to be

$$FWER_I = \mathbb{P}(S_t^n \in \mathcal{R}_\alpha^n|\theta_0) < \alpha. \tag{5.9}$$

From [93], at time t, the p-value corresponding to an observed CUSUM value at subcarrier n is given by $p_t^n = \inf(\alpha : S_t^n \in \mathcal{R}_\alpha^n)$ which follows $p_t^n = \mathbb{P}(S \geq S_t^n|\theta_0)$. Now if the cumulative distribution of S is known, then the p-value at time t and subcarrier n is simply given by

$$p_t^n = 1 - F(S_t^n) = 1 - \mathbb{P}(S < S_t^n|\theta_0). \tag{5.10}$$

In this case, the cumulative distribution function (CDF) of S is not explicitly known in both scenarios. However, an estimation of the CDF can be approximated by the Kaplan-Meier Method [43] for survival probability prior to testing. First sufficient samples are drawn from distribution f_0 to characterize the survival probability of pre-change distribution. Let $h(s)$ be the hazard rate for a given range of $s \in S$. For $s = 0$, the hazard rate is 0. Then the survival probability is given by

$$G(s) = F(s-1)(1 - h(s)). \tag{5.11}$$

The empirical CDF is simply the complement of the survival probability; i.e.,

$$F(s) = 1 - G(s). \tag{5.12}$$

Once the p-value is computed for each subcarrier, the receiver sends their p-values to the transmitter in a feedback channel. Then the transmitter uses the Holm's procedure [46] as follows to determine whether to declare a blockage if a criterion D is reached. The change detection is summarized in Procedure.1.

Initialization;
Compute the empirical CDF of the pre-change CUSUM values.
while *No Blockage Detected* **do**
  Each subcarrier calculates its CUSUM value using (5.6) and (5.7);
  Each subcarrier calculates its p-value using (5.10);
  Feeds back the p-value to the UAV;
  The UAV orders the p-values in an ascending order to obtain $p(1) \leq p(2) \leq ... \leq p(N)$;
  if $p_t^n \leq \frac{\alpha}{N-n+1}$ **then**
    Detection $d_n = 1$ for some n and we declare a detection if $\sum_n d_n > D$;
  else
    p-value is tested without detection;
  end
end

Algorithm 1: Holm procedure for multichannel quickest detection

5.4.3 Adaptive Communications

Once the parameters of the blockage have been identified, the mmWave transmitter can predict the blockage and then select corresponding MCSs. The key challenge is how to design the feedback from the receiver, without which the transmitter cannot sense the blockage.

The efficiency of adaptive design is highly dependent on the data frame structure. In this section, a prototype superframe structure similar to [105] is adopted. One superframe shown in Fig. 5.11 includes 100 slots, where each slot can be assigned as DL or UL. The ratios can be dynamically arranged based on the need. At the beginning of each superframe, a few slots will be used for beam association and training due to the limited searching ability in mmWave. Then the SNR of each slot with unique beam pattern will be recorded and compared in order to identify the optimal beam direction.

As in Fig. 5.11, there are two possible types of frame structures. The first arrangement are more focued on the real time feedback where downlink(DL) and uplink(UL) are heavily interleaved within one frame with in-time ACK for channel state feedback. This structure could satisfy the requirement of fast response and low latency requirement for mutual communication despite the large overhead could occurs. In the second frame structure, the feedback is located at the very last slot of each superframe for ACK or SNR report. In each slot, the control field is located at the beginning. One block of the control field contains a pilot for channel estimation. Each block will contain 10 symbols.

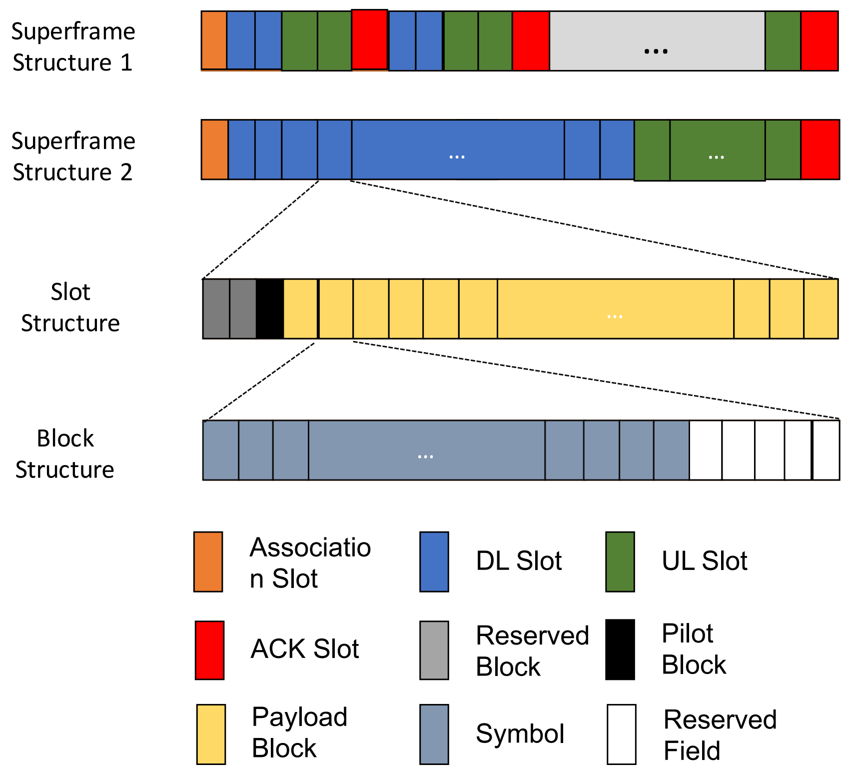

Figure 5.11: Illustration of superframe scheme

In the following simulation, a downlink transmission is considered where the UAV transmits data back to the ground base station. As shown in the experiment, the most impacted scenario is when there is no sufficient SNR margin for the blockage loss and herein two different strategies are compared within simulations, where the second based on intelligent prediction and learning is proposed as above.

- Real-time tracking: Use superframe structure 1 where an ACK slot is inserted for every 3 slots to feed back to the UAV the channel states in a relatively real-time fashion.

- Predicted tracking: Use superframe structure 2, assuming that the channel SNR record of this superframe is reported back to the UAV which will predict the next blockage.

Both feedback schemes will be tested in simulations.

5.5 Simulation Results

In this section, all simulation results are summarized on the quickest detection based blockage pattern identification and the corresponding throughput improvement.

5.5.1 Blockage Pattern Identification

The channel model in (5.2) is applied in the simulation where all channel gains are independent. Two criteria for the performance are compared under different setups, namely Σd_n the number of subcarriers needed for the quickest detection and the detection delay define as $\mathbb{E} = \max\{0, T_n - \tau_n\}$. The first metric corresponds to the computation cost and the second one represents the algorithm performance. In the simulation, a subset of 20 subcarriers are monitored, where the blockage pattern is simulated using the measurement signal strength pattern in the experiment. As various patterns are recorded in the experiment, the combination of distance 100cm and PWM level 2 is adopted for instance. The blockage begins at time $50ms$ and repeats after that. Each subcarrier will estimate its own channel state in the interval of $0.2ms$.

In Fig. 5.12 the detection over time with various number of monitored subcarriers is compared. Even with relatively less subcarriers (i.e, 3 out of 20), the detection performance is acceptable with a relaxed delay.

Fig. 5.13 demonstrates the detection over different blockage losses. It appears that a modest blockage loss is sufficient to identify the blockage. Indeed, if the blockage effect is minor, the AGC could compensate such an impairment of SNR and there is no need for the blockage compensation then.

Noise character is another important factor in the edge detection. Fig.5.14 thoroughly exam the impact on the detection result. Both detection delay and false alarm are severely impacted under large noise variance.

Finally, simulations are carried out given various rejection levels in Fig. 5.15. As can be seen, a tight α will lower the metric $\sum d_n$ as in Algorithm 1 while the false alarm rate is less in the first 50ms of all figures. Therefore, the threshold D can be appropriately selected between these two values.

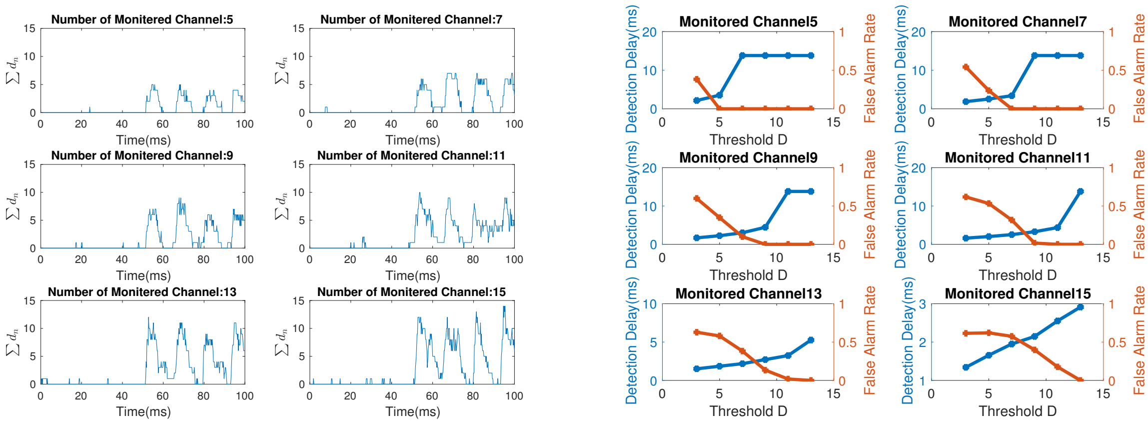

(a) Different Numbers of Subcarriers under 5dB Loss with Noise of $\mathcal{CN}(0, 5)$ and Rejection Level $\alpha = 0.1$.

(b) Detection Delay and False Alarm Rate under Different Channel Numbers and Thresholds D.

Figure 5.12: Simulation Results of Numbers of Different Blockage Channels

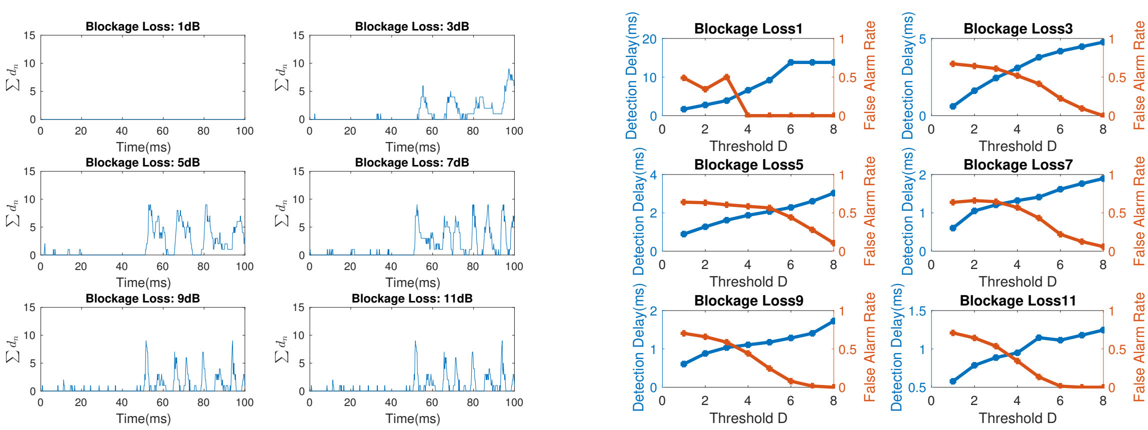

(a) 10 Subcarriers under Different Levels of Blockage Loss with Noise of $\mathcal{CN}(0, 5)$ and Rejection Level $\alpha = 0.1$.

(b) Detection Delay and False Alarm Rate under Different Levels of Blockage Loss and Thresholds D.

Figure 5.13: Simulation Results of Numbers of Different Levels of Blockage Loss

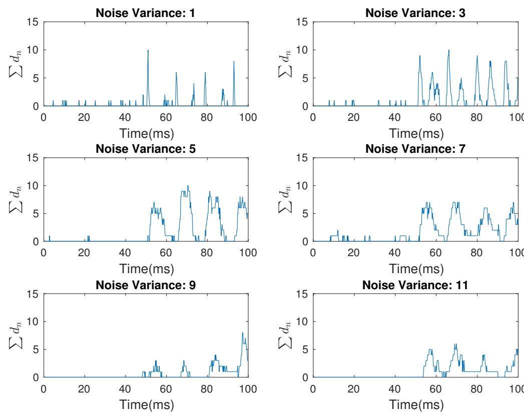

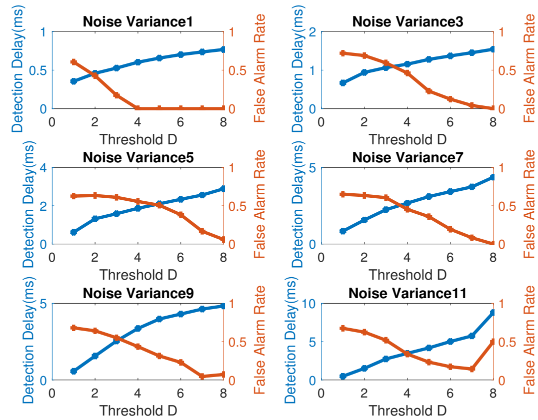

(a) 10 Subcarriers under 5dB Loss with Different Noise of $\mathcal{CN}(0, \sigma^2)$ and Rejection Levels α.

(b) Detection Delay and False Alarm Rate under Different Noise Variance and Thresholds D.

Figure 5.14: Simulation Results of Numbers of Different Noise $\mathcal{CN}(0, \sigma^2)$

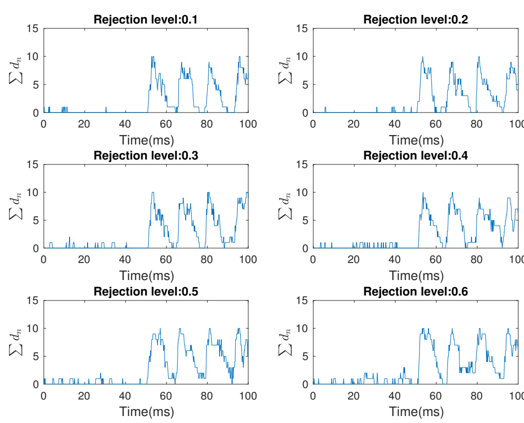

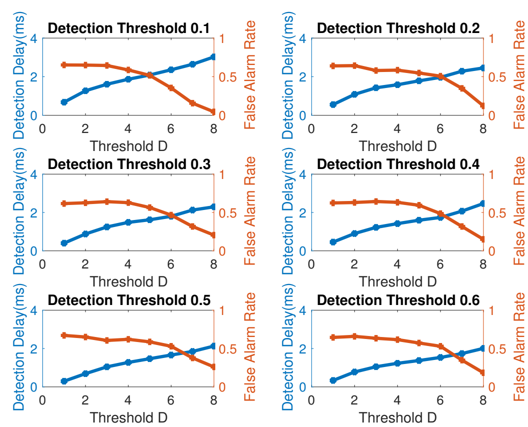

(a) 10 Subcarriers under 5dB Loss with Noise of $\mathcal{CN}(0, 5)$ and Different Rejection Levels α.

(b) Detection Delay and False Alarm Rate under Different Rejection Levels and Thresholds D.

Figure 5.15: Simulation Results of Numbers of Different Rejection Levels

5.5.2 Throughput Evaluation

The detailed parameters of the frame arrangement used in the simulation are listed in Table 5.3. To simplify the simulation, the time is discretized into time slots. It is assumed that the SNR does not change during one slot. A group of MCSs covering more than 15dB is predefined, whose BER rates are calculated in advance and are stored in a table. The predicted tracking proposed in this paper uses the previous ACK to predict the next blockage time and properly chooses the MCS. For the real-time feedback, an ACK is inserted in every 3 slots. For each slot, the throughput is simulated by accumulating the throughput combing the MCS and BER rate with the real-time SNR information.

Table 5.3: Parameters of OFDM data Frame

Carrier Frequency	60GHz
Sub Carrier	1MHz
Bandwidth	100 MHz
CP Time	0.25 μs
Symbol Length	1 μs
Block Time	10 μs
Slot Time	0.2 ms
Supeframe Time	20 ms

As shown in Fig. 5.16, three scenarios of blockage patterns are compared in Table 5.2—distance 150cm and PWM 2-4 for the blockage timing. The throughput is compared with the most conservative MCS strategy, namely always using the worst-case MCS. It is obvious that the conservative strategy wastes too much bandwidth for achieving a low error rate except for the extremely low blockage loss region, for which the feedback for detecting and estimating blockages takes a large amount of overhead to track the channel states. The proposed approach (slow feedback and prediction) performs similarly in this region. Otherwise, the approach could outperform the other two methods (namely the conservative one and the real-time feedback).

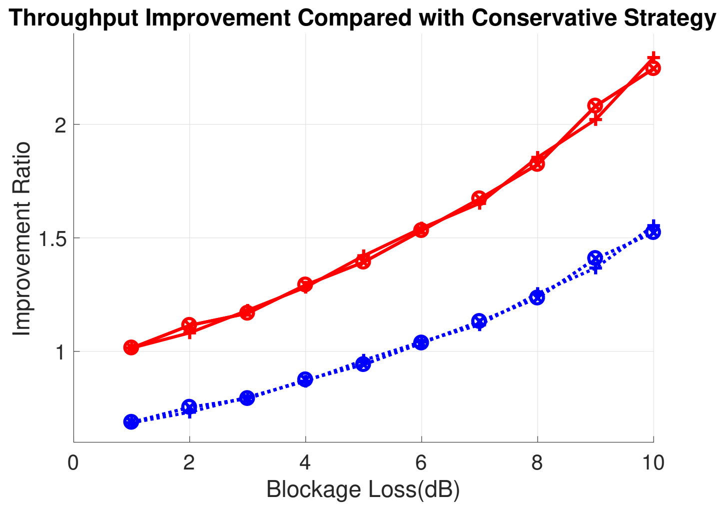

Figure 5.16: Throughput improvement

5.6 Conclusion

The integration of mmWave communications and UAV is both promising and challenging in the near future. At the beginning of this chapter, several experiments of mmWave communications on a UAV testbed confirmed the concern of blockage incurred by UAV propeller. The limited volume of the UAV might be a detrimental factor for the mmWave communications, where the blockage effect could be severe. Moreover, the blockage patterns are recorded and analyzed. The fast but periodic fading wireless communication channel may demand a fast channel estimation to mitigate the performance impairment. Then a quickest detection scheme is proposed by using muiltiple subcarriers to detect blockage and identify its pattern. Simulation results have demonstrated that the proposed method could successfully identify the blockage in an agile manner, and the data throughput is improved when compared with benchmark results.

Chapter 6

Handover Prediction based on Geometry Method in mmWave Communications

6.1 Introduction

Due to high propagation loss, mmWave cellular communication is typically implemented in small and densified cells with a radius of no more than a couple hundred meters. As the shrinkage of cell size, frequent handover between cells and the resultant high overhead is an intrinsic problem faced by densified mmWave cellular networks. Unlike handover in 3G/4G networks, a handover in mmWave networks is more resource and time-consuming, as the initial access of the new beam requires expensive signaling and long training time (e.g., could be as long as a couple seconds) [9]. The issue is further exacerbated by the fact that a mmWave channel is vulnerable to the blockage of obstacles. The short wavelength of mmWave makes it difficult for the signal to penetrate through or circumvent around the obstacle. Thus, a LOS blockage of the mmWave channel could easily translate into a 20 to 30 dB loss on the signal strength, leading to a sudden outage of the received signal [14], and hence calls for a handover.

LOS blockage happens frequently in a mobile scenario, because a user's movement could easily encounter obstacles such as treetops, pedestrians, and buildings, as illustrated in Fig. 6.1. The blockage by these obstacles renders a mmWave link handover more frequently. For example, according to the study of Nokia Research [92], the typical average interval between two adjacent handovers in a mmWave cellular network is only around 15 seconds, while for certain types of user scenarios the average interval can be as short as 0.75 seconds. The frequent handover and the resultant expensive overhead in signaling and beam training has been the main challenge for seamless mobility in mmWave cellular systems.

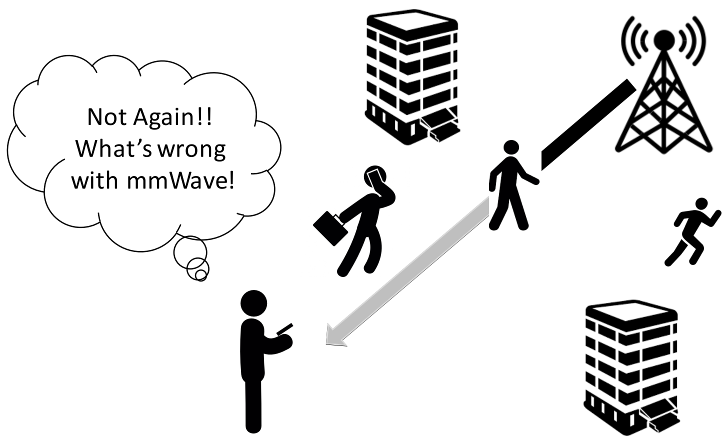

Figure 6.1: Human Movement Blockage

To address the above challenge, in this chapter a LOS-blockage/outage prediction mechanism is proposed for small and densified mmWave cellular networks to eliminate unnecessary handover and make necessary active handover smoother/more seamless. The prediction is based on the real-time sensing of blockage of peripheral NLOS components. These NLOS components may not be strong enough to be used for high-speed communication but are typically strong enough to be detectable. Combined with the geometry of the mmWave multipaths channel, the proposed mechanism can accurately predict when the LOS path will be blocked, as well as how long the blockage will last. All the benefits are explained in detail.

- Reduce mmWave handover frequency: Given the knowledge or prediction of the dimension of the blockage items, the mobile device can avoid unnecessary handovers related to short-time-scale blockage/outage (e.g., those caused by a pedestrian or a car).

- Enable advanced active handover: Obtain lead time before necessary active handovers (e.g., those caused by long-time blockages such as a building) and therefore enable handshaking with the handover destination base station in advance, so that the handover can be made with significantly reduced delays compared with passive handover that only initialize the procedure when it suffers great signal strength loss.

This method is deterministic in nature, and is thus in sharp contrast to existing statistical prediction models such as the finite state Markov chain [27, 33], MDP [57], and POMDP [94, 95], which predict the possibility of an outage in the next time slot based on the current channel state. The probabilistic nature of these methods inevitably renders large errors to the prediction (false positive and false negative). Compared with existing statistical models, this sensing-based model does not rely on assumptions of the channel statistics/distributions, and thus can eliminate prediction errors caused by the channel uncertainty. The feasibility and effectiveness of the proposed mechanism are validated based on experiments in a real mmWave communication testbed.

The remainder of this chapter is organized as follows. The system model and the problem statement are described in Section 6.2. Then the proposed blockage prediction mechanism is presented in Section 6.3. Section 6.4 provides the experiment setup and results. Conclusions are drawn in Section 6.5.

6.2 Channel Model and Problem Statement

In this section, the system model is introduced and blockage prediction in such system are defined.

6.2.1 Channel Model

We consider a quasi-static outdoor environment where obstacles are either static or moving and receiver is moving slowly (pedestrian speed). Field measurements have revealed that an outdoor mmWave channel in mostly time has a sparse spatial structure. In particular, the signal propagation path between a transmitter and a receiver consists of a dominant LOS component and a few, say $L-1$, weak NLOS components, as shown in Fig. 6.1. The path loss of a component i ($1 \leq i \leq L$) can be characterized by 4 parameters, a_i, ϕ_i, δ_i, and θ_i, which represent the component's amplitude, phase shift, the angle of departure (AoD) at the transmitter, and the angle of arrival (AoA) at the receiver, respectively. Without loss of generality, we consider a case where the directional antennas such as phased-array antennas are used at both the transmitter and receiver for beamforming. A phased array antenna creates directional beam(s) to transmit and receive signals. Since the proposed channel sensing is carried out by the receiver, this chapter is focused on the receiver's perspective on the signal presentation. More specifically, the received signal is the combination of L different components (with AoA θ_i), each of which travels through a different propagation path and is amplified by the transmitter antenna gain G_t and receiver antenna gain G_r along that path component, i.e.,

$$r(t) = \sum_{i=0}^{L-1} a_{\theta i} s(t + \phi_i). \tag{6.1}$$

Note that to simplify the notation, $a_{\theta i}$ in above equation represents the combined effect of both propagation path loss and the (transmit and receive) antenna gains. Since a phased-array antenna may present different beam patterns, a_{θ_i}'s are variables dependent on antenna patterns of two ends. $s(t + \phi_i)$ represents the transmitting signal with phase shift by ϕ_i.

6.2.2 The Blockage Prediction Problem Formulation

The Blockage Prediction intends to predict when the LOS path will be blocked by obstacles, and how long the blockage will last. To illustrate the idea, a toy micro-mobility example is considered in Fig. 6.2a, where the receiver r is static but the obstacle O is moving at a constant speed v along fixed direction α. The assumption of moving along a fixed direction at a constant speed is largely true for a small-scale movement at the outdoor. To simplify the analysis, we further assume that the obstacle is much closer to the receiver than to the base station, which is a typical scenario in outdoor cellular applications. If the obstacle is far away from the mobile receiver, it becomes either a slow-fading channel factors or a small blockage loss due to the distance.

Let t_i denote the moment when the trajectory of O intersects (and thus blocks) the i-th path, where $1 \leq i \leq L$. This model should predict t_i before these blockages occur and meanwhile determine which t_i corresponds to the LOS path. Note that none of the geometric parameters in Fig. 6.2a, including α and the amplitude/AoA of any path component, is given as a priori information. Moreover, for the baseline problem v is unknown and no location information is available.

Under the assumption above, the slow and slight change of the path components, which caused by the small-scale movement of the receiver, can be safely ignored based on the geometry. Therefore, this path-traversing model in Fig. 6.2b can well approximate the process above, where the receiver r is moving at a constant speed v along a fixed direction $\pi + \alpha$. With the movement of r, a static obstacle, represented by a node O, will eventually 'cut through' all L paths of the mmWave channel of receiver r, and thus block them, one at a time. The approximation of the process in Fig. 6.2b by the linear trajectory model in Fig. 6.2a provides a lower bound for the blockage time prediction.

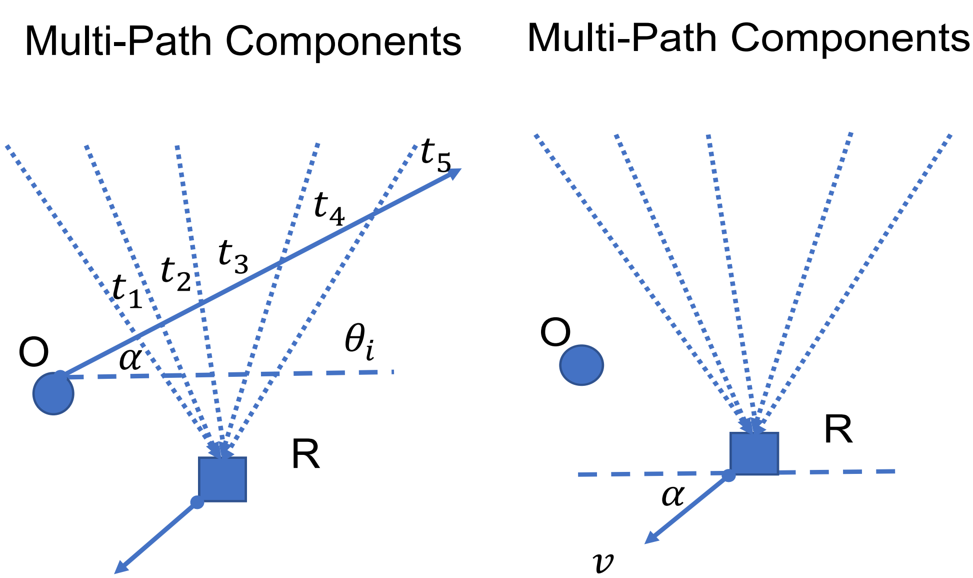

(a) Blockage due to Moving Obstacle and Static Receiver

(b) Blockage due to Static Obstacle and Moving Receiver

Figure 6.2: Two Approximately Equivalent Blockage Models

Clearly, it is unrealistic to predict $(t_1 \dots t_L)$ before O hits any of these paths. Therefore, a more realistic version of the problem is given: for some small i, is it possible to predict $(t_{i+1} \dots t_L)$ when $t_1 \dots t_i$ have happened? In other words, we wish to predict the moment of LOS or main communication link blockage based on the moments when some peripheral NLOS paths are blocked. As will be shown later, the peripheral NLOS paths is clearly detectable within the range, yet they are considerably weaker than the preferred link. Such a prediction is usually sufficient for just-in-time handover, because: (1) the blockage of NLOS paths has little influence on the existing connection, and (2) slow movement (small v) is the case for the micro mobility scenario under consideration; hence prediction based on peripheral NLOS blockage still gives significant lead time to LOS blockage.

Note that the second problem of predicting the blockage duration can be converted into the prediction of difference between two moments, when the two ends of the obstacle 'hit' the LOS respectively. In other word, the moments of entrance and exit are applied for the duration prediction. Therefore, it is sufficient to only discuss the first problem.

6.3 Geometry-based Blockage Prediction

In this section, the blockage prediction algorithm is described in two phases. In the high level overview, the solution first identifies the path geometry of the mmWave channel and the trajectory of receiver R (or equivalently O). Then the algorithm is proposed to predict the blockage timing $(t_3, \dots, t_L)$ based on the detection of t_1 and t_2.

6.3.1 Resolving Moving Direction α

The receiver's moving direction α can be calculated by exploiting the beam tracking feature of the phased array antenna, by which the transmitter (and/or receiver) continuously steers its beam to follow the LOS while the receiver moves, such that the AoD (or AoA) of the LOS is known by the transmitter (receiver). To illustrate the calculation procedure, consider the example in Fig. 6.3, where we assume that the transmitter (i.e., the base station) is at the origin, and the receiver moves at speed v along the direction α. Without loss of generality, suppose that the AOD of LOS is 0 at time $\tau_0 = 0$. Accordingly, let us assume that the receiver is at coordinate $(x_0, y_0) = (0, 1)$ at time τ_0. Note that the assumption $y_0 = 1$ is arbitrary and it does not affect the calculation of α. The assumed coordinates are only used to facilitate the calculation of α, and do not reflect the actual location of the transmitter and receiver.

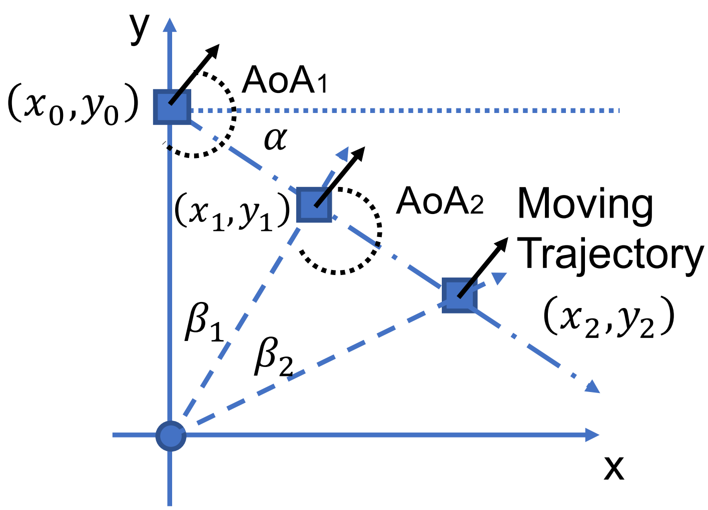

Figure 6.3: Estimation of Moving Direction α Based on AoA β_i

The receiver will monitor the AoA of the main path in a fixed interval δt. Based on trigonometry, it is easy to see that the angle increment of AoA as $\beta_i = AoA_{i+1} - AoA_i$ where i is the sample time. Then β_1 and β_2 are known at given timestamps τ_1 and τ_2. The 1th and 2th coordinates of receiver should be $(x_1, y_1) = (z \cos \alpha, 1 - z \sin \alpha)$ and $(x_2, y_2) = (2z \cos \alpha, 1 - 2z \sin \alpha)$ respectively, where $z = v\Delta t$. Then α can be obtained by solving a bi-variant quadratic equation set by cosine formulas:

$$\begin{cases} (\omega^2 - \cos^2 \beta^1) z^2 - 2z\omega \sin^2 \beta^1 + \sin^2 \beta^1 = 0 \\ (\omega^2 - \cos^2 \beta^2) z^2 - 4z\omega \sin^2 \beta^2 + \sin^2 \beta^2 = 0 \end{cases} \tag{6.2}$$

where $\beta^1 = \beta_1$, $\beta^2 = \beta_1 + \beta_2$ and $\sin \alpha = \omega$. The two unknown variables to solve above are ω and z. This equation set can be solved and the reasonable solution is taken to resolve the moving direction α.

6.3.2 Predicting the Moment of LOS Blockage

For a quasi-static mmWave channel, a_i, θ_i, and ϕ_i vary slowly, and therefore they can be resolved by mmWave channel sensing (see Section 6.4). t_1 and t_2 can also be detected by sensing the change of amplitudes of the channel components (i.e., a_i). After all the geometric parameters at time t_1 and t_2 have been obtained, the prediction of $t_3 \dots t_L$ is made by calculating the ratio of the distance traveled by the obstacle between adjacent path components (see Fig. 6.2a). Specifically, suppose that l_i is the distance that the obstacle travels between the i-th and the $i+1$-th path components. Then the next few hitting times can be predicted as

$$t_3 = t_2 + \frac{l_2}{l_1}(t_2 - t_1) \tag{6.3}$$

$$t_4 = t_2 + \frac{l_2 + l_3}{l_1}(t_2 - t_1)... \tag{6.4}$$

Because the ratio between paths is the only key for a successful prediction, an arbitrary line of angle α can be assumed, and then compute its intersection with each of the path component. In particular, for the intersection with the i-th path component, we have

$$y = (\tan\theta_i)x \tag{6.5}$$

$$y = (\tan\alpha)(x - x_1) + y_1 \tag{6.6}$$

where (x_1, y_1) is arbitrarily assumed, but fixed for all path components once it is assumed. Because this line is parallel with the actual trajectory of the obstacle, the set of calculated intersections is merely a scaled version of the intersections between the actual obstacle trajectory and path, thus preserving the same ratio. The predicted moment of LOS blockage is given by $t_i^o = (t_i | i = \arg\max_{1 \le i \le L} a_i)$.

6.4 Experiment on Blockage Prediction — A Semi-Real Time Result

In this section, several experiments are done to support the assumption we made for the modeling and validate our proposed prediction algorithm.

6.4.1 Experiment Setup and Measurements

During the experiments, we have tested two versions of platforms which basically switch the baseband processing unit for the performance differences; yet the result shows the difference is negligible for sensing purpose.

In general, the two testbeds share similar structures. Two general software defined radios — WARP V3 and USRP NI2922 are adopted for real-time data acquisition of raw data within the two testbeds, respectively. For the WARP platform, an additional AD9963 AD/DA extension board with clock board is connected through the HMC interface to bypass the onboard AD/DA. The other components are well described in chapter II. The detailed scheme is demonstrated in Figures 6.4 and 2.1. The azimuth resolution is chosen as of 1.8 degree. One additional critical component on the NI-based platform is a 400mm linear stage actuator

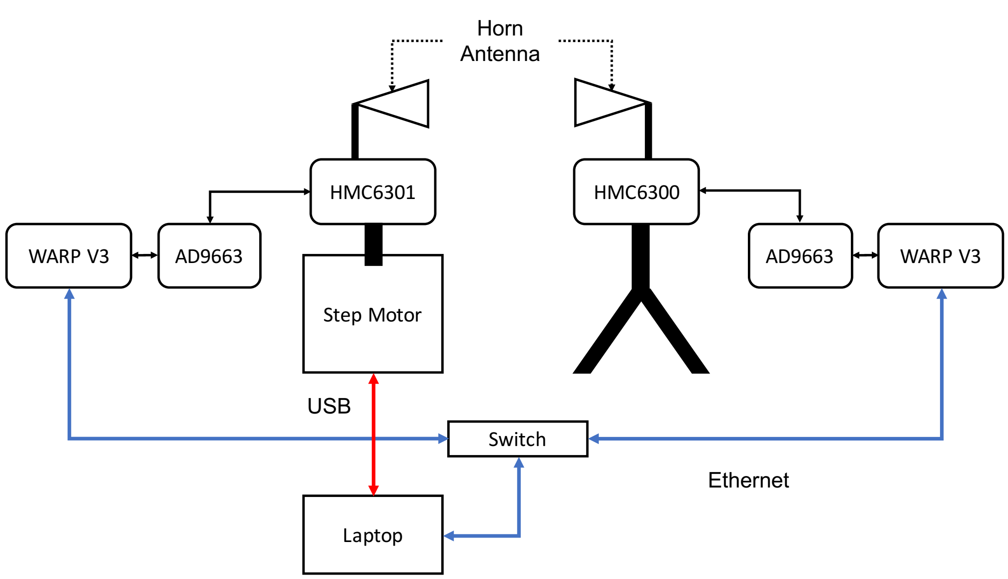

Figure 6.4: Scheme of Motorized mmWave Communication Testbed

shown in Figure.2.1, which allows us to accurately control the movement in the experiment of resolving α.

During all the experiments, heights of both ends are adjusted to be the same level to minimize the misalignment. Although the proposed algorithm is for outdoor scenarios, all experiments in this paper are conducted in an indoor environment, due to the limited RF power of our platforms.

6.4.2 Estimation on Movement Direction α

For the direction detection, the channel measurement is carried out in a semi-static environment, since the environmental channel scanner cannot cover the azimuth space in real time. The linear stage actuator would mimic the movement of receiver, where the distance is accurately controlled by the laptop.

The resulting heat map is given at Fig. 6.5. During this experiment, the transmitter is fixed to send a predefined signal a certain direction. The receiver moved along a straight line following one direction, thus crossing transmitting beams. The total accumulated movement

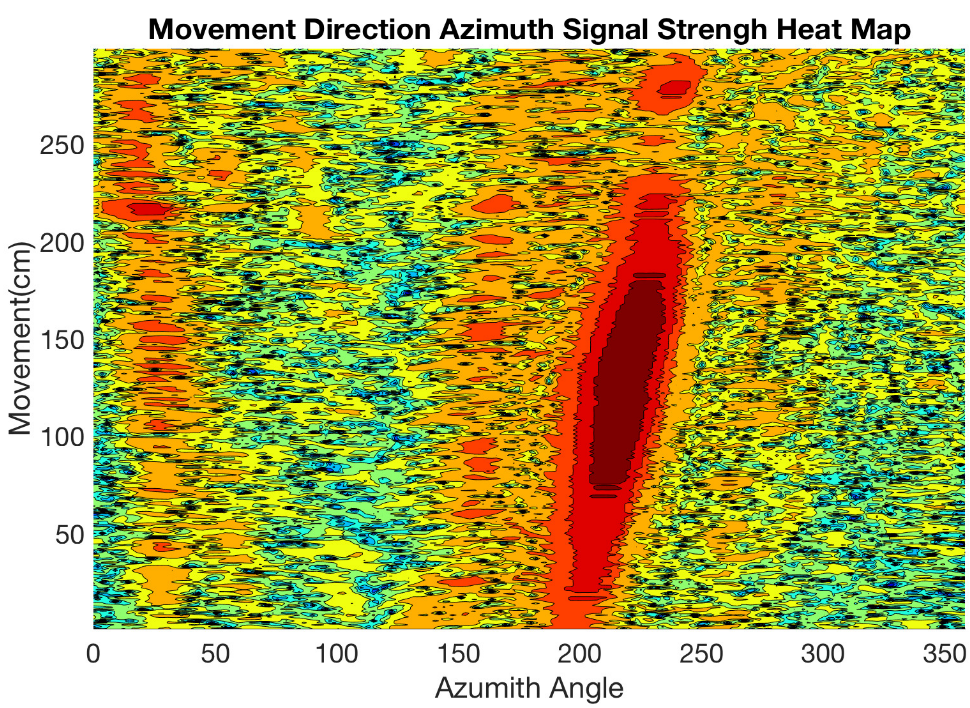

Figure 6.5: Signal Strength over Azimuth Angle and Movement

of receiver is $3m$ with the step size of $1cm$. When the linear actuator stabilized, the testbed will scan through the azimuth plane to capture and measure the signal strength. We choose the SNR as the signal strength indicator. In other words, the transmitter generates a predefined baseband signal and upconverts to the carrier frequency of 60GHz. When the receiver is stabilized, it will capture the RF signal and then record the received baseband signal. This received signal is used for offline SNR calculation.

This result clearly demonstrates that the strongest signal angle, which is the AoA of LOS angle, will drift to follow the movement. One thing to notice is that the beam width of antenna is more than 5 times wider than the azimuth step size. Therefore, the spatial resolution will be improved, if a narrower horn antenna is adopted.

However, although two horn antennas are not strictly aligned at some locations, this healmap can still be used to identify the AoA and movement direction. Given the widths and angle information of the strong area in Figure 6.5, we could calculate the medium angle as the estimation of AoA. The moving direction of the receiver can then be calculated using (6.2).

6.4.3 Blockage Prediction

The blockage prediction is done in a lab that has a floor size of 9.5m by 6m, as showed in Fig. 6.6. The walls are made of bricks and surrounded by tables and one white-board.

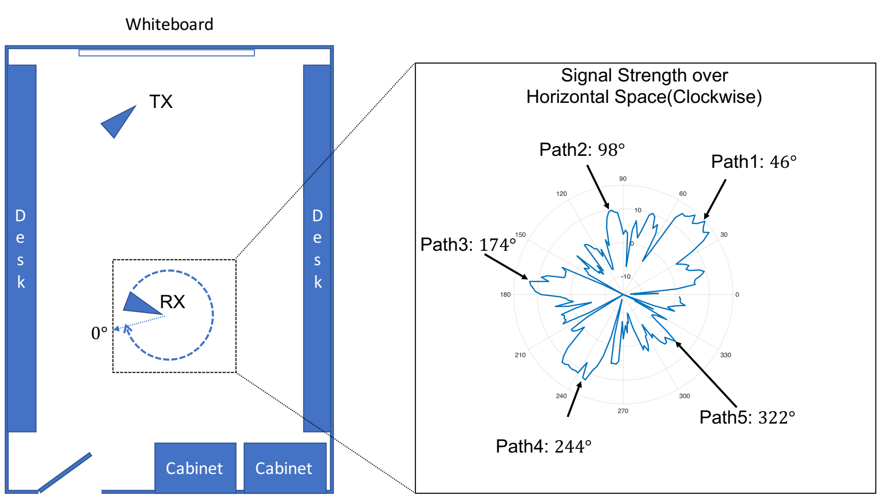

Figure 6.6: Floor Plan of the Lab and the Polar Plot of Multi-paths Signal Strength

By one side of the wall, one door and two metal cabinets are aligned. In general, the lab is a typical and relatively closed indoor space. The transmitter and receiver are placed about 3 meters away from each other, while the antennas are not aligned, thus preventing the LOS path. The reason for this NLOS setting is to approximate the multi-paths channel condition in the outdoor open space.

This part of experiment is accomplished by two phases. First, we identify the AoA of multi-paths. This experiment follows the same procedure of resolving moving direction but without the linear actuator. Again, the signal is recorded and the SNR is calculated around the azimuth plane. Finally, the local peaks in the signal strength are identified among the horizontal space. These are considered as available paths for data transmission or sensing as showed in Fig. 6.7.

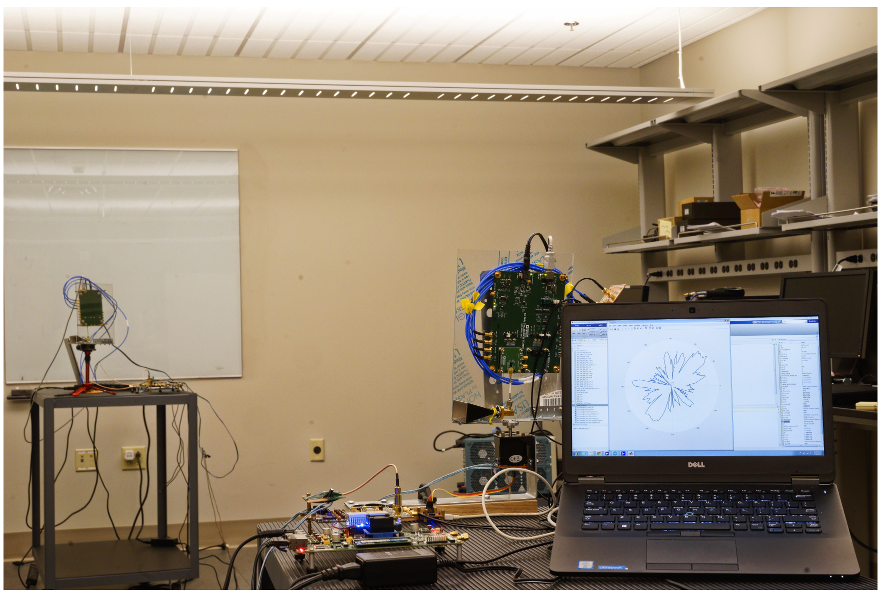

Figure 6.7: Setup of Field Test

Once the AoAs of multi-paths are identified, the second phase is to use the information of times of NLOS paths blcokage to predict the blockage time of the main communication path. Due to the limitation of channel measurement and angle resolution of testbed, the experiment is conducted in a semi real-time approach. It is assumed that the blockage objective is moving with a constant speed and the test for the blockages of NLOS path is done in a static approach. Specifically, One human obstacles is standing still in a potential blockage place, and the receiver will scan through the azimuth. If a significant SNR drop on

a_{θ_i} appears in the corresponding NLOS path, then it can claim that this is one cut-through point between the obstacle and that NLOS path component. Later, these positions are recorded for the blockage prediction based on our algorithm.

6.4.4 Experiment Result

Phase 1 — Resolving α

As it is discussed in the previous section, the AoA can be calculated even with horn antenna with a large beam width. However, as shown in the Fig. 6.8, the sampled AoA has relatively large noise while the algorithm requires more accurate estimation for real time detection, due to the fact that a small time-interval δt will lead to small angle increment. This can be overcome by extending the time interval or using a narrower beam width for high spatial resolution. Nevertheless, here we use linear regression to smooth the measured AoA. The result is $AoA(t) = \frac{1}{6}t + 198.1$. $0.4s$ is taken as the time interval. The result is reasonably accurate: the estimated $\alpha = 6.4°$ while the ground truth is $5.36°$. The estimated error is around $1°$.

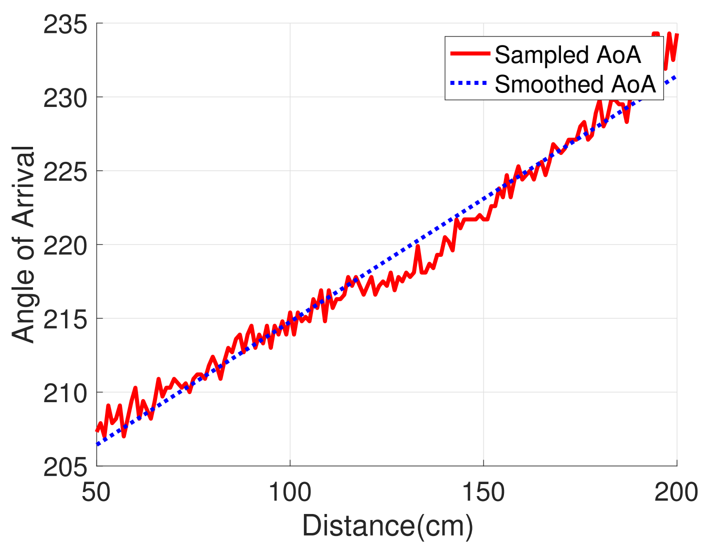

Figure 6.8: Comparison of Sampled AoA and Smoothed AoA with Linear Regression

Phase 2 — Multi-Path Identification

The experiment done in Fig. 6.6 has substantial multiple paths in the azimuth space. As can be seen, the dominated path components is the signal from the first reflection. The polar plot shows that multiple azimuth angles have relatively strong strength with different widths, and all these can be considered as viable path components in Fig. 6.9. In this experiment, paths at 46°, 98° and 174° are chosen for the blockage prediction.

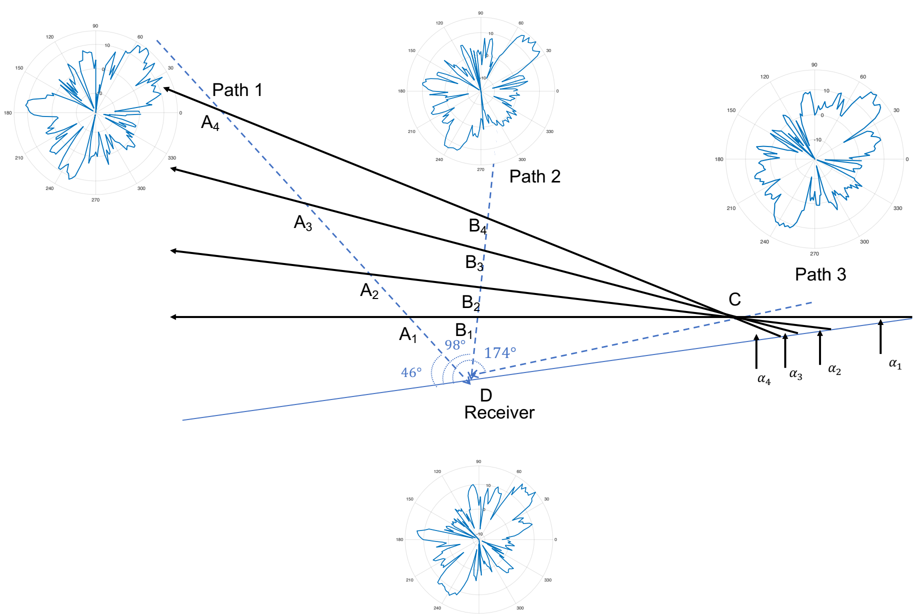

Figure 6.9: Blockage Prediction Scheme with Experiment Records

Before proceeding to the second phase, one key assumption needs to be confirmed in the experiment, namely the reproductivity of the experiment result in a static environment. Unlike the standard RF testing room with absorption materials attached on the wall, the lab room is filled with reflective and scatter objects, and these random factors could cause the variation in the signal strength. We scanned the horizontal space for multiple times in the same spot and calculated the variation of among angles. The result confirms that a static environment could create steady polar SNR plots.

Phase 3 — Blockage Prediction

As stated in the previous section, three paths are used to verify the prediction algorithm. A SNR drop of 5dB is considered as an indicator of a blockage event. More specifically, the signal strength is monitored where blockage occurs at angle 98° and 174° and positions are recorded to predict the time of blockage of 46°. As can be observed from Fig.6.10, these three angles are intersected by straight lines CA_i. More complicated cases can be easily extended as we have shown above.

With a limited lab space, only four possible crossing angles α_i are measured with different crossing points as shown in Figure6.9. The location of receiver is assigned as the point D. α_i is determined by the measurement of DB_i, DC and CB_i in trigonometry. Therefore, the location of $\hat{A}_i$ can be further determined. Finally, a human obstacle stood around the pre-calculated A_i and found the true blockage point where the most blockage loss is observed.

Fig. 6.9 demonstrates a set of measured channel data (AoAs and amplitudes of the paths) in one of the blockage tests, where the testbed tracks the blockage of NLOS at different AoAs 174°, 98° and 46° by detecting the degradation of their amplitudes. As shown in these figures, the strength of a path is attenuated significantly when it is blocked, comparing with the benchmark of no blockage. This effect is clearly demonstrated at the lower part of Fig. 6.10, while other paths remain almost unchanged.

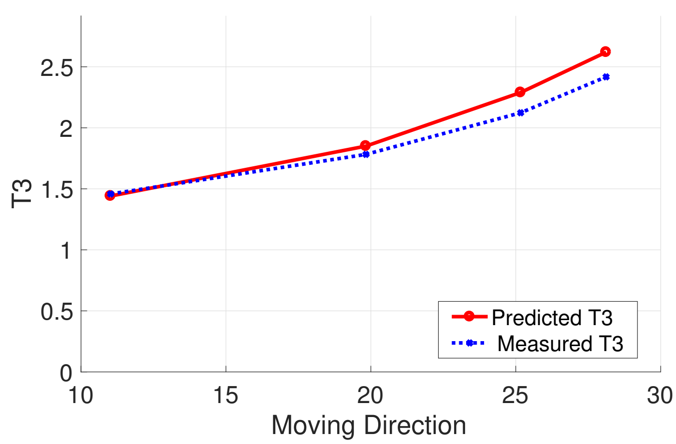

Figure 6.10: Predicted and Measured Lead Time of LOS Blockage T_3 as a Function of Moving Direction α

Based on Eq.6.3 and the measurement, it is further assumed that a person is moving at the speed of $S = 1.5m/s$. Since the starting time t_1 is irrelevant in the prediction, t_1 is arbitrary set as 0. The measured lead time is taken as $t_3 = \frac{A_i B_i}{S} + t_2$ while the predicted lead time is $\hat{t}_3 = \frac{\hat{A}_i B_i}{S} + t_2$. Figure 6.10 compares the predicted and the measured lead time to the LOS blockage as a function of α. It can be observed that the NLOS blockages are indeed detectable, and the LOS blockage prediction is accurate in general, especially for small α.

Remark 1 (Limitation)**.** *During the experiment, it is found the blockage position measurement becomes ill-defined with increased distance. For instance, A_4 is more of an area, instead of a point in Fig. 6.9, because human body has a certain width and cannot be exactly abstracted as a point. As a result, the blockage at A_4 becomes weak and noisy. Therefore, the prediction error increases with α. These unsolved problems can be mitigated if the experiment is done in a real time fashion where an obstacle is moving following one direction. The position can be found by finding the time corresponding to the lowest SNR.*

6.5 Conclusion

In this chapter, the equivalent blockage models have been introduced to convert the moving receiver and static obstacle scenario to the model with static receiver and moving obstacle. Based on this model, the moving direction estimation and blockage prediction strategy are demonstrated based on the geometry properties given the directional communication. The experiment result has shown that blockage time can be predicted with little error.

Chapter 7

Conclusions

This thesis covered two topics in the mmWave mobile communication —mobility management and blockage mitigation. At the beginning of the thesis, the necessity of introducing mmWave into mobile network is discussed. Then, to verify the source of problem, we provide detailed methodology of a 60GHz mmWave testbed. It contains three sub-modules and has two degree of freedom. The motion control module is constructed with high accuracy to study motion-caused inferior performance in mmWave communication. Meanwhile, the signal processing of the testbed is accomplished by the off-the-shelf SDR. The capability of channel measurement is verified by indoor experiments.

In order to maintain a robust mobile link, this thesis proposed two potential solutions—sensor-aided beam tracking and multi-connectivity. The first approach is based on the low-cost MEMS motion sensor within current mobile devices. The attitude information are gathered and then applied to correct the performance loss caused by misaligned beam direction. In this work, a quaternion-based motion aware beam tracking mechanism is integrated into protocol to reduce the system overhead. The performance is examined by the measurements captured by both mobile devices and optical system. The result demonstrates that the accuracy of tracking algorithm and efficiency of overhead reduction.

The multi-connectivity appears as the second option solution to fight with intermittent connection and provide robust performance. However, the complexity of backbone network and caching mechanism hinder the implementation with high frequency handover. To simplify the design, we modeled the mmWave link as an erasure channel and attack the problem with the fountain code. Afterward, a simplified backbone is defined correspondingly. Then, a field experiment captures a three link channel conditions over three hours. The static of the mmWave channel is incorporated in the simulation. Finally, the packet loss and associated throughput are analyzed.

The second topic is related to mitigating and utilizing the blockage in mmWave. In the study of mmWave drone, the mmWave testbed is integrated with a UAV propeller testbed. We exhibit the blockage loss, blockage patterns in terms of to the incidence angle and distances in the existence of working propeller. Based on these measurements, a multi-subcarrier model is proposed to study the blockage-aware communication protocol design. Then based on the Holm's procedure, the blockage edge detection is formed, aiming to control the FWER. The simulations show the effectiveness of detection algorithm and further validate that the throughput can be improved with a blockage-aware scheme.

Finally, contrary to the common sense that the blockage is only a detrimental factor, a geometrical analysis showed that under certain circumstance, the blockage on NLOS path could provide in-time active handover prediction to avoid the large latency in the passive case. We first derive the prediction algorithm and extend it to more cases in the outdoor environment. Then, in the experiment, we resolved the moving direction of blockage object and compared prediction timing with grand truths. This result supports our claim that the active handover can be done when you combine the geometry and blockage information.

Bibliography

[1] Abari, O., Hassanieh, H., Rodriguez, M., and Katabi, D. (2016). Millimeter wave communications: From point-to-point links to agile network connections. In *Proceedings of the 15th ACM Workshop on Hot Topics in Networks*, pages 169–175. ACM. 12

[2] Alkhateeb, A., El Ayach, O., Leus, G., and Heath, R. W. (2014). Channel estimation and hybrid precoding for millimeter wave cellular systems. *IEEE Journal of Selected Topics in Signal Processing*, 8(5):831–846. 7

[3] Alkhateeb, A., Nam, Y.-H., Rahman, M. S., Zhang, J., and Heath, R. W. (2017). Initial beam association in millimeter wave cellular systems: Analysis and design insights. *IEEE Transactions on Wireless Communications*, 16(5):2807–2821. 42

[4] Allen, K., DeMinco, N., Hoffman, J., Lo, Y., and Papazian, P. (1994). Building penetration loss measurements at 900 mhz, 11.4 ghz, and 28.8 ghz. *US Department of Commerce, National Telecommunications and Information Administration Rep*, pages 94–306. 7

[5] Anderson, C. R. and Rappaport, T. S. (2004). In-building wideband partition loss measurements at 2.5 and 60 ghz. *IEEE transactions on wireless communications*, 3(3):922–928. 11

[6] Andreev, V., Vdovin, V., and Voronov, P. (2003). An experimental study of millimeter wave absorption in thin metal films. *Technical Physics Letters*, 29(11):953–955. 7

[7] Astely, D., Dahlman, E., Fodor, G., Parkvall, S., and Sachs, J. (2013). Lte release 12 and beyond. *IEEE Communications Magazine*, 51(7):154–160. 42

[8] Bai, T., Alkhateeb, A., and Heath, R. W. (2014). Coverage and capacity of millimeter-wave cellular networks. *IEEE Communications Magazine*, 52(9):70–77. 6

[9] Barati, C. N., Hosseini, S. A., Mezzavilla, M., Korakis, T., Panwar, S. S., Rangan, S., and Zorzi, M. (2016). Initial access in millimeter wave cellular systems. *IEEE Transactions on Wireless Communications*, 15(12):7926–7940. 8, 88

[10] Brady, J., Behdad, N., and Sayeed, A. M. (2013). Beamspace mimo for millimeter-wave communications: System architecture, modeling, analysis, and measurements. *IEEE Transactions on Antennas and Propagation*, 61(7):3814–3827. 7

[11] Center, V. (2013). Unmanned aircraft system (uas) service demand 2015-2035: Literature review & projections of future usage. 61

[12] Chen, S., Qin, F., Hu, B., Li, X., and Chen, Z. (2016). User-centric ultra-dense networks for 5g: challenges, methodologies, and directions. *IEEE Wireless Communications*, 23(2):78–85. 2

[13] Collonge, S., Zaharia, G., and Zein, G. E. (2004a). Influence of the human activity on wide-band characteristics of the 60 ghz indoor radio channel. *IEEE Transactions on Wireless Communications*, 3(6):2396–2406. 33

[14] Collonge, S., Zaharia, G., and Zein, G. E. (2004b). Influence of the human activity on wide-band characteristics of the 60 ghz indoor radio channel. *IEEE Transactions on Wireless Communications*, 3(6):2396–2406. 43, 62, 88

[15] Commission, F. C. (accessed Jan 5, 2018). Fcc 16-89 report and order and further notice of proposed rulemaking. 1

[16] Consortium, W. et al. (2010). Wirelesshd specification version 1.1 overview. *Specification. California, USA*. 3

[17] Constantine, A. B. et al. (2005). Antenna theory: analysis and design. *MICROSTRIP ANTENNAS, third edition, John wiley & sons*. 6

[18] Costello, D. J. and Forney, G. D. (2007). Channel coding: The road to channel capacity. *Proceedings of the IEEE*, 95(6):1150–1177. 1

[19] CTIA (2015). Mobile data demand: growth forecasts met. Technical report, CTIA. 1

[20] Cudak, M., Kovarik, T., Thomas, T. A., Ghosh, A., Kishiyama, Y., and Nakamura, T. (2014). Experimental mm wave 5g cellular system. In *Globecom Workshops (GC Wkshps), 2014*, pages 377–381. IEEE. 9

[21] Dahlman, E., Parkvall, S., and Skold, J. (2016). *4G, LTE-advanced Pro and the Road to 5G*. Academic Press. 43

[22] Dai, L. and Gao, X. (2016). Priori-aided channel tracking for millimeter-wave beamspace massive mimo systems. In *URSI Asia-Pacific Radio Science Conference (URSI AP-RASC)*, pages 1493–1496. IEEE. 9

[23] Desai, V., Krzymien, L., Sartori, P., Xiao, W., Soong, A., and Alkhateeb, A. (2014). Initial beamforming for mmwave communications. In *Signals, Systems and Computers, 2014 48th Asilomar Conference on*, pages 1926–1930. IEEE. 8

[24] DJI (accessed Jan 5, 2018). E1200 pro tuned poopulsion system. 65

[25] ECMA (2010). Standard ecma-387 high rate 60 ghz phy, mac and hdmi pals. Technical report, ECMA. 3

[26] Emerson, D. T. (1997). The work of jagadis chandra bose: 100 years of mm-wave research. In *Microwave Symposium Digest, 1997., IEEE MTT-S International*, volume 2, pages 553–556. IEEE. 2

[27] Ford, R., Rangan, S., Mellios, E., and Nix, D. K. A. (2017). Markov channel-based performance analysis formillimeter wave mobile networks. In *Proceedings of the IEEE WCNC Conference*. 90

[28] Gao, K., Cai, M., Nie, D., Hochwald, B., Laneman, J. N., Huang, H., and Liu, K. (2016). Beampattern-based tracking for millimeter wave communication systems. In *Global Communications Conference (GLOBECOM), 2016 IEEE*, pages 1–6. IEEE. 9

[29] Gao, Z., Dai, L., Mi, D., Wang, Z., Imran, M. A., and Shakir, M. Z. (2015). Mmwave massive-mimo-based wireless backhaul for the 5g ultra-dense network. *IEEE Wireless Communications*, 22(5):13–21. 2

[30] Ghasempour, Y. and Knightly, E. W. (2017). Decoupling beam steering and user selection for scaling multi-user 60 ghz wlans. In *Proceedings of the 18th ACM International Symposium on Mobile Ad Hoc Networking and Computing*, page 10. ACM. 12

[31] Ghosh, A. (Accessed: 02/10/2018). 5g new radio mmwave : Present and future. 14

[32] Giordani, M., Mezzavilla, M., Rangan, S., and Zorzi, M. (2016). Multi-connectivity in 5g mmwave cellular networks. In *Ad Hoc Networking Workshop (Med-Hoc-Net), 2016 Mediterranean*, pages 1–7. IEEE. 42

[33] Goyal, S., Mezzavilla, M., Rangan, S., Panwar, S., and Zorzi, M. (2017). User association in 5g mmwave networks. In *2017 IEEE Wireless Communications and Networking Conference (WCNC)*, pages 1–6. 90

[34] Granjon, P. (2012). The cusum algorithm a small review. *Gipsa-Lab, Grenoble, France, Team SAIGA*. 79

[35] Gutierrez, F., Agarwal, S., Parrish, K., and Rappaport, T. S. (2009). On-chip integrated antenna structures in cmos for 60 ghz wpan systems. *IEEE Journal on Selected Areas in Communications*, 27(8). 6

[36] Haider, M. K. and Knightly, E. W. (2016). Mobility resilience and overhead constrained adaptation in directional 60 ghz wlans: Protocol design and system implementation. In *Proceedings of the 17th ACM International Symposium on Mobile Ad Hoc Networking and Computing*, MobiHoc '16, pages 61–70, New York, NY, USA. ACM. 12

[37] Haider, M. K. and Knightly, E. W. (2018). itrack: Tracking indicator leds on aps to bootstrap mmwave beam acquisition and steering. In *Proceedings of the 19th International Workshop on Mobile Computing Systems & Applications*, HotMobile '18, pages 107–112, New York, NY, USA. ACM. 8, 12

[38] Heath, R. W., Gonzalez-Prelcic, N., Rangan, S., Roh, W., and Sayeed, A. M. (2016). An overview of signal processing techniques for millimeter wave mimo systems. *IEEE journal of selected topics in signal processing*, 10(3):436–453. 1, 6, 7

[39] IEEE (2009). Ieee standard for information technology– local and metropolitan area networks– specific requirements– part 15.3: Amendment 2: Millimeter-wave-based alternative physical layer extension. *IEEE Std 802.15.3c-2009 (Amendment to IEEE Std 802.15.3-2003)*, pages 1–200. 3

[40] IEEE (2012). Ieee draft standard for local and metropolitan area networks - specific requirements - part 11: Wireless lan medium access control (mac) and physical layer (phy) specifications - amendment 3: Enhancements for very high throughput in the 60 ghz band. *IEEE P802.11ad/D8.0, May 2012 (Draft Amendment based on IEEE 802.11-2012)*, pages 1–667. 3

[41] Instruments, N. (Accessed: 01/10/2018). Introduction to the ni mmwave transceiver system hardware. 12

[42] Jeong, C., Park, J., and Yu, H. (2015). Random access in millimeter-wave beamforming cellular networks: issues and approaches. *IEEE Communications Magazine*, 53(1):180–185. 8

[43] Kaplan, E. L. and Meier, P. (1958). Nonparametric estimation from incomplete observations. *Journal of the American statistical association*, 53(282):457–481. 80

[44] Kutty, S. and Sen, D. (2016). Beamforming for millimeter wave communications: An inclusive survey. *IEEE Communications Surveys & Tutorials*, 18(2):949–973. 6

[45] Lee, G., Sung, Y., and Seo, J. (2016). Randomly-directional beamforming in millimeter-wave multiuser miso downlink. *IEEE Transactions on Wireless Communications*, 15(2):1086–1100. 8

[46] Lehmann, E. L. and Romano, J. P. (2008). *Testing Statistical Hypothesis*. Springer. 76, 80

[47] Lema, M. A., Pardo, E., Galinina, O., Andreev, S., and Dohler, M. (2016). Flexible dual-connectivity spectrum aggregation for decoupled uplink and downlink access in 5g heterogeneous systems. *IEEE Journal on Selected Areas in Communications*, 34(11):2851–2865. 42

[48] Li, X., Guo, D., Yin, H., and Wei, G. (2015). Drone-assisted public safety wireless broadband network. In *Wireless Communications and Networking Conference Workshops (WCNCW), 2015 IEEE*, pages 323–328. IEEE. 61

[49] Lorden, G. (1971). Procedures for reacting to a change in distribution. *The Annals of Mathematical Statistics*, pages 1897–1908. 78

[50] Lu, J. S., Steinbach, D., Cabrol, P., and Pietraski, P. (2012). Modeling human blockers in millimeter wave radio links. *ZTE Communications*, 10(4):23–28. 7

[51] Luby, M., Gasiba, T., Stockhammer, T., and Watson, M. (2007). Reliable multimedia download delivery in cellular broadcast networks. *IEEE Transactions on Broadcasting*, 53(1):235–246. 47

[52] Lynn, V., Sohigian, M., and Crocker, E. (1964). Radar observations of the moon at a wavelength of 8.6 millimeters. *Journal of Geophysical Research*, 69(4):781–783. 2

[53] MacCartney, G. R., Samimi, M. K., and Rappaport, T. S. (2014). Omnidirectional path loss models in new york city at 28 ghz and 73 ghz. In *Personal, Indoor, and Mobile Radio Communication (PIMRC), 2014 IEEE 25th Annual International Symposium on*, pages 227–231. IEEE. 11

[54] MacKay, D. J. (2005). Fountain codes. *IEE Proceedings-Communications*, 152(6):1062–1068. 47

[55] Madgwick, S. (2010). An efficient orientation filter for inertial and inertial/magnetic sensor arrays. *Report x-io and University of Bristol (UK)*, 25. 27, 38

[56] Mahony, R., Hamel, T., and Pflimlin, J.-M. (2005). Complementary filter design on the special orthogonal group so (3). In *Decision and Control, 2005 and 2005 European Control Conference. CDC-ECC'05. 44th IEEE Conference on*, pages 1477–1484. IEEE. 27, 38

[57] Mezzavilla, M., Goyal, S., Panwar, S., Rangan, S., and Zorzi, M. (2016). An mdp model for optimal handover decisions in mmwave cellular networks. In *2016 European Conference on Networks and Communications (EuCNC)*, pages 100–105. 90

[58] Mo, J. and Heath, R. W. (2014). High snr capacity of millimeter wave mimo systems with one-bit quantization. In *Information Theory and Applications Workshop (ITA), 2014*, pages 1–5. IEEE. 7

[59] NaturalPoint (2017). Optitrack. [Online; accessed 1-March-2017]. 33

[60] Nitsche, T., Bielsa, G., Tejado, I., Loch, A., and Widmer, J. (2015a). Boon and bane of 60 ghz networks: Practical insights into beamforming, interference, and frame level operation. In *Proceedings of the 11th ACM Conference on Emerging Networking Experiments and Technologies*, CoNEXT '15, pages 17:1–17:13, New York, NY, USA. ACM. 11

[61] Nitsche, T., Flores, A. B., Knightly, E. W., and Widmer, J. (2015b). Steering with eyes closed: mm-wave beam steering without in-band measurement. In *Computer Communications (INFOCOM), 2015 IEEE Conference on*, pages 2416–2424. IEEE. 8

[62] Nitsche, T., Flores, A. B., Knightly, E. W., and Widmer, J. (2015c). Steering with eyes closed: mm-wave beam steering without in-band measurement. In *Computer Communications (INFOCOM), 2015 IEEE Conference on*, pages 2416–2424. IEEE. 23, 25

[63] Oh, T., Song, C., Jung, J., and Lee, I. (2017). A new rf beam training method for multi-user millimeter wave systems. In *Communications (ICC), 2017 IEEE International Conference on*, pages 1–6. IEEE. 8

[64] Orhan, O., Erkip, E., and Rangan, S. (2015). Low power analog-to-digital conversion in millimeter wave systems: Impact of resolution and bandwidth on performance. In *Information Theory and Applications Workshop (ITA), 2015*, pages 191–198. IEEE. 7

[65] Pi, Z., Choi, J., and Heath, R. (2016). Millimeter-wave gigabit broadband evolution toward 5g: fixed access and backhaul. *IEEE Communications Magazine*, 54(4):138–144. 2

[66] Polese, M., Giordani, M., Mezzavilla, M., Rangan, S., and Zorzi, M. (2017a). Improved handover through dual connectivity in 5g mmwave mobile networks. *IEEE Journal on Selected Areas in Communications*, 35(9):2069–2084. 42

[67] Polese, M., Jana, R., and Zorzi, M. (2017b). Tcp in 5g mmwave networks: Link level retransmissions and mp-tcp. *arXiv preprint arXiv:1703.08985*. 8

[68] Qingling, Z. and Li, J. (2006). Rain attenuation in millimeter wave ranges. In *Antennas, Propagation & EM Theory, 2006. ISAPE'06. 7th International Symposium on*, pages 1–4. IEEE. 5

[69] Qualcomm (accessed Jan 5, 2018). Qualcomm presentation, 1000x: Mobile data challenge. 1

[70] Rangan, S., Rappaport, T. S., and Erkip, E. (2014). Millimeter-wave cellular wireless networks: Potentials and challenges. *Proceedings of the IEEE*, 102(3):366–385. 1

[71] Rappaport, T. S., Gutierrez, F., Ben-Dor, E., Murdock, J. N., Qiao, Y., and Tamir, J. I. (2013a). Broadband millimeter-wave propagation measurements and models using adaptive-beam antennas for outdoor urban cellular communications. *IEEE transactions on antennas and propagation*, 61(4):1850–1859. 7

[72] Rappaport, T. S., Heath Jr, R. W., Daniels, R. C., and Murdock, J. N. (2014). *Millimeter wave wireless communications*. Pearson Education. 62

[73] Rappaport, T. S., MacCartney, G. R., Samimi, M. K., and Sun, S. (2015). Wideband millimeter-wave propagation measurements and channel models for future wireless communication system design. *IEEE Transactions on Communications*, 63(9):3029–3056. 1, 7

[74] Rappaport, T. S., Murdock, J. N., and Gutierrez, F. (2011). State of the art in 60-ghz integrated circuits and systems for wireless communications. *Proceedings of the IEEE*, 99(8):1390–1436. 2

[75] Rappaport, T. S., Sun, S., Mayzus, R., Zhao, H., Azar, Y., Wang, K., Wong, G. N., Schulz, J. K., Samimi, M., and Gutierrez, F. (2013b). Millimeter wave mobile communications for 5g cellular: It will work! *IEEE access*, 1:335–349. 1

[76] Roh, W., Seol, J.-Y., Park, J., Lee, B., Lee, J., Kim, Y., Cho, J., Cheun, K., and Aryanfar, F. (2014). Millimeter-wave beamforming as an enabling technology for 5g cellular communications: Theoretical feasibility and prototype results. *IEEE communications magazine*, 52(2):106–113. 1, 6

[77] Rosa, C., Pedersen, K., Wang, H., Michaelsen, P.-H., Barbera, S., Malkamaki, E., Henttonen, T., and Sébire, B. (2016). Dual connectivity for lte small cell evolution: Functionality and performance aspects. *IEEE Communications Magazine*, 54(6):137–143. 42

[78] Saha, S. K., Ghasempour, Y., Haider, M. K., Siddiqui, T., De Melo, P., Somanchi, N., Zakrajsek, L., Singh, A., Torres, O., Uvaydov, D., et al. (2017). X60: A programmable testbed for wideband 60 ghz wlans with phased arrays. In *Proceedings of the 11th Workshop on Wireless Network Testbeds, Experimental evaluation & CHaracterization*, pages 75–82. ACM. 12

[79] Saha, S. K., Vira, V. V., Garg, A., and Koutsonikolas, D. (2016). Multi-gigabit indoor wlans: Looking beyond 2.4/5 ghz. In *Communications (ICC), 2016 IEEE International Conference on*, pages 1–6. IEEE. 11

[80] Samimi, M., Wang, K., Azar, Y., Wong, G. N., Mayzus, R., Zhao, H., Schulz, J. K., Sun, S., Gutierrez, F., and Rappaport, T. S. (2013). 28 ghz angle of arrival and angle of departure analysis for outdoor cellular communications using steerable beam antennas in new york city. In *Vehicular Technology Conference (VTC Spring), 2013 IEEE 77th*, pages 1–6. IEEE. 25

[81] Samuylov, A., Gapeyenko, M., Moltchanov, D., Gerasimenko, M., Singh, S., Himayat, N., Andreev, S., and Koucheryavy, Y. (2016). Characterizing spatial correlation of blockage statistics in urban mmwave systems. In *Globecom Workshops (GC Wkshps), 2016 IEEE*, pages 1–7. IEEE. 7

[82] Sato, M. and Mizuno, K. (2010). Millimeter-wave imaging sensor. In *Microwave and Millimeter Wave Technologies from Photonic Bandgap Devices to Antenna and Applications*. InTech. 11

[83] Sayeed, A., Hall, C., and Zhu, K. Y. (2017). A lens array multi-beam mimo testbed for real-time mmwave communication and sensing. In *Proceedings of the 1st ACM Workshop on Millimeter-Wave Networks and Sensing Systems 2017*, pages 35–40. ACM. 13

[84] Sayeed, A. M. (2002). Deconstructing multiantenna fading channels. *IEEE Transactions on Signal Processing*, 50(10):2563–2579. 7

[85] Schwering, F. K., Violette, E. J., and Espeland, R. H. (1988). Millimeter-wave propagation in vegetation: Experiments and theory. *IEEE Transactions on Geoscience and Remote Sensing*, 26(3):355–367. 7

[86] Sector, I. R. (2013). Recommendation itu-r p. 676–10, attenuation by atmospheric gases. *International Telecommunications Union*. xi, 5

[87] Seo, M., Ananthasubramaniam, B., Madhow, U., and Rodwell, M. J. (2007). Millimeterwave (60 ghz) imaging wireless sensor network: Recent progress. In *Signals, Systems and Computers, 2007. ACSSC 2007. Conference Record of the Forty-First Asilomar Conference on*, pages 396–400. IEEE. 11

[88] Shokrollahi, A., Luby, M., et al. (2011). Raptor codes. *Foundations and trends® in communications and information theory*, 6(3–4):213–322. 43, 47

[89] Singh, J., Dabeer, O., and Madhow, U. (2009). On the limits of communication with low-precision analog-to-digital conversion at the receiver. *IEEE Transactions on Communications*, 57(12). 7

[90] Smulders, P. F. (2009). Statistical characterization of 60-ghz indoor radio channels. *IEEE Transactions on Antennas and Propagation*, 57(10):2820–2829. 11

[91] Sur, S., Venkateswaran, V., Zhang, X., and Ramanathan, P. (2015). 60 ghz indoor networking through flexible beams: A link-level profiling. In *ACM SIGMETRICS Performance Evaluation Review*, volume 43, pages 71–84. ACM. 12

[92] Talukdar, A., Cudak, M., and Ghosh, A. (2014). Handoff rates for millimeterwave 5G systems. In *VTC Spring 2014*. 89

[93] Tartakovsky, A., Nikiforov, I., and Basseville, M. (2014). *Sequential Analysis: Hypothesis Testing and Change Point Detection*. CRC Press. 64, 80

[94] Tseng, P., Feng, K., and Huang, C. (2014). POMDP-based cell selection schemes for wireless networks. *IEEE Communications Letters*, 18(5):797–800. 90

[95] Tu, H., Lin, J., Chang, T., and Feng, K. (2012). Prediction-based handover schemes for relay-enhanced LTE-A systems. In *Proceedings of the IEEE WCNC Conference*. 90

[96] Watson, M. and Shokrallahi, T. S. M. L. A. (2011). Rfc 6330: Raptorq raptor forward error correction scheme for object delivery. Technical report, IETF, RFC 633. 47, 55

[97] Wei, T. and Zhang, X. (2015). mtrack: High-precision passive tracking using millimeter wave radios. In *Proceedings of the 21st Annual International Conference on Mobile Computing and Networking*, pages 117–129. ACM. 12

[98] Wiki (Accessed: 01/10/2018). List of software-defined radios. 12

[99] Wikipedia (2017). Wikipedia, the free encyclopedia. [Online; accessed 1-April-2017]. 28

[100] Xiao, M., Mumtaz, S., Huang, Y., Dai, L., Li, Y., Matthaiou, M., Karagiannidis, G. K., Björnson, E., Yang, K., Chih-Lin, I., et al. (2017). Millimeter wave communications for future mobile networks. *IEEE Journal on Selected Areas in Communications*, 35(9):1909–1935. 1

[101] Xu, H., Kukshya, V., and Rappaport, T. S. (2002). Spatial and temporal characteristics of 60-ghz indoor channels. *IEEE Journal on selected areas in communications*, 20(3):620–630. 2, 5, 11

[102] Xu, H., Rappaport, T. S., Boyle, R. J., and Schaffner, J. H. (2000). Measurements and models for 38-ghz point-to-multipoint radiowave propagation. *IEEE Journal on Selected Areas in Communications*, 18(3):310–321. 5

[103] Yanmaz, E., Kuschnig, R., and Bettstetter, C. (2011). Channel measurements over 802.11 a-based uav-to-ground links. In *GLOBECOM Workshops (GC Wkshps), 2011 IEEE*, pages 1280–1284. IEEE. 62

[104] Yorkgitis, C. (accessed Jan 5, 2018). Fcc adopts a second wave of millimeter wave regulations to support next generation terrestrial systems and services. 3

[105] Yoshioka, S., Inoue, Y., Suyama, S., Kishiyama, Y., Okumura, Y., Kepler, J., and Cudak, M. (2016). Field experimental evaluation of beamtracking and latency performance for 5g mmwave radio access in outdoor mobile environment. In *Personal, Indoor, and Mobile Radio Communications (PIMRC), 2016 IEEE 27th Annual International Symposium on*, pages 1–6. IEEE. 62, 81

[106] Zhang, H., Dong, Y., Cheng, J., Hossain, M. J., and Leung, V. C. (2016a). Fronthauling for 5g lte-u ultra dense cloud small cell networks. *IEEE Wireless Communications*, 23(6):48–53. 2

[107] Zhang, M., Mezzavilla, M., Ford, R., Rangan, S., Panwar, S., Mellios, E., Kong, D., Nix, A., and Zorzi, M. (2016b). Transport layer performance in 5g mmwave cellular. In *Computer Communications Workshops (INFOCOM WKSHPS), 2016 IEEE Conference on*, pages 730–735. IEEE. 8

[108] Zhao, H., Mayzus, R., Sun, S., Samimi, M., Schulz, J. K., Azar, Y., Wang, K., Wong, G. N., Gutierrez, F., and Rappaport, T. S. (2013). 28 ghz millimeter wave cellular communication measurements for reflection and penetration loss in and around buildings in new york city. In *Communications (ICC), 2013 IEEE International Conference on*, pages 5163–5167. IEEE. 7

[109] Zheng, G., Hua, C., Zheng, R., and Wang, Q. (2016). Toward robust relay placement in 60 ghz mmwave wireless personal area networks with directional antenna. *IEEE Transactions on Mobile Computing*, 15(3):762–773. 6

[110] Zhu, Y., Zhang, Z., Marzi, Z., Nelson, C., Madhow, U., Zhao, B. Y., and Zheng, H. (2014). Demystifying 60ghz outdoor picocells. In *Proceedings of the 20th annual international conference on Mobile computing and networking*, pages 5–16. ACM. 8

[111] Zhu, Y., Zhu, Y., Zhao, B. Y., and Zheng, H. (2015). Reusing 60ghz radios for mobile radar imaging. In *Proceedings of the 21st Annual International Conference on Mobile Computing and Networking*, MobiCom '15, pages 103–116, New York, NY, USA. ACM. 11

Vita

Jingchao Bao was born in Qingdao, China — a beautiful city by the Sea. He is the only child to the parent of LiLi and Xinyu Bao. After high school, he went to north and attended Harbin Institute of Technology in Harbin, Heilongjiang. In 2011, he received the B.S. degrees in electronic engineering. He received the research assistantship from University of Tennessee and started to pursue the Ph.D. degree in electrical engineering from 2012.